

Design and Control of UAV Systems: A Tri-Rotor UAV Case Study

A thesis submitted to the University of Manchester
for the degree of Doctor of Philosophy
in the Faculty of Engineering and Physical Sciences

2012

Mohamed Kara Mohamed

School of Electrical and Electronic Engineering

Contents

Abstract	6
Declaration	7
Copyright Statement	8
Dedication	10
Acknowledgment	11
1 Introduction	12
1.1 Background and Motivation	12
1.2 Thesis Structure and Outlines	14
1.3 Publications	16
2 Two Stage Feedback Linearisation To Handle Actuator Dynamics in Control Systems for UAVs	17

2.1	Introduction	18
2.2	Review of Input Output Feedback Linearization	19
2.3	Analyzing The Effect of Unmodeled Actuator Dynamics on Feedback Linearization	23
2.4	New Two Stage Feedback Linearisation to Handle Actuator Dynamics	32
2.5	Summary	42
3	An Explicit Design Procedure for Propulsion Systems of Electrically Driven VTOL UAVs	43
3.1	Introduction	44
3.1.1	Why A Design Procedure Is Needed?	44
3.2	Electric Propulsion Systems	46
3.2.1	Propellers	47
3.2.2	Propeller Model Verification	52
3.2.3	Electric Motors	55
3.2.4	Electric Speed Controllers (ESCs)	59
3.2.5	Battery Packs	59
3.3	Design Methodology	60
3.4	Summary	65

4	A New Cost Effective Indoor Navigation Technique for UAV Systems	66
4.1	Introduction and Related Work	67
4.2	System Description	69
4.3	Theoretical Formulation	72
4.3.1	UAV Position	72
4.3.2	UAV Orientation	74
4.4	Implementation	78
4.4.1	Obtaining the lengths of the Laser Beams	79
4.4.2	Capturing The Laser Dots Coordinates	80
4.4.3	On-board camera: restrictions to the angle α between the laser beams	81
4.4.4	The Implementation Algorithm	84
4.5	Summary	85
5	Case Study: Design and Control of Novel Tri-Rotor UAV	87
5.1	Background and Motivation	88
5.2	System Structure and Design	90
5.3	Mathematical Modeling	92
5.3.1	Reference Coordinate Systems and Notations	92
5.3.2	UAV Model	95

5.4	Control System Design	107
5.4.1	Control Synthesis Without Actuator Dynamics	108
5.4.2	Analysis of Unmodeled Actuator Dynamics Effect	119
5.4.3	Control System Design Including Actuators Dynamics: Comparison Study	124
5.5	Propulsion System Design	140
5.6	Hardware Assembly	150
5.7	Summary	152
6	Concluding Remarks	153
6.1	Contributions	153
6.2	Directions for Future Research	155
	References	157

Word Count = 48,790

Abstract

The University of Manchester

Mohamed Kara Mohamed

Doctor of Philosophy

Design and Control of UAV Systems: A Tri-Rotor UAV Case Study

22 October 2012

The field of UAV systems is an active research area with potential for development and enhancement in various perspectives. This thesis investigates different issues related to the design, operation and control of UAV systems with a focus on the application side of each proposed solution where the implementation side and applicability of the proposed solutions are always considered with high priority. The thesis discusses unmodeled actuator dynamics and their effect on UAV systems when using feedback linearisation to linearize nonlinear models of UAVs. The analysis shows potential risk when implementing feedback linearisation and neglecting actuator dynamics even for first order actuator system. A solution algorithm of two stage feedback linearisation is proposed to handle actuator dynamics and linearize the main dynamics of the system. In the field of design and operation of UAVs, this thesis proposes a systematic design procedure for electric propulsion systems that are widely used in UAVs. The design procedure guides the designer step by step to achieve minimum propulsion system weight or maximum flight time or a trade off between the two factors from the supplied solution sets. On the navigation side, the thesis proposes a new indoor navigation system that is easy to implement and less costly compared with other indoor navigation systems. The proposed system can be classified under computer-vision based navigation systems, however, it needs less information and less computational capacity. The thesis also contributes to the structure design of UAV systems by producing a novel tri-rotor UAV platform. The proposed UAV is novel in structure and design and has a centralized control system that stabilizes and tracks both rotational and transitional motion of the vehicle simultaneously.

Declaration

No portion of the work referred to in this thesis has been submitted in support of an application for another degree or qualification of this or any other university or other institution of learning.

Copyright Statement

- i. The author of this thesis (including any appendices and/or schedules to this thesis) owns certain copyright or related rights in it (the “Copyright”) and s/he has given The University of Manchester certain rights to use such Copyright, including for administrative purposes.
- ii. Copies of this thesis, either in full or in extracts and whether in hard or electronic copy, may be made only in accordance with the Copyright, Designs and Patents Act 1988 (as amended) and regulations issued under it or, where appropriate, in accordance with licensing agreements which the University has from time to time. This page must form part of any such copies made.
- iii. The ownership of certain Copyright, patents, designs, trade marks and other intellectual property (the “Intellectual Property”) and any reproductions of copyright works in the thesis, for example graphs and tables (“Reproductions”), which may be described in this thesis, may not be owned by the author and may be owned by third parties. Such Intellectual Property and Reproductions cannot and must not be made available for use without the prior written permission of the owner(s) of the relevant Intellectual Property and/or Reproductions.
- iv. Further information on the conditions under which disclosure, publication and commercialisation of this thesis, the Copyright and any Intellectual Property and/or Reproductions described in it may take place is available in the University IP Policy¹, in any relevant Thesis restriction declarations deposited in the University Library,

¹see <http://www.campus.manchester.ac.uk/medialibrary/policies/intellectual-property.pdf>

The University Library's regulations² and in The University's policy on presentation of Theses.

²see <http://www.manchester.ac.uk/library/aboutus/regulations>

Dedication

To my parents and wife

for their love, support and praying.

Acknowledgment

All praise and thanks are due to Almighty Allah for his continuous blessing and for giving me the strength and ability to complete my PhD journey and write up this thesis.

I would like to thank my supervisor Dr. Alexander Lanzon for his support and readiness to help during the course of my research study. His suggestions and comments were always vital to polish and improve my research skills.

I must also thank my parents, Majed Kara Mohamed and Lutfia Kawusra who spent their lives educating and nurturing me until I have achieved my degrees and reached this level of the learning journey. Thanks my father and mother. I am grateful to have parents like you who cover me always with their love and support without a return.

I am also indebted to my wife Dima Kurbah who joined me along the years of my PhD program. I thank her for taking care of our children and doing virtually all family chores on my behalf to give me spare times to stay at the university for long hours to read and research.

Special thanks also to all members of the Control Systems Centre for sharing ideas and creating such a learning joyful environment. I mention specially Dr. Sourav Patra and my colleagues Mobolaji Osinuga, Sönke Engleken, Martin Maya-Gonzalez and Dr. Zhuoyue Song.

Chapter 1

Introduction

1.1 Background and Motivation

The field of robotic applications is no longer restricted to the area of conventional robot systems represented by programmed mechanical arms or complete human-like systems designed to do routine tasks and take limited decisions [1]. The robotic systems include now advanced designs of different vehicles with high capabilities to take hard decisions and operate in harsh circumstances [2]. In this regard, Unmanned Aerial Vehicles (UAVs) are considered highly advanced robotic systems and have seen unprecedented level of development and growth.

UAVs were initially known as drones and introduced during World War I for pure military tasks, and since then they have been developing for wide range of applications [3]. On the top of their use in military activities, such as logistical operations for collecting data and observing enemies ([4, 5] and the references therein), UAV systems have been employed in civil missions of high risk or in areas where it is difficult for humans to execute tasks [6, 7, 8]. In the field of scientific research, UAVs are also used in several missions for investigating areas, collecting data, watching volcanoes, forecasting weather, monitoring isolated territories and other various activities [9, 10, 11]. The wide spectrum of applications for UAV systems has raised research interest in UAVs and makes the field of UAV

design and operation the most dynamic developing sector in aerospace industry [12, 3].

UAVs exist in various configurations and operate in different styles such as fixed-wing aircraft, rotary-wing or vertical take-off and landing (VTOL) with the latter being the rapidly evolving segment of all UAV markets [13]. In addition, VTOL systems are the major contributor in non-military applications [7]. Regardless of the type and application, the tendency shifts to smaller, more flexible, less costly and lighter weight UAV systems [14, 15, 16, 17] which leads to the emerge of miniature aerial vehicles (MAVs) and even micro UAVs in some projects that are referred to as μ UAVs [18]. Furthermore, latest UAV projects deploy multi-UAV systems to achieve more complex missions and cover wide operational areas [19, 20]. The multiple UAV operations benefit from the development of new technology in navigations systems, communication systems and control.

Designing and operating a UAV system is controlled by several factors such as the flight mechanics, mission type, vehicle instrumentations, on-board computing capability and the physical limitations of the vehicle [3, 21]. From research point of view, all these factors and other aspects of UAV systems are investigated and studied with an ultimate goal of improving the capability and stability of the vehicle, minimizing the power requirements and achieving full autonomy [9, 22]. With increasing number of research publications to meet these challenges and overcome the faced difficulties, open problems are still facing the design, control, application, navigation and sensors of UAV systems, see for example [3, 9, 23] and the references therein. Moreover, the rising of miniature air vehicles (MAVs) opens the door for more study related specifically to the design and development of these systems due to the limitation of size, weight and power of these miniature vehicles [18].

This thesis approaches UAV systems from different perspectives. It includes research studies for different issues related to the design and control of UAV systems. From control point of view, the study investigates actuator dynamics and their effect in control system performance when implementing feedback linearisation. A two stage feedback linearisation algorithm is proposed to compensate actuator dynamics and maintain the validity of feedback linearisation of UAV nonlinear systems. Moving to the design and navigation aspect of UAVs, the thesis introduces a general framework for designing electric propulsion system for VTOL UAVs and also tackles the indoor navigation problem

by introducing a novel cost-effective and easy to implement navigation strategy that benefits from computer vision algorithms. Furthermore, the thesis examines a novel design of tri-rotor UAV (in the sequel, referred to as the Tri-rotor UAV). The proposed UAV is used as a case study to demonstrate the effectiveness of the two stage feedback linearisation where a centralized \mathcal{H}_∞ controller associated with two stage feedback linearisation is synthesized for the proposed Tri-rotor system. In addition, the propulsion system of the vehicle is designed using the proposed propulsion system design procedure. The Tri-rotor vehicle is constructed and prepared for the next stage of experimental studies and analysis.

The thesis can be seen as a general guideline that can be used in UAV projects involves designing and operating a UAV system from scratch. The various subjects conducted in the thesis are related to different aspects of UAV systems but they form in total a harmony of general issues one might encounter to design, operate and control a UAV system.

1.2 Thesis Structure and Outlines

The thesis is arranged into six chapters. Outlines of the main chapters of the thesis are as follows:

- **Chapter 2: Two Stage Feedback Linearisation To Handle Actuator Dynamics in Control Systems for UAVs**

This chapter reviews the common feedback linearisation technique used widely in UAVs control design to linearize nonlinear model of UAV systems and then discusses the effect of unmodeled actuator dynamics on the linearized system and overall stability of the UAV. The study shows that it is vital to include actuator dynamics when implementing feedback linearisation. Assuming that actuator dynamics are available, a two stage feedback linearisation algorithm is proposed to compensate for actuator dynamics in the first stage and then linearize the UAV model in the second stage. The proposed two stage algorithm is simpler compared to the process of linearizing the total UAV system including actuator dynamics.

- **Chapter 3: An Explicit Design Procedure for Propulsion Systems of Electrically Driven VTOL UAVs**

In this chapter, the design of propulsion systems for electrically driven VTOL UAVs is discussed. The design objectives are to generate sufficient thrust and obtain maximum flight time by using the lightest possible components. Based on these factors, a design procedure is proposed to design efficiently electric propulsion systems from commercially available products. To implement the proposed procedure, a momentum theory based model is derived to quantify the thrust of propellers.

- **Chapter 4: A New Cost Effective Indoor Navigation Technique for UAV Systems**

This chapter introduces a new cost-effective navigation system that can be used for indoor applications. The proposed system benefits partially from computer-vision navigation algorithms, but in the same time it is simple as there is no need for scene construction or full image matching algorithms which puts this algorithm ahead over other existing vision-based navigation systems. This fact is very important in mini UAVs where the size and power of on-board processors are limited. Moreover, the proposed system gives information about the position and orientation of the vehicle directly without the need for another integration, estimation or optimization stage which makes the system free from error accumulation.

- **Chapter 5: Case Study: Design and Control of Novel Tri-Rotor UAV**

This chapter investigates the control and design of a novel tri-rotor UAV. The proposed platform has six degree of freedom resulting from full authority of torque and force vectoring that is achieved by using tilt-rotor mechanism. The chapter includes a full study of the proposed system including design, modeling and control. Moreover, the proposed tri-rotor platform is used as a case study for the propulsion system design procedure and the two stage feedback linearisation algorithm derived in early chapters of this thesis. For instance, the procedure introduced in Chapter 3 is used here to effectively design the propulsion system of the vehicle. In regard to the control system design of the vehicle, the study shows the effect of unmodeled actuator dynamics on control system performance and then a comparison analysis between the two stage feedback linearisation and the classical feedback linearisation is conducted. Upon linearizing the UAV system, \mathcal{H}_∞ loop shaping design

procedure is motivated to design a linear controller for the system where a centralized \mathcal{H}_∞ controller is synthesized to stabilize and track the translational motion and rotational motion of the vehicle simultaneously. The goal was to completely build and operate the proposed Tri-rotor UAV using the synthesized controller. Unfortunately, we ran out of time and this goal was not completely achieved within the time span of my PhD. The vehicle was built completely with installation of all equipment and components, yet, it is not ready for flight tests due to a technical communication problem between instruments. The results presented in this chapter are simulated using Matlab Simulink.

- **Chapter 6: Conclusion**

The conclusion and recommendations for future research are presented in this chapter.

1.3 Publications

Three conference papers were published based on the contents of this thesis as listed below. Parts of chapters 3 and 4 were presented in published conference papers 1 and 2 respectively. The conference paper 3 is based on Chapters 2 and 5.

1. Kara Mohamed, M., Patra, S. and Lanzon, A., “Designing simple indoor navigation system for UAVs”, Proceedings of The 19th Mediterranean Conference on Control and Automation , Corfu, Greece, pp. 1223–1228, June 2011.
2. Kara Mohamed, M., Patra, S. and Lanzon, A., “Designing electric propulsion systems for UAVs”, Lecture Notes in Artificial Intelligence, Subseries of Lecture Notes in Computer Science, Vol. 6856, Springer, Proceedings of The 12th Annual Conference Towards Autonomous Robotic Systems, Sheffield, UK, pp. 388–389, September 2011.
3. Mohamed Kara, M. and Lanzon, A. "Design and Control of Novel Tri-rotor UAV", Proceedings of The UKACC International Conference on Control 2012, Cardiff, UK, pp. 304 - 309, September 2012.

Chapter 2

Two Stage Feedback Linearisation To Handle Actuator Dynamics in Control Systems for UAVs

This chapter is dedicated to the control design of UAV systems represented by nonlinear models. The chapter discusses feedback linearisation (FL) technique used to transform the UAV nonlinear system into a linear one and the effect of unmodeled actuator dynamics on the stability of the linearized system. A two stage feedback linearisation procedure to compensate actuator dynamics and linearize the UAV system is proposed.

The chapter is organized as follows. In Section 2.2, the input-output feedback linearisation technique is reviewed. The effect of unmodeled actuator dynamics on input-output feedback linearisation is discussed in Section 2.3. In Section 2.4, we propose a two stage input-output feedback linearisation algorithm for fully modeled system including actuator dynamics. A summary of the chapter is presented in Section 2.5.

2.1 Introduction

One of the common techniques used to handle nonlinear systems is to linearize the system by canceling the nonlinearity and then a linear system control method can be used to synthesize a controller for the linearized system [24]. Canceling the nonlinearity of nonlinear systems via feedback is known as feedback linearisation and it can be either state-input feedback linearisation or input-output feedback linearisation. Generally speaking, UAVs are nonlinear systems and input-output feedback linearisation is widely applied in UAV systems [25, 26, 27, 28] where it can be viewed as a method to transform the UAV nonlinear system into a linear system with respect to a new defined control input.

To simplify the implementation of feedback linearisation, several assumptions related to the model of the system and its operating point are considered. Among these assumptions is the negligence of actuator dynamics. In UAV literature, actuator dynamics are commonly neglected when modeling the system and synthesizing a controller, see for example [29, 30, 31] and the references therein. In these references, it is assumed that actuators are fast and their dynamics can be neglected safely. In this chapter, we show that this assumption is not valid always and when it comes to feedback linearisation, unmodeled actuator dynamics have vital effect and they can destabilize the system.

The problem of actuators dynamics and their effect on feedback linearisation has been addressed by several researches, see for example [32, 33] and there references therein. However, the focus in these references is on how to recover the stability of the system when actuators dynamics are not modeled. In this chapter, we assume that actuator dynamics are available and then a two stage feedback linearisation method to handle actuator dynamics and linearize the UAV nonlinear system is developed. The work presented in this chapter is more generic compared to [34], where the compensation of actuator dynamics is considered only for a specific SISO system.

2.2 Review of Input Output Feedback Linearization

This section outlines the input-output feedback linearisation method used to transfer a nonlinear system into a linear one and thereafter a linear control method can be used to synthesize a controller for the linearized system.

Consider a class of continuous multi-input multi-output (MIMO) nonlinear fully actuated UAV systems of the form:

$$\dot{x} = f(x) + \sum_{j=1}^m g_j(x)u_j \quad (2.1)$$

$$y = h(x) \quad (2.2)$$

where $x \in \mathbb{R}^n$ is the state vector of the system, $u_j \in \mathbb{R}$ is the j^{th} control input. $y \in \mathbb{R}^m$ is the measured output vector of the system.

Assuming that $f(\cdot)$, $h(\cdot)$ and $g_j(\cdot)$ are sufficiently smooth in a domain $\mathbb{D}_j \subset \mathbb{R}$, the derivative k of an output $y_i \in y$ is given by:

$$y_i^{(k)} = L_f^k h_i + \sum_{j=1}^m L_{g_j} L_f^{k-1} h_i u_j, \quad 1 \leq i \leq m, \quad (2.3)$$

where $L_f h_i$ is the Lie derivative of the scalar function h_i with respect to the vector function f and is defined as [35]:

$$L_f h_i(x) = \frac{\partial h_i(x)}{\partial x} f(x) \quad (2.4)$$

and for higher derivatives, we have:

$$\begin{aligned} L_f^2 h_i(x) &= \frac{\partial (L_f h_i(x))}{\partial x} f(x) \\ &\vdots \\ L_f^k h_i(x) &= \frac{\partial (L_f^{k-1} h_i(x))}{\partial x} f(x) \end{aligned}$$

and similarly, we have:

$$\begin{aligned}
L_{g_j}L_f h_i(x) &= \frac{\partial (L_f h_i(x))}{\partial x} g_j(x) = \frac{\partial}{\partial x} \left(\frac{\partial h_i(x)}{\partial x} f(x) \right) g_j(x) \\
&\vdots \\
L_{g_j}L_f^k h_i(x) &= \frac{\partial}{\partial x} \left(L_f^{k-1} h_i(x) f(x) \right) g_j(x)
\end{aligned}$$

In order to understand how the input u enters the linearized system, the notion "*relative degree*" is introduced. From Eq. (2.3), the output y_i is said to have a relative degree r_i if:

$$L_{g_j} h_i = L_{g_j} L_f h_i = L_{g_j} L_f^2 h_i = \dots = L_{g_j} L_f^{r_i-2} h_i = 0 \quad \forall 1 \leq i, j \leq m \quad (2.5)$$

where $L_{g_j} h_i$ is the Lie derivative of the scalar function h_i with respect to the vector function g_j and it is defined in similar way to the definition in Eq. (2.4) as:

$$L_{g_j} h_i(x) = \frac{\partial h_i(x)}{\partial x} g_j(x)$$

and for higher derivatives, we have:

$$L_{g_j}^k h_i(x) = \frac{\partial \left(L_{g_j}^{k-1} h_i(x) \right)}{\partial x} g_j(x)$$

In this context, the relative degree can be seen as the number of times the output needs to be differentiated before the input appears explicitly. In LTI systems, the relative degree is defined as the difference between the number of poles and the number of zeros of the system. In our case, the total relative degree of the MIMO system (2.1) - (2.2) in \mathbb{D} is defined as the sum of the relative degree of all outputs:

$$r = r_1 + r_2 + \dots + r_m \quad (2.6)$$

where \mathbb{D} is the intersection of all $\mathbb{D}_j, j = 1, 2, \dots, m$. When $r = n$, the input-output linearisation is equivalent to the input-state linearisation with no internal dynamics. The term "internal dynamics" is used to reflect the existence of states that are not observable from the output of the system when using input-output feedback linearisation. Internal dynam-

ics are dynamics related to these unobservable states. These unobservable states might be unbounded and destabilize the system. When the relative degree of the system equals to the number of states, all states will be observable and there is no internal dynamics. For now, let's assume that $r = n$ with no internal dynamics.

Define a new mapping $\zeta = T(x)$ as:

$$\zeta = \begin{bmatrix} \zeta_1 \\ \zeta_2 \\ \vdots \\ \zeta_m \end{bmatrix}, \quad (2.7)$$

where

$$\zeta_i = \begin{bmatrix} h_i(x) \\ L_f h_i(x) \\ \vdots \\ L_f^{r_i-1} h_i(x) \end{bmatrix}, \quad 1 \leq i \leq m. \quad (2.8)$$

We define also a new input vector ϑ as:

$$\vartheta = \begin{bmatrix} y_1^{(r_1)} \\ y_2^{(r_2)} \\ \vdots \\ y_m^{(r_m)} \end{bmatrix} \quad (2.9)$$

Then, the nonlinear system (2.1) - (2.2) can be transformed into a linearized system of a global normal form defined by:

$$\dot{\zeta} = \mathbf{A}_c \zeta + \mathbf{B}_c \vartheta \quad (2.10)$$

$$y = \mathbf{C}_c \zeta \quad (2.11)$$

where

$$\mathbf{A}_c = \begin{bmatrix} \mathbf{A}_1 & & & & \\ & \mathbf{A}_2 & & & \\ & & \dots & & \\ & & & & \mathbf{A}_m \end{bmatrix}, \quad \mathbf{B}_c = \begin{bmatrix} B_1 & & & & \\ & B_2 & & & \\ & & \dots & & \\ & & & & B_m \end{bmatrix}, \quad \mathbf{C}_c = \begin{bmatrix} C_1 & & & & \\ & C_2 & & & \\ & & \dots & & \\ & & & & C_m \end{bmatrix}$$

A_j, B_j, C_j with $1 \leq j \leq m$ are the matrices of the Brunovsky canonical form and given by [36]:

$$\mathbf{A}_j = \begin{bmatrix} 0 & 1 & 0 & 0 & \dots & 0 \\ 0 & 0 & 1 & 0 & \dots & 0 \\ \vdots & \vdots & \vdots & \vdots & \vdots & \vdots \\ 0 & 0 & 0 & \dots & 0 & 1 \\ 0 & 0 & 0 & 0 & \dots & 0 \end{bmatrix} \in \mathbb{R}^{r_j \times r_j}, \quad \mathbf{B}_j = \begin{bmatrix} 0 \\ \vdots \\ 0 \\ 1 \end{bmatrix} \in \mathbb{R}^{r_j \times 1}, \quad \mathbf{C}_j = \begin{bmatrix} 1 & 0 & \dots & 0 \end{bmatrix} \in \mathbb{R}^{1 \times r_j} \quad (2.12)$$

The feedback linearisation law from system (2.1) - (2.2) to the linearized system (2.10) - (2.11) is given by:

$$u(x, \vartheta) = \alpha(x) + \boldsymbol{\beta}^{-1}(x)\vartheta \quad (2.13)$$

where

$$\boldsymbol{\beta}(x) = \begin{bmatrix} L_{g_1} L_f^{r_1-1} h_1(x) & \dots & L_{g_m} L_f^{r_1-1} h_1(x) \\ \vdots & \vdots & \vdots \\ L_{g_1} L_f^{r_m-1} h_m(x) & \dots & L_{g_m} L_f^{r_m-1} h_m(x) \end{bmatrix}, \quad (2.14)$$

$$\alpha(x) = -\boldsymbol{\beta}(x)^{-1} \begin{bmatrix} L_f^{r_1} h_1(x) \\ \vdots \\ L_f^{r_m} h_m(x) \end{bmatrix}, \quad (2.15)$$

and

$$u = \begin{bmatrix} u_1 \\ u_2 \\ \vdots \\ u_m \end{bmatrix} \quad (2.16)$$

The matrix $\boldsymbol{\beta}(x)$ in Eq. (2.14) is called the decoupling matrix. We assume that $\boldsymbol{\beta}$ is invertible on the domain \mathbb{D} and then we define the feedback linearisation on this domain.

The linear system represented by Equations (2.10) - (2.11) can be controlled using a linear system control method whereas the field of linear systems is rich of several control methods that can be used to stabilize the system and track the reference signals, e.g., LQR, LQG, state feedback and \mathcal{H}_∞ loop-shaping design [37, 38]. In this thesis, we invoke the \mathcal{H}_∞ loop-shaping design as a robust control method for the linearized system when considering the case study of the Tri-rotor UAV. The motivation behind the \mathcal{H}_∞ loop-shaping design along with a brief introduction of the procedure is presented Chapter 5.

2.3 Analyzing The Effect of Unmodeled Actuator Dynamics on Feedback Linearization

The input-output feedback linearisation technique presented in the previous section linearizes the UAV nonlinear system by canceling the nonlinearities via feedback linearisation. In UAV systems, when applying feedback linearisation, actuator dynamics are usually neglected assuming that actuators are fast enough to apply the required controller action without a considerable delay, see for example [29, 30, 31] and the references therein. In practice, the input u to the UAV system (2.1) - (2.2) is applied by mechanical or electrical actuators of physical constraints which makes the assumption of ignoring their dynamics questionable. In this section, we analyze the effect of unmodeled actuator dynamics on input-output feedback linearisation.

We assume that actuator dynamics can be approximated by a MIMO LTI system as:

$$\dot{x}_a = \mathbf{A}_a x_a + \mathbf{B}_a u_a \quad (2.17)$$

$$y_a = \mathbf{C}_a x_a \quad (2.18)$$

where $x_a \in \mathbb{R}^{n_a}$ is the state vector of the actuators system and $u_a \in \mathbb{R}^m$ is the control input of the actuators. We assume also that the actuators system is asymptotically stable for all

values $x_a \in \mathbb{D}$, where \mathbb{D} is the domain of existence of the feedback linearisation law.

We recall the linearized system of the nonlinear model (2.1) - (2.2) which is given by:

$$\dot{\zeta} = \mathbf{A}_c \zeta + \mathbf{B}_c \vartheta \quad (2.19)$$

$$y = \mathbf{C}_c \zeta \quad (2.20)$$

and the feedback linearisation law from (2.13) is:

$$u(x, \vartheta) = \alpha(x) + \boldsymbol{\beta}^{-1}(x) \vartheta \quad (2.21)$$

Suppose that the mapping $\zeta = T(x)$ is invertible and we can get:

$$x = T^{-1}(\zeta) \quad (2.22)$$

Using Eq. (2.21) and the mapping (2.22), the artificial control input ϑ in terms of the physical input u can be given by:

$$\vartheta(\zeta, u) = \boldsymbol{\beta}(\zeta)(u - \alpha(\zeta)) \quad (2.23)$$

The linearized system can be written in terms of the physical input as:

$$\dot{\zeta} = \mathbf{A}_c \zeta + \mathbf{B}_c \boldsymbol{\beta}(\zeta)(u - \alpha(\zeta)) \quad (2.24)$$

$$y = \mathbf{C}_c \zeta \quad (2.25)$$

When imposing actuators dynamics, the perturbed plant by actuator dynamics can be

represented by:

$$\dot{\zeta} = \mathbf{A}_c \zeta + \mathbf{B}_c \boldsymbol{\beta}(\zeta)(y_a - \alpha(\zeta)) \quad (2.26)$$

$$\dot{x}_a = \mathbf{A}_a x_a + \mathbf{B}_a u \quad (2.27)$$

$$y_a = \mathbf{C}_a x_a \quad (2.28)$$

$$y = \mathbf{C}_c \zeta \quad (2.29)$$

Using (2.21) the mapping (2.22), we write the system from ϑ to y as:

$$\dot{\zeta} = \mathbf{A}_c \zeta + \mathbf{B}_c \boldsymbol{\beta}(\zeta) \mathbf{C}_a x_a - \mathbf{B}_c \boldsymbol{\beta}(\zeta) \alpha(\zeta) \quad (2.30)$$

$$\dot{x}_a = \mathbf{A}_a x_a + \mathbf{B}_a \alpha(\zeta) + \mathbf{B}_a \boldsymbol{\beta}^{-1}(\zeta) \vartheta \quad (2.31)$$

$$y = \mathbf{C}_c \zeta \quad (2.32)$$

The perturbed system (2.30) - (2.31) by actuator dynamics is nonlinear system and different from the linearized system (2.10) - (2.11). The order of the perturbed system from ϑ to y is $n + n_a$ where n is the order of the UAV system without actuators and n_a is the order of the actuators system. There is no guarantee that the synthesized controller for the linearized plant (2.10) - (2.11) will be able to control the nonlinear system (2.30) - (2.31) and if the controller manages to stabilize the nonlinear system (2.30) - (2.31), apparently the performance will be deteriorated. Therefore, actuators dynamics cannot be neglected safely always when using feedback linearisation and they show risk of destabilizing the overall system.

Example 1. To demonstrate the effect of unmodeled actuator dynamics on feedback linearisation, we consider a small example of nonlinear system and try to synthesize different controllers while studying the effect of unmodeled actuator dynamics at each case.

Consider the SISO nonlinear system given by:

$$\dot{x}_1 = x_2 \quad (2.33)$$

$$\dot{x}_2 = x_1 x_2 + x_1^2 + u \quad (2.34)$$

$$y = x_1 \quad (2.35)$$

We linearize the system using input-output feedback linearisation. Therefore, we have:

$$\dot{y} = \dot{x}_1 = x_2 \quad (2.36)$$

$$\ddot{y} = \dot{x}_2 = x_1 x_2 + x_1^2 + u \quad (2.37)$$

The relative degree of the system ($r = 2$) equals to the order of the system ($n = 2$) and there is no internal dynamics. To linearize the system we choose:

$$\ddot{y} = \vartheta. \quad (2.38)$$

Then, we have $\alpha(x) = -x_1 x_2 - x_1^2$ and $\beta(x) = 1$. The feedback linearisation law is:

$$u = \vartheta - x_1 x_2 - x_1^2. \quad (2.39)$$

The linearized system from ϑ to y is a double integrator system given by:

$$\begin{bmatrix} \dot{\zeta}_1 \\ \dot{\zeta}_2 \end{bmatrix} = \begin{bmatrix} 0 & 1 \\ 0 & 0 \end{bmatrix} \begin{bmatrix} \zeta_1 \\ \zeta_2 \end{bmatrix} + \begin{bmatrix} 0 \\ 1 \end{bmatrix} \vartheta \quad (2.40)$$

$$y = \begin{bmatrix} 1 & 0 \end{bmatrix} \begin{bmatrix} \zeta_1 \\ \zeta_2 \end{bmatrix} \quad (2.41)$$

We invoke now different controllers for the linearized system and observe the effect of unmodeled actuator dynamics in each case. Table 2.1 summarizes the used controllers and the transfer functions of the controller for each case.

Linearized Plant P(s)	Controller	Synthesis method
$1/s^2$	$\frac{0.54s^3 + 4.5s^2 + 4.75s + 1.31}{0.001s^4 + 0.034s^3 + 0.43s^2 + 1.83s + 1.08}$	\mathcal{H}_∞ loop shaping design
	$k_1 = 12, k_2 = 35, k_I = 30$	State feedback with integrator
	$k_d = 8.75, k_p = 10$	PD

Table 2.1: The synthesized controllers for the linearized system.

The step responses of the linearized system using the specified controllers are summarized in Figure 2.1.

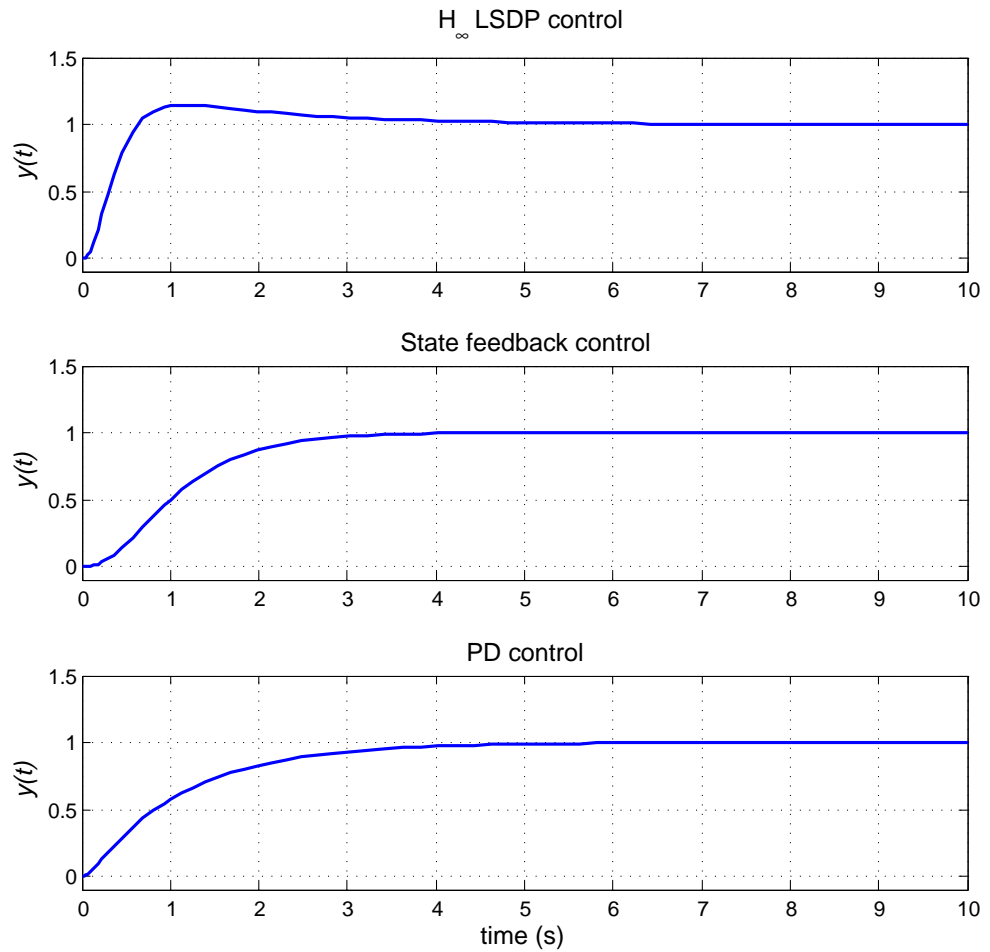


Figure 2.1: Step responses of the nonlinear system using input-output feedback linearisation associated with the specified controllers without considering actuator dynamics

To study the effect of unmodeled actuator dynamics on feedback linearisation, we consider a SISO LTI actuator system given by:

$$\dot{x}_a = -\frac{1}{t_a}x_a + \frac{1}{t_a}u_a \quad (2.42)$$

$$y_a = x_a \quad (2.43)$$

where t_a is the time constant of the actuator system and it indicates the speed of the actuator.

To impose the unmodeled actuator dynamics on the linearized system we have the mapping:

$$x_1 = \zeta_1 \quad (2.44)$$

$$x_2 = \zeta_2 \quad (2.45)$$

and then we have the perturbed plant as:

$$\dot{\zeta}_1 = \zeta_2 \quad (2.46)$$

$$\dot{\zeta}_2 = x_a + \zeta_1 \zeta_2 + \zeta_1^2 \quad (2.47)$$

$$\dot{x}_a = -\frac{1}{t_a} x_a + \frac{1}{t_a} (-\zeta_1 \zeta_2 - \zeta_1^2) + \frac{1}{t_a} \vartheta \quad (2.48)$$

$$y = \zeta_1 \quad (2.49)$$

We simulate the step response of the nonlinear system (2.46) - (2.49) using the same controller synthesized in Table 2.1 with $t_a \in [0.1 \ 0.5]$. This range of time constant is chosen based on a review of empirical data for UAV actuators, see Chapter 5. The responses of the system under the synthesized controllers with unmodeled actuator dynamics are summarized in Figure 2.2.

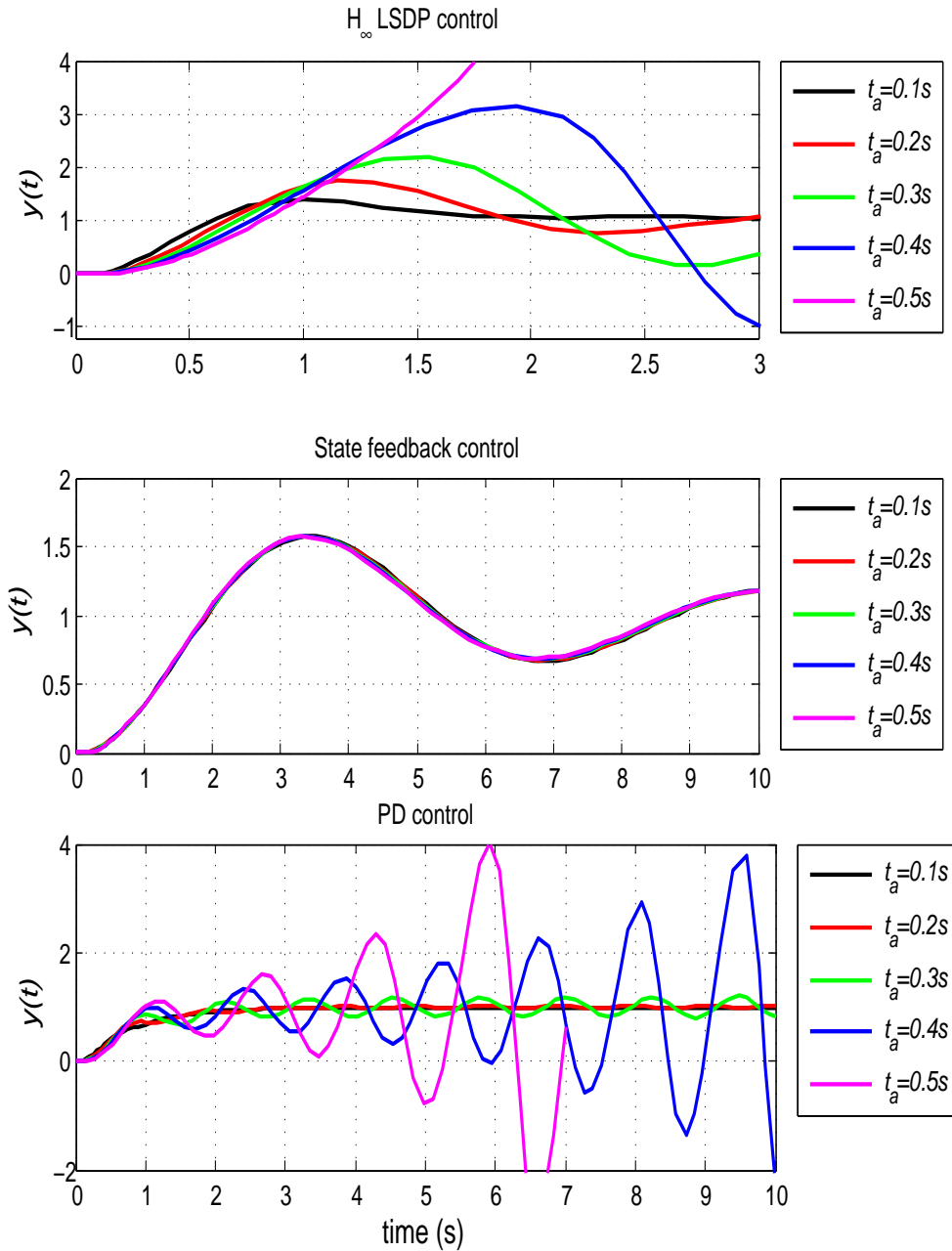


Figure 2.2: Step responses of the linearized system under the effect of first order unmodeled actuator dynamics.

It can be seen from Figure 2.2 that in case of the \mathcal{H}_∞ control and the PD controller, unmodeled actuator dynamic deteriorate the performance of the system up to a certain actuator speed and the system becomes unstable for slower actuators. When applying

the state feedback control with integrator, unmodeled actuator dynamics deteriorate the performance regardless of the speed of the dynamics.

For further analysis of the negative impact of actuator dynamics on feedback linearisation, we consider second order actuator dynamics as:

$$\dot{x}_{a_1} = x_{a_2} \quad (2.50)$$

$$\dot{x}_{a_2} = -\frac{1}{t_a}x_{a_2} + \frac{1}{t_a}u_a \quad (2.51)$$

$$y_a = x_{a_1} \quad (2.52)$$

Figure 2.3 shows the response of the system when imposing unmodeled second order actuator dynamics. In this case, the synthesized controllers fail to accommodate the actuator dynamics and the system becomes unstable regardless of how fast actuators are.

This example clarifies that unmodeled actuator dynamics cannot be neglected safely when using feedback linearisation regardless of how fast actuators are. Therefore, it is vital to model actuators and handle their dynamics before feedback linearisation can be implemented.

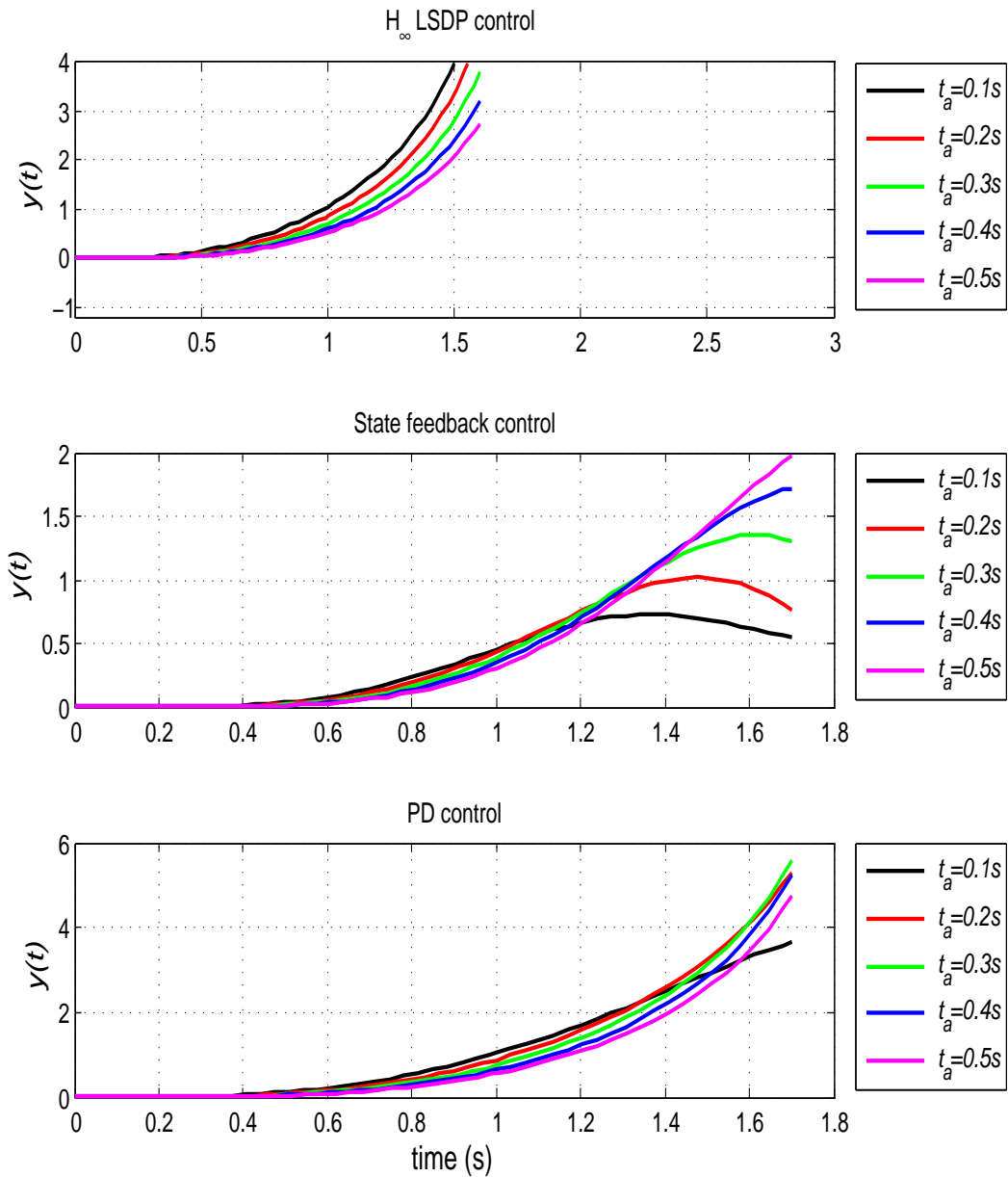


Figure 2.3: Step responses of the nonlinear system under the effect of second order un-modeled actuator dynamics when using input-output feedback linearisation associated with different controllers.

2.4 New Two Stage Feedback Linearisation to Handle Actuator Dynamics

The previous section shows the negative effect of unmodeled actuator dynamics on system performance when implementing feedback linearisation. In this section, we develop a two stage feedback linearisation algorithm to compensate actuator dynamics and maintain the validity of the linear control associated with feedback linearisation for the nonlinear system. In the proposed two stage algorithm, the first stage handles actuator dynamics using inner loop linearisation/compensation while the second stage is to design the outer loop and linearize the main nonlinear system. Compared with the direct way of including actuator dynamics in the overall system before implementing feedback linearisation, the proposed two stage algorithm simplifies the implementation of feedback linearisation and minimize the effect of actuators system uncertainty on the stability of the linearized system.

Assuming that the model of actuators system is available, consider a nonlinear MIMO fully actuated system represented by:

$$\dot{x} = f(x) + \mathbf{G}(x)u \quad (2.53)$$

$$y = h(x) \quad (2.54)$$

and a nonlinear actuators system given by:

$$\dot{x}_a = f_a(x_a) + \mathbf{G}_a(x_a)u_a \quad (2.55)$$

$$y_a = h_a(x_a) \quad (2.56)$$

where $x_a \in \mathbb{R}^{n_a}$ and $y_a, u_a \in \mathbb{R}^m$. $f(\cdot)$, $f_a(\cdot)$ and $h(\cdot)$, $h_a(\cdot)$ as well as the column vectors of \mathbf{G} and \mathbf{G}_a are assumed sufficiently smooth in the domains \mathbb{D} , $\mathbb{D}_a \subset \mathbb{R}$ respectively where the matrices \mathbf{G} and \mathbf{G}_a are given by:

$$\mathbf{G} = \begin{bmatrix} g_1 & g_2 & \cdots & g_m \end{bmatrix}, \quad (2.57)$$

$$\mathbf{G}_a = \begin{bmatrix} g_{a1} & g_{a2} & \cdots & g_{am} \end{bmatrix}. \quad (2.58)$$

The complete nonlinear system including actuator dynamics can be represented by:

$$\dot{x} = f(x) + \mathbf{G}(x)y_a \quad (2.59)$$

$$y = h(x) \quad (2.60)$$

and

$$\dot{x}_a = f_a(x_a) + \mathbf{G}_a(x_a)u_a \quad (2.61)$$

$$y_a = h_a(x_a) \quad (2.62)$$

$$(2.63)$$

We propose now two stage feedback linearisation algorithm to linearize the nonlinear UAV system . In the first stage, we linearize and control the actuator system assuming that actuators states are available, the actuators system has a well-defined relative degree of r_a and the dynamics of the actuators are invertible. We linearize the nonlinear actuator system by defining the feedback linearisation law for the actuator system as:

$$u_a = \alpha_a + \beta_a^{-1} \vartheta_a \quad (2.64)$$

with α_a and β_a are defined respectively as in Eq. (2.15) and (2.14) with regard to the actuators nonlinear system. The input ϑ_a is defined as:

$$\vartheta_a = \begin{bmatrix} y_{a1}^{(r_{a1})} \\ y_{a2}^{(r_{a2})} \\ \vdots \\ y_{am}^{(r_{am})} \end{bmatrix} \quad (2.65)$$

where

$$y_{a_i}^{(r_{a_i})} = L_{f_a}^{r_{a_i}} h_{a_i} + \sum_{j=1}^m L_{g_{a_j}} L_{f_a}^{r_{a_i}-1} h_{a_i} u_{a_j}, \quad 1 \leq i \leq m. \quad (2.66)$$

and

$$r_a = r_{a1} + r_{a2} + \cdots + r_{am} \quad (2.67)$$

Now, the linearized actuators system can be represented by:

$$\dot{\zeta}_a = \mathbf{A}_a \zeta_a + \mathbf{B}_a \vartheta_a \quad (2.68)$$

$$y_a = \mathbf{C}_a \zeta_a \quad (2.69)$$

such as \mathbf{A}_a , \mathbf{B}_a , \mathbf{C}_a are defined according to Eq. (2.12) with regard to the actuators system. ζ_a is a new actuator state vector defined throughout the mapping $\zeta_a = T_a(x_a)$.

System (2.68) - (2.69) is a MIMO decoupled system in which each channel can be handled individually.

We consider now the SISO System of the i^{th} actuator channel. We have:

$$\zeta_{a_i} = \begin{bmatrix} h_i \\ \dot{h}_i \\ \vdots \\ h_i^{(r_{a_i})} \end{bmatrix} = \begin{bmatrix} \zeta_{i_1} \\ \zeta_{i_2} \\ \vdots \\ \zeta_{i_{(r_{a_i}-1)}} \end{bmatrix} \quad (2.70)$$

and therefore we can write the dynamics of the the i^{th} channel as:

$$\dot{\zeta}_{i_1} = \zeta_{i_2} \quad (2.71)$$

$$\dot{\zeta}_{i_2} = \zeta_{i_3} \quad (2.72)$$

$$\vdots \quad (2.73)$$

$$\dot{\zeta}_{i_{(r_{a_i}-1)}} = \vartheta_{a_i} \quad (2.74)$$

$$y_{a_i} = \zeta_{i_1} \quad (2.75)$$

where $1 \leq i \leq m$.

The desire is to make the linearized actuator system follows a trajectory of reference signal y_d . This reference input represents the feedback linearisation control law of the outer loop that will be discussed later, i.e. $y_d = u$. For the i^{th} actuator channel we have

$y_{d_i} = u_i$. We define a new strict feedback error systems as:

$$e_{i_1} = \zeta_{i_1} - u_i \quad (2.76)$$

$$e_{i_2} = \zeta_{i_2} - z_{i_1} - \dot{u}_i \quad (2.77)$$

$$\vdots \quad (2.78)$$

$$e_{i_{r_{a_i}}} = \vartheta_{a_i} - z_{i_{(r_{a_i}-1)}} - u_i^{(r_{a_i}-1)} \quad (2.79)$$

where z_{i_k} , $1 \leq k \leq r_{a_i} - 1$ is a Backstepping control law that is used to achieve stability and convergence of the overall error system. We design z_{i_k} using Lyapunov function V_{i_k} such that \dot{V}_{i_k} is semidefinite. Following [39], z_{i_k} can be designed as:

$$z_{i_k} = -e_{i_{k-1}} - c_{i_k} e_{i_k} + \sum_{j=1}^{k-1} \left(\frac{\partial z_{i_{(j-1)}}}{\partial \zeta_{i_j}} \zeta_{i_{(j+1)}} + \frac{\partial z_{i_{(j-1)}}}{\partial u_i^{(j-1)}} u_i^{(j)} \right) \quad (2.80)$$

The candidate for the Lyapunov function is:

$$V_{i_k} = V_{i_{k-1}} + \frac{1}{2} e_{i_k}^2 \quad (2.81)$$

with $V_{i_1} = e_{i_1}^2$.

The final control law for the i^{th} channel is:

$$\vartheta_{a_i} = z_{i_{(r_{a_i}-1)}} + u_i^{(r_{a_i})} \quad (2.82)$$

and that leads to:

$$\dot{V}_{i_{r_{a_i}}} = - \sum_{j=1}^{r_{a_i}} c_{i_j} e_{i_j}^2 \leq 0 \quad (2.83)$$

The resulting error system for the i^{th} channel is:

$$\begin{bmatrix} \dot{e}_{i_1} \\ \vdots \\ \dot{e}_{i_{r_{a_i}}} \end{bmatrix} = \begin{bmatrix} -c_{i_1} & 1 & 0 & \cdots & 0 \\ -1 & -c_{i_2} & 1 & \cdots & 0 \\ 0 & -1 & \ddots & \ddots & \vdots \\ 0 & 0 & \cdots & -1 & -c_{i_{r_{a_i}}} \end{bmatrix} \begin{bmatrix} e_{i_1} \\ \vdots \\ e_{i_{r_{a_i}}} \end{bmatrix} \quad (2.84)$$

The error system in Eq. (2.84) is globally uniformly stable at equilibrium $e_i = 0$ and $\lim_{t \rightarrow \infty} e_i(t) = 0$ which means that the global asymptotic tracking is achieved, where e_i is defined as:

$$e_i = \begin{bmatrix} e_{i_1} \\ \vdots \\ e_{i_{r_{a_i}}} \end{bmatrix} \quad (2.85)$$

The proof can be obtained easily using Lyapunov theory. The transient performance of the error system can be controlled by the design parameters c_{i_k} . In general, increasing c_{i_k} will improve the transient performance of the error system [39].

We repeat the previous Backstepping tracking design for all actuator channels, i.e., $1 \leq i \leq m$, and finally we have:

$$\vartheta_a(T_a(x_a), u, \dot{u}, \ddot{u}, \dots, u^{(a_1)}, \dots, u^{(a_m)}) = \begin{bmatrix} \vartheta_{a_1} \\ \vdots \\ \vartheta_{a_m} \end{bmatrix} \quad (2.86)$$

The design of the inner loop ensures that y_a converges to u asymptotically for all initial values.

Assuming that the inner loop has high and sufficient bandwidth, we can put $y_a \approx u$ and then we can now perform the second stage by implementing input-output feedback linearisation of the main nonlinear system using the standard procedure described in Section 2.2. Figure 2.4 represents a block diagram of the developed two stage feedback linearisation for nonlinear systems including actuator dynamics.

The proposed two stage linearisation procedure is straightforward and simple compared with the standard method of handling actuator dynamics by including these dynamics in the overall system and consider the total system as a two cascaded systems. For instance, let's consider a nonlinear system represented by (2.53) -(2.54) and a nonlinear actuators system given by (2.55) - (2.56). The total model of the system including actuator dynam-

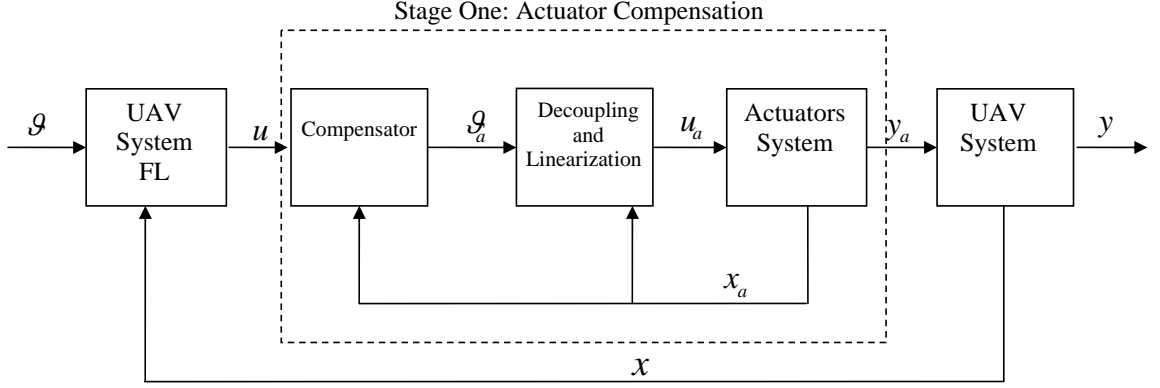


Figure 2.4: Block diagram of the proposed two stage feedback linearisation.

ics can be written as a two cascaded nonlinear system:

$$\dot{x} = f(x) + \mathbf{G}(x)h(x_a) \quad (2.87)$$

$$\dot{x}_a = f_a(x_a) + \mathbf{G}_a(x_a)u_a \quad (2.88)$$

$$y = h(x) \quad (2.89)$$

System (2.87) - (2.88) can be linearized as one system using standard feedback linearisation. However, this method is complex and requires derivation along both vector states x_a and x , which means that the vector functions $f(\cdot)$, $g_i(\cdot)$, $f_a(\cdot)$ and $g_{a_i}(\cdot)$ need to be smooth and diffeomorphic up to the level $n + n_a$. A comparison study between the proposed two stage feedback linearisation and the standard linearisation of the whole system will be conducted when considering the example of Tri-rotor UAV in Chapter 5.

Remark 1. The proposed two stage feedback linearisation is developed for the general case of nonlinear actuator systems. The linear actuator system represents a special case of the general nonlinear case. The first stage includes two steps, in the first step the nonlinear system is decoupled and linearized while the second step represents the compensation process via Backstepping control. In case of a linear actuator system, stage 1 does not need to include the linearisation process and hen it simplified to be a tracking problem using Backstepping control. Therefore, stage one can be referred to as "dynamic inversion" stage to include both cases of linear and nonlinear actuator systems.

To demonstrate the proposed linearisation algorithm, we consider again Example 1 and apply the proposed two stage feedback linearisation procedure.

Stage 1 We consider in this stage the actuator dynamics given in (2.50) -(2.52). The goal is to design an inner loop feedback controller so that y_a tracks the reference signal u . We define the new error states as:

$$e_1 = x_{a_1} - y_d \quad (2.90)$$

$$e_2 = x_{a_2} - z_1 - \dot{y}_d \quad (2.91)$$

and then we have the error system as:

$$\dot{e}_1 = \dot{x}_{a_1} - \dot{y}_d \quad (2.92)$$

$$\dot{e}_2 = \dot{x}_{a_2} - \dot{z}_1 - \ddot{y}_d \quad (2.93)$$

$$(2.94)$$

We have from the dynamics of the system:

$$\dot{x}_{a_1} = x_{a_2} \quad (2.95)$$

$$\dot{x}_{a_2} = -\frac{1}{t_a}x_{a_2} + \frac{1}{t_a}u_a \quad (2.96)$$

Therefore, the error system is:

$$\dot{e}_1 = x_{a_2} - \dot{y}_d \quad (2.97)$$

$$\dot{e}_2 = -\frac{1}{t_a}x_{a_2} + \frac{1}{t_a}u_a - \dot{z}_1 - \ddot{y}_d \quad (2.98)$$

We have from Eq. (2.91):

$$\dot{y}_d = -e_2 + x_{a_2} - z_1 \quad (2.99)$$

and therefore:

$$\dot{e}_1 = x_{a2} - (-e_2 + x_{a2} - z_1) \quad (2.100)$$

$$= e_2 + z_1 \quad (2.101)$$

$$\dot{e}_2 = -\frac{1}{t_a}x_{a2} + \frac{1}{t_a}u_a - \dot{z}_1 - \ddot{y}_d \quad (2.102)$$

We define a Lyapunov function:

$$V_1 = \frac{1}{2}e_1^2 \quad (2.103)$$

whose derivative is:

$$\dot{V}_1 = e_1\dot{e}_1 \quad (2.104)$$

$$= e_1(e_2 + z_1) \quad (2.105)$$

Then, we choose:

$$z_1(x_1) = -c_1e_1 \quad (2.106)$$

with $c_1 > 0$ a design parameter. Then, we have:

$$\dot{V}_1 = -c_1e_1^2 + e_1e_2 \quad (2.107)$$

The term e_1e_2 will be canceled in next step.

Let us now consider the equation:

$$\dot{e}_2 = -\frac{1}{t_a}x_{a2} + \frac{1}{t_a}u_a - \dot{z}_1 - \ddot{y}_d \quad (2.108)$$

We define a Lyapunov function:

$$V_2 = V_1 + \frac{1}{2}e_2^2 \quad (2.109)$$

whose derivative is:

$$\dot{V}_2 = \dot{V}_1 + e_2 \dot{e}_2 \quad (2.110)$$

$$= -c_1 e_1^2 + e_1 e_2 + e_2 (\dot{x}_{a2} - \dot{z}_1 - \ddot{y}_d) \quad (2.111)$$

$$= -c_1 e_1^2 + e_1 e_2 + e_2 \left(-\frac{1}{t_a} x_{a2} + \frac{1}{t_a} u_a - \dot{z}_1 - \ddot{y}_d \right) \quad (2.112)$$

Then, we choose the control input as:

$$u_a = t_a \left(-c_2 e_2 - e_1 + \dot{z}_1 + \ddot{y}_d + \frac{1}{t_a} x_{a2} \right) \quad (2.113)$$

with c_2 a positive design parameter, and this gives:

$$\dot{V}_2 = -c_1 e_1^2 - c_2 e_2^2 \leq 0 \quad (2.114)$$

We have:

$$\dot{z}_1 = -c_1 e_1 \quad (2.115)$$

$$= -c_1 (e_2 + z_1) \quad (2.116)$$

and therefore the control law is given by:

$$u_a = t_a \left[-\left(c_1 + c_2 - \frac{1}{t_a} \right) x_{a2} - (c_1 c_2 + 1) x_{a1} + (c_1 c_2 + 1) y_d + (c_1 + c_2) \dot{y}_d + \ddot{y}_d \right] \quad (2.117)$$

We choose c_1 and c_2 high enough to guarantee $y_a \approx u$.

stage 2 This stage includes the feedback linearisation of the original system (2.33) - (2.34) neglecting actuator dynamics. Eq. (2.39) gives the feedback linearisation law of the outer loop in regard to the main nonlinear system.

We consider now the same controllers developed in Table 2.1 to demonstrate the performance of the system under the two stage feedback linearisation. Figure 2.5 depicts the performance of the system under the various synthesized controllers.

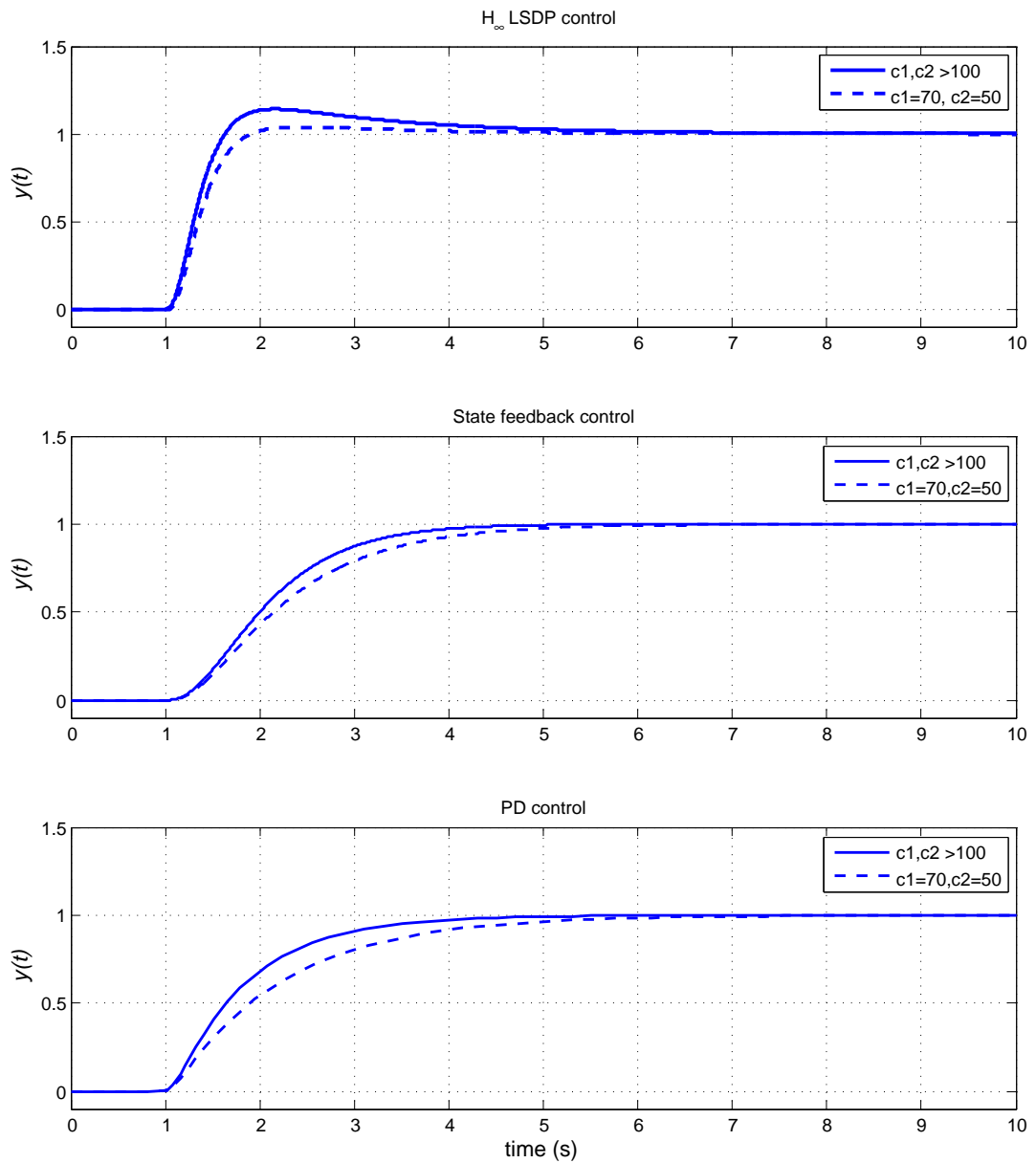


Figure 2.5: Step responses of the system using the proposed two stage feedback linearisation associated with different controllers.

The graphs depicted in Figure 2.5 shows that with large value of c_1 and c_2 the performance of the system is typical to the nominal plant without actuators shown in Figure 2.1. The compensation of the actuator dynamics using the proposed two stage feedback linearisation succeeds to maintain the validity of the feedback linearisation for the main nonlinear system without actuators.

2.5 Summary

This chapter shows the vital importance of actuator dynamics for the control design of UAV nonlinear systems when using dynamic inversion. The conducted example shows that regardless of how fast actuators are, actuator dynamics can destabilize the linearized system if not modeled when using input-output feedback linearisation. To implement input-output feedback linearisation in existence of actuator dynamics, a two stage feedback linearisation method is developed. The proposed method aims to simplify the implementation of feedback linearisation when actuator dynamics are considered and to minimize the effect of actuator model uncertainty on the whole feedback linearisation of the main UAV system. The result of this chapter will be investigated again later in this thesis when studying the design and control of the Tri-rotor UAV in Chapter 5.

Chapter 3

An Explicit Design Procedure for Propulsion Systems of Electrically Driven VTOL UAVs

This chapter proposes a systematic design procedure for electric propulsion systems of VTOL UAVs based on the design specifications that are given in terms of the required thrust, permissible weight of the propulsion system and required flight time. The solution space of the proposed design methodology is a subset of commercially available products, which enhances the applicability of the procedure to the practicing community. For the purpose of the proposed design procedure, we introduce a mathematical model for the thrust and mechanical power of fixed pitch propellers.

Section 3.2 presents a description of electric propulsion systems along with mathematical models of the main components to be considered in the design procedure. In Section 3.3, the proposed design procedure is presented. Some concluding remarks and summary are drawn in Section 3.4.

3.1 Introduction

A key part of UAV systems is the propulsion system that generates the required lifting force for all flying modes; i.e., taking-off, hovering, forward flying, maneuvering and landing. In practice, different types of propulsion systems exist, and the selection of best suitable system depends on many factors such as the vehicle size and structure, the operational environment, the payload and flight time of the vehicle [40, 41]. Therefore, for different UAV designs and applications, designers choose different propulsion systems; e.g., electric propulsion systems, jet engines or reciprocating piston engines. Due to their advantages, electric propulsion systems are widely used in UAV systems and particularly in mini UAVs and research platforms [41, 40, 42, 43]. The advantages and disadvantages of electric propulsion systems are summarized in [40]. The advantages of electric propulsion systems are inherited from electric motors that are reliable and can be controlled easily. Moreover, electric motors are less noisy, require less maintenance and have no emissions compared to jet and internal combustion (IC) engines. On the other side, electric propulsion systems reports some disadvantages due to sensitivity to water and conductive liquids. Another point in the negative side of propulsion systems is related to electric batteries. The energy of electric batteries is still far shorter than that of liquid fuels, which results in shorter flight time. However, the available electric batteries have adequate power capacities for short-flight missions and demonstration purposes. Nevertheless, electric propulsion systems are still dominant in small UAV systems and research platforms. This in turn calls for more focusing on the design and operation of electric propulsion systems.

3.1.1 Why A Design Procedure Is Needed?

Ideally, an electric propulsion system comprises of an electric motor powered by an energy source unit (battery pack) and a propeller coupled with the motor shaft to generate the required thrust while rotating at a specific speed [41]. The voltage supplied from the battery pack controls the speed of the motor that in turn regulates the generated thrust. In addition to the rotational speed, the generated thrust is a function of some other factors

like the radius and pitch angle of the propeller and the air density as will be shown later in Section 3.2.1.

Due to the considerable relative weight of electric batteries and motors compared to other components of UAV systems, the chosen electric propulsion system has an impact on the total weight of the vehicle which in turn affects the payload capability and the maneuverability of the UAV. Moreover, the power consumption of electric motors and the capacity of electric batteries are important factors in specifying the flight time of the UAV. Therefore, the chosen electric propulsion system needs to be designed effectively in order to improve the thrust-to-weight ratio of the system and decrease the weight of the vehicle. This in turn enhances the payload capability, the maneuverability and the operational flight time of the UAV.

To this end, few attempts have been reported in literature to systematically enhance the efficiency of electric propulsion systems design. In [44], it is shown how a pack of Solid Oxide Fuel Cell (SOFC) with various duty cycles of the supplied voltage can be used to generate different amounts of thrust while utilizing a random selection of motor-propeller assemblies. The authors focus only on a special type of fuel cell to supply power to the electric motor while the selections of the motor and propeller are not discussed. In [45], a design strategy is proposed to select the propulsion system components from commercially available products. The authors suggest an algorithm that uses a compact model of the propeller/motor assembly and assumes that this model is known and available to give the needed inputs to the design algorithm such as the thrust-to-current ratio, torque-to-current ratio and voltage-to-current ratio of the propeller-motor assembly. In the field of model aircraft and mini UAVs, manufacturers typically do not supply the required highly specialized information of propellers and electric motors. Instead, the thrust model of available propellers needs to be obtained via a theoretical formula or an experimental procedure, which is not always easy to do. For instance, wind-tunnel based experiments are conducted in [46] to extract the thrust and power coefficients for some propellers from which the thrust model can be obtained. However, the tested propellers are limited to specific range of size and cannot be used in wide applications. In [47, 48, 49, 50], the used electric propulsion systems and the whole UAV designs are adopted from existing commercial radio controlled aircraft toys. This choice restricts the payload capabilities and narrows the range of applications of the UAV. In a wider scope, there exist some software

packages to design electric propulsion systems [51, 52]. In these softwares, a routine is used to analyze the supplied specifications of the UAV, and then suggests a set of components to construct the required electric propulsion system. However, the algorithms of these software are ambiguous and the suggested components do not always exist commercially in the market. As a result, a global search is followed to obtain the best matching existing alternative products which might deviate from the optimal solution.

In this chapter, a systematic design procedure is proposed to select the components of electric propulsion systems for VTOL UAVs. Prior to the design steps, the technical specifications of each component are discussed in detail and a mathematical model for the propeller thrust that is explicit and easy to use for design purposes is derived. In the proposed design strategy, two goals are considered: one is to increase the payload capacity of the UAV by reducing the total weight of the propulsion system. The other goal is to increase the flight time by choosing the best possible battery pack.

3.2 Electric Propulsion Systems

A single electric propulsion unit consists mainly of an energy storage unit (battery pack), an electronic speed control unit (ESC), an electric motor (usually brushless DC (BLDC) motor) and a propeller. The shaft of the electric motor is coupled with one propeller to produce the required thrust. The power from the battery to the electric motor is fed through the ESC that controls the speed of the motor by regulating the input voltage of the motor which in turn controls the generated thrust. The structure of the electric propulsion system and the number of the propulsion units required to drive the UAV depends on the vehicle's structure, size and flying mode. For instance, different arrangements can be made to transmit the mechanical power from the motor shaft to one or more propellers in order to generate the required thrust. In addition, the energy storage unit, depending on the size and capacity, can supply power to one or more motors simultaneously. In Figure 3.1, a generic operational block diagram of an electric propulsion unit is depicted. In general, the components of electric propulsion systems are selected to meet the design

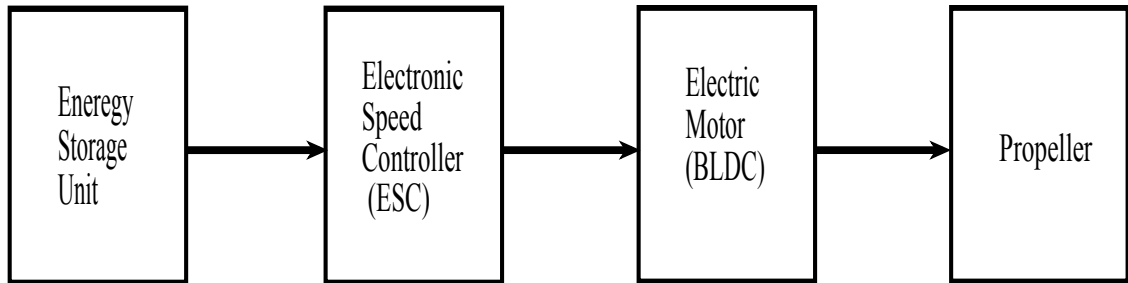


Figure 3.1: Structure and elements of an electric propulsion unit.

requirements of sufficient static thrust for taking off and hovering, minimum power consumption to generate the required thrust, minimum weight of the propulsion system, and maximum flight time [53]. These design parameters are reflected directly by the specifications of the components of the constructed electric propulsion system. For instance, the size, shape and rotational speed of the propeller determine the maximum thrust it can generate. The constants of the electric motor specify the maximum torque and rotational speed that can be produced at the shaft and these should match with the propeller requirements to generate the specified thrust. The electric capacity of the battery should be sufficient to operate the motor at the specified rotational speed for the required flight time while in the same time the size and weight of the battery should fit the structure and design of the vehicle. In the following subsections, the principle components of electric propulsion systems and the important design factors of each component are highlighted. Side by side, the technical specifications of each component along with the mathematical model that represent the component is illustrated to make the design steps easy to use for the practicing community.

3.2.1 Propellers

Propeller are the thrust generating components of propulsion systems. The generated thrust is mainly a function of the diameter, the pitch angle and the rotational speed of the propeller. To this end, different theories are proposed in the literature to elicit an

accurate mathematical model for the developed thrust by air propellers [54, 55, 56]. In general, the available thrust and power models, e.g. the blade element model, need an exact description of the geometric shape of the propeller in order to obtain the thrust and power coefficients required to derive the thrust model. In the market of model aircraft and mini UAVs, the geometric descriptions of available propellers are not available and the power/thrust coefficients are not supplied. An alternative way to get the missing information is to use wind tunnel experiments to extract the thrust curves of the given propeller(s) [57, 46]. The wind tunnel experiment is not always available or easy to perform, and therefore, an explicit mathematical thrust model that requires less information about propellers is useful. The methodology adopted in this chapter is to use the simplest possible model to bring the design to the neighborhood of the optimized choice of components as it is futile to require experiments or design methods that cannot be possibly implemented in practice. In this section, a new mathematical model of air propellers based on [54, 55, 56] is derived. This model is used latter in Section 3.3 to develop the proposed design procedure for electric propulsion systems of VTOL UAVs.

Using the momentum theory [55] while considering propellers as actuator disks and with the following assumptions: (i) ideal fluid (air in this case) with no energy dissipation through friction or energy transfer to the ideal fluid, (ii) no viscosity and compressibility of the air and (iii) no elastic bending of the propellers, the static thrust f_p developed by a propeller p is given as:

$$f_p = 2\mu_a A_p v_a^2, \quad (3.1)$$

where μ_a is the air density, $A_p = \pi R_p^2$ is the disk area of the propeller, R_p is the radius of the propeller and v_a is the induced velocity of the incoming air by the propeller.

For constant pitch propellers and uniform airflow, the induced velocity is given by:

$$v_a = \kappa_p \omega_p R_p, \quad (3.2)$$

where ω_p is the rotational speed of the propeller and κ_p is the inflow constant that depends on the propeller type and shape. The inflow constant for uniform inflow can be

approximated [56] as:

$$\kappa_p = \frac{\sigma_p k_1}{16} \left[\sqrt{\left(1 + \frac{64}{3\sigma_p k_1} \theta_p\right)} - 1 \right], \quad (3.3)$$

where θ_p is the pitch angle of the propeller, k_1 is known as the two-dimensional lift slope factor¹ and σ_p is the solidity factor that is defined by:

$$\sigma_p = \frac{\text{blade area}}{\text{disk area}} = \frac{n_p d_p R_p}{\pi R_p^2} = \frac{n_p d_p}{\pi R_p}, \quad (3.4)$$

where n_p is the number of blades of the propeller and d_p represents the chord length of the blade. For a propeller with varying chord length, d_p is taken as the average chord length of the blade. By using Equations (3.2) - (3.4), the generated thrust can be written as:

$$f_p = \frac{\mu_a}{128\pi} \left(\frac{n_p^2 d_p^2 k_1^2}{R_p^2} \right) \omega_p^2 R_p^4 \left(\sqrt{\left(1 + \frac{64\pi R_p}{3n_p d_p k_1} \theta_p\right)} - 1 \right)^2. \quad (3.5)$$

For simplicity of representation, a new variable C_p is defined as a function of the number of blades n_p , the chord-to-radius ratio d_p/R_p and the pitch angle θ_p :

$$C_p = \frac{d_p}{R_p} \left(\sqrt{\left(1 + \frac{64\pi}{3n_p \frac{d_p}{R_p} k_1} \theta_p\right)} - 1 \right). \quad (3.6)$$

Using C_p , the developed thrust f_p can be written as:

$$f_p = \frac{\mu_a n_p^2 k_1^2}{128\pi} \omega_p^2 R_p^4 C_p^2. \quad (3.7)$$

Using Eq. (3.7), one can calculate the thrust f_p generated by a propeller p of radius R_p and pitch angle θ_p when rotating at rotational speed ω_p . Assuming that C_p is radius independent due to the fact that the ratio d_p/R_p can be considered constant for a family of propellers², the radius of the propeller has more effect on the generated thrust than other

¹In this thesis, k_1 is assumed constant with a value of $k_1 = 5.7$ [56].

²As the radius of the propeller increases, the average chord length increases in the same rate and hence $d_p/R_p \approx \text{constant}$.

variables: $f_p \propto R_p^4$. In addition, Eq. (3.7) can be used to calculate the rotational speed necessary to generate a given thrust f_p by a propeller of radius R_p and pitch angle θ_p as following:

$$\omega_p = \sqrt{\frac{f_p}{R_p^4 C_p^2} \frac{128\pi}{\mu_a n_p^2 k_1^2}}. \quad (3.8)$$

An experiment based validation is conducted in next section to test the validity of the thrust model represented by Eq. (3.7).

In order to generate the required thrust f_p , an external mechanical power P_{f_p} is needed (supplied by a motor) to rotate the propeller at the particular rotational speed ω_p . Following the momentum theory, this mechanical power is defined as the power needed to overcome the drag torque and mathematically is given by [54]:

$$P_{f_p} = 2\mu_a A_p (v_\infty + v_a)^2 v_a, \quad (3.9)$$

where v_∞ is the air speed in the direction of the propeller. μ_a , A_p and v_a are defined as in Eq. (3.1). For static thrust, the directional speed of the air toward the propeller is zero; i.e., $v_\infty = 0$, and then Eq. (3.9) is simplified to:

$$P_{f_p} = 2\mu_a A_p v_a^3. \quad (3.10)$$

Using Equations (3.2) - (3.4) yields:

$$P_{f_p} = \frac{\mu_a}{2048\pi^2} (n_p k_1)^3 (\omega_p C_p)^3 R_p^5. \quad (3.11)$$

For a given propeller p , the term $\omega_p C_p$ can be obtained from Eq. (3.7) as a function of the generated thrust f_p and the radius R_p , and then substituted into Eq. (3.11) to give the relationship between the thrust f_p and the power P_{f_p} required to generate this thrust:

$$P_{f_p} = \frac{1}{\sqrt{2\mu_a\pi}} \frac{(f_p)^{\frac{3}{2}}}{R_p}. \quad (3.12)$$

Eq. (3.12) shows a mapping between the generated thrust by a propeller of radius R_p and the power requirement to rotate the propeller. In practice, this relationship is beneficial

as it involves only few variables; the propeller radius and air density. For instance, to calculate the power that is necessary to generate a specific thrust f_p , the designer needs only to know the radius of the propeller and the air density.

Pitch Length vs. Pitch Angle

Broadly speaking, the pitch of commercial propeller available in the market is specified in terms of pitch length β_p rather than pitch angle θ_p . The pitch length is defined as the distance that the propeller would move forward in each revolution without slipping [54]. However, in order to use Eq. (3.7) or Eq. (3.11) to calculate the developed thrust f_p or the power P_{f_p} , the pitch angle must be known a priori for obtaining C_p (see Eq. (3.6)). In twisted propellers, the pitch angle and pitch length vary along the radius r , where r is the distance from the center of the propeller to the point of measurement, i.e., $0 \leq r \leq R_p$. The relationship between the pitch length $\beta(r)$ and the pitch angle $\theta(r)$ at a radius r is given by:

$$\beta(r) = 2\pi r \tan(\theta(r)). \quad (3.13)$$

For constant-pitch length propellers³, the pitch length is constant along the radius, i.e., the pitch angle $\theta(r)$ decreases as r increases so that the pitch length $\beta(r)$ remains fixed along the radius span. Empirically, it was shown in [56] that for the case of constant pitch length propellers, the pitch angle at the radius $r = 0.75R_p$ is sufficient to be used to calculate the generated thrust of the propeller. Therefore, θ_p is obtained as following:

$$\theta_p = \theta(0.75R_p) = \arctan\left(\frac{2\beta_p}{3\pi R_p}\right), \quad (3.14)$$

where β_p and R_p are known.

For the purpose of propulsion systems design, a simplified propeller model is necessary to get a quantitative measure of important physical quantities, e.g. thrust and power, and the relationships between them. In this section, Eq. (3.7), Eq. (3.11) and Eq. (3.12)

³In this thesis, propellers are assumed to be constant pitch length (shortly called constant-pitch propellers) unless specified.

fulfill this objective easily when the propeller's radius and pitch angle are known a priori. However, the proposed design procedure is similarly applicable for any other advanced propeller model available in hand.

3.2.2 Propeller Model Verification

The propeller model shown in the previous section is based on an assumption of constant inflow and incompressible air. In practice, these assumptions might be questionable. In order to verify the derived model and show that it is adequate for the design purpose, an experiment has been conducted to compare the actual thrust developed by a range of propellers with the calculated values of thrust based on Eq. (3.7). The thrust is measured using the testbed arrangement shown in Figure 3.2.



Figure 3.2: Test rig for thrust model verification.

A DC motor (Himaxx HC5030-390) is used to spin the propellers and generate thrust. The motor-propeller assembly is mounted on the top edge of a balancing arm that is fixed in the middle on a fulcrum to allow free movement around the center. A weighing scale is placed under the other end of the arm. The system is fixed so that the arm is still

and perfectly horizontal. As the propeller spins, it generates a lifting force transmitted to a push force on the scale at the other end. According to Newton's second law, the generated thrust is equal to the read values on the scale times the Earth's gravity. To enhance the accuracy of the measurements, the shape of the arm is built in such a way to minimize its negative effect against the net generated force. In addition, the ground effect on the measured thrust is minimized by mounting the equipment about 1 m high above the ground. The experiment is repeated for different propellers to measure the generated thrust. The propellers are chosen such as they match the motor load specifications.

Three different sizes of propellers⁴, 16"×8", 17"×10" and 18"×10", are used in this experiment to generate thrust at different rotational speeds. The same propellers are considered in Eq. (3.7) to calculate the predicted thrust for the same range of rotational speeds used in experiment. Figure 3.3 plots the measured thrust and the calculated thrust for each propeller vs. the rotational speed of the propeller.

⁴Each propeller is denoted by: diameter × pitch length. The inch (") is used to be the measurement unit of the propellers' dimensions for consistency with the commercial specifications used in the chosen propellers that follow the American standards.

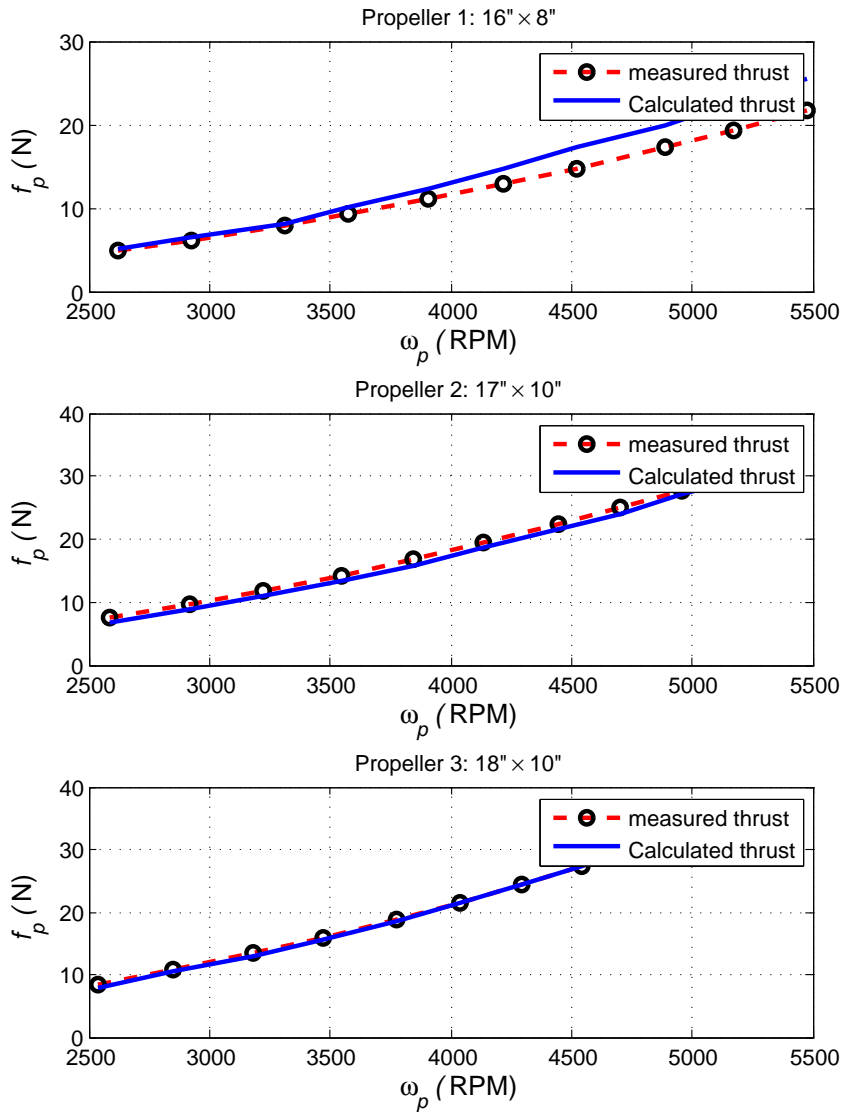


Figure 3.3: Measured thrust and calculated thrust vs. rotating speed for three different propellers.

In this figure, the thrust curves indicate that the derived model of the generated thrust has good approximation to the measured thrust. The worst case exists in the smallest propeller (16" x 8") with a maximum discrepancy of 11.56% between the measured thrust and the calculated thrust for the plotted range of rotation speed. The maximum error between the two thrust values decreases to be 5.6% in the second propeller (17" x 10")

and it is only 1.52% in the largest propeller (18" × 10") for the plotted range of the rotation speed. Moreover, the derived model overestimates the real generated thrust for the smallest propeller while it underestimates the generated thrust for the other two propellers.

The result of this experiment can be interpreted in light of the simplification of the momentum theory and the assumptions made while deriving the thrust formula. The assumption of uniform inflow seems to be reasonable for large blade propellers. As the diameter of the propeller decreases, the inflow becomes disturbed and not uniform any more. The impact of the blade size increases proportional to the rotational speed of the propeller, and in this case the assumption of a uniform flow becomes questionable.

In conclusion, we can say that for the purpose of propulsion systems design, Eq. (3.7) represents a good approximation for the thrust model of air propellers within specific range of radius and pitch sizes. For propellers outside this range, a safety margin needs to be considered to compensate for the inaccuracy of the derived thrust model. If a more accurate model is sought for the thrust, it can be obtained by using the element blade theory or any other alternative in hand. It can follow also that the power model in Eq. (3.11) has a similar accuracy to that obtained in the thrust model. However, the power model is of higher order in terms of the rotation speed ω_p , which puts more limitation to the accuracy of power model for high rotational speed and small propellers.

3.2.3 Electric Motors

Choosing an electric motor for the required electric propulsion system is an important task. The motor should have the ability to spin the propeller connected to its shaft at a certain speed to generate the required thrust. Moreover, the selected motor must fit into the weight and size requirements of the vehicle. The specifications of the chosen motor also affect the weight and size of the power supply needed to run the motor, which in turn affects the size and weight of the vehicle. The general criteria for choosing an electric motor for the propulsion system are: (i) enough power to spin the propeller to generate the required amount of thrust, (ii) rotational speed capability that matches the required rotational speed of the propeller, and (iii) high torque-to-weight ratio. There are different

types of electric motors available commercially that can be used for the electric propulsion system. Recently, brushless DC (BLDC) motors have gained enormous popularity in UAV applications due to the high torque-to-weight ratio, high efficiency, low noise level, high reliability and long lifetime of these motors [58]. In general, BLDC motors are more expensive than conventional DC motors with brushes, yet, they are much more efficient [59]. BLDC motors exist in a wide range of sizes, weights, power ratings, and they fit into many applications. The operating principle of brushless DC motor is based on electric commutation instead of mechanical commutation that exists in DC motor with brushes. In the sequel, we consider BLDC motors as the standard motors for the propulsion system design. However, the design method and motor's modeling remain valid for other types of DC motors.

Assuming negligible mechanical and electrical losses, the electric input power P_{in} to the BLDC motor and the output mechanical power P_{out} at the shaft can be written respectively as $P_{in} = V_{in}I_{in}$ and $P_{out} = \omega_m\tau_m$, where V_{in} and I_{in} are the supplied DC voltage and current from the battery pack respectively. τ_m is the torque developed at the shaft of the motor and ω_m is the rotational speed of the shaft. The relation between the input and out power is given by:

$$\frac{P_{out}}{P_{in}} = \frac{\tau_m}{I_{in}} \cdot \frac{\omega_m}{V_{in}} = k_i k_v, \quad (3.15)$$

where k_v and k_i are known respectively as the rotational speed-to-voltage constant and the torque-to-current constant (also known as the voltage and the torque constants). These two constants of electric motors are used to determine the electric power needed to load a certain propeller at a specified rotational speed. Mathematically, we write:

$$V_{in} = \frac{\omega_m}{k_v}, \quad I_{in} = \frac{P_{out}}{\omega_m k_i}. \quad (3.16)$$

Assuming a direct driving of the propeller, we can write:

$$V_{in} = \frac{\omega_p}{k_v}, \quad I_{in} = \frac{P_{fp}}{\omega_p k_i}. \quad (3.17)$$

where ω_p and P_{fp} are as defined in the previous section.

Eq. (3.17) indicates that to obtain a rotational speed ω_p , a voltage $V_{in} = \omega_p/k_v$ should be

supplied to the motor where k_v is given as a constant for the motor. Likewise, the current needed to produce a mechanical power P_{fp} necessary to rotate the propeller at speed ω_p depends on k_i . In practice, k_v is given by the technical specifications of the motor while k_i is rarely supplied in motor specifications. This is due to the fact that k_i is not constant at all operating points and rather it is a function of many factors such as the ratio between output power and the rating power of the motor and the temperature of the motor [60]. Instead, manufacturers supply operational curves and load charts of the motor that can be used to obtain the mapping between the supplied voltage to the motor and the expected drawn current under the load of different propellers. Figure 3.4 shows an example of the load curves for the BLDC motor (HC6332-230) manufactured by "Maxx product"⁵.

The HC6332-230 motor has an efficient current rating range of 30 – 80 A. The graph shows the drawn current vs. the supplied voltage for different propellers. For instance, the motor draws approximately 44 A when loaded with the propeller 15" × 10" and supplied by 40 V. Propellers that are not shown in the graph can be fitted in by approximate matching with the propellers presented in the graph. For instance, empirical experiments show that within a specific range of sizes, adding two inches to pitch equals to decreasing one inch in diameter; i.e., keeping the voltage level fixed, this motor draws approximately the same current under the load of 19" × 10" or 18" × 12" [61].

⁵This graph is taken from the data sheet of the motor as supplied by the manufacturer in [61].

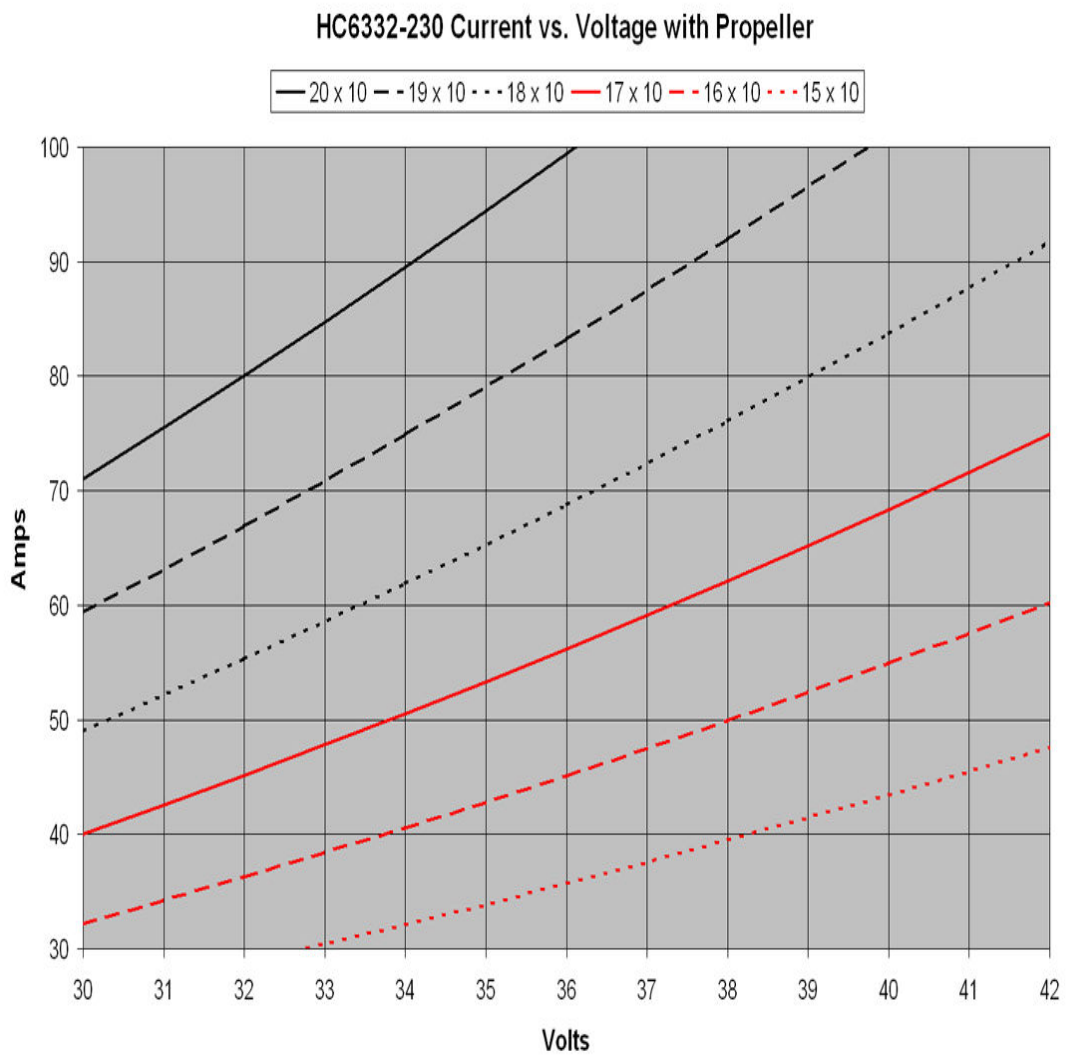


Figure 3.4: Load curves for the motor HC6332-230 (taken from [61]).

3.2.4 Electric Speed Controllers (ESCs)

ESCs are used to control the speed of electric motors and therefore the speed of the propellers to generate the required thrust. ESCs are electronic circuitries that receive reference signals from the user and accordingly regulate the voltage from the power supply to control the rotational speed of the controlled motors. The current and voltage rate of the ESC should match with the current rating and the operating voltage of the motor. In case of a BLDC motor, the ESC runs the appropriate electric switching sequence necessary to control the supply voltage and operate the motor. Moreover, a BLDC motor needs a designated ESC for brushless motors and cannot be controlled by other types of ESC. In the proposed design procedure, it is assumed that negligible power loss occurs at the ESC. In addition, the size and weight of the ESC are negligible compared to other principle components of the propulsion system. Therefore, the ESC is not an important component to be considered in the proposed design procedure.

3.2.5 Battery Packs

Battery packs are the power supply units that supply electric power to the motor to generate the required thrust. The voltage and current capacities of the battery should be sufficient to run the propeller at certain speed and generate the required thrust. In addition, the weight and size of the battery pack should fit the UAV design requirements. Different types and sizes of battery packs are used as energy storage units in UAV systems. The commonly used batteries for electric propulsion systems in UAVs are Lithium Polymer (Li-Po) batteries. Li-Po batteries have more power capacity and lighter in weight compared to other type of batteries, such as Ni-Cd and Ni-Mh [62]. Li-Po batteries are available in form of multiple cells with a no-load voltage of 3.7 V per cell and different current rating per cell. The total voltage supplied by a battery pack depends on the serial arrangement of its internal cells while the total current rating of the pack depends on the parallel arrangement and the nominal current rate of its internal cells. The weight of the battery pack is a function of its nominal current, nominal voltage and maximum discharging rate. The maximum discharging rate of a battery pack determines the maximum current that can be drawn from the pack (if the maximum discharging rate is high,

the maximum drawn current is high and vice versa). The operating time of the chosen battery pack, and hence the flight time of the vehicle, depends on the drawn current and the current rating of the battery pack. Mathematically, the battery pack is represented by:

$$V_b = V_{b_0} - I_b R_b, \quad I_{b_{max}} = c_{b_{max}} I_{b_0}, \quad t_b = \frac{I_{b_0} (A.h)}{I_b (A)}, \quad (3.18)$$

where V_b is the effective voltage at the terminal of the battery, V_{b_0} is the nominal no-load voltage rate, I_b is the drawn current from the battery and R_b is the internal resistance of the battery pack. The maximum current that can be drawn from the battery is $I_{b_{max}}$ while I_{b_0} is the current rate of the battery and is defined as the current that can be supplied from the battery for one hour before the rated voltage starts to drop, i.e. it is given in Amber-hour (A.h). $c_{b_{max}}$ is the maximum discharging rate of the battery and is defined by the battery manufacturer. t_b is the operating time of the battery before the voltage drops beyond the nominal value. The unit of t_b is (hours). This due to the fact that the current rate of the battery I_{b_0} is given in (A.h) and the required current for the propeller is given in (A).

3.3 Design Methodology

This section proposes a systematic procedure for designing the propulsion system of electrically driven VTOL rotary-wing UAV, assuming that the total size of the vehicle, including propellers' dimension, is specified. In addition, the maximum permissible weight of the vehicle including the propulsion system and the maximum payload is estimated a priori. The minimum continuous flight time needs to be specified as well.

The estimated size and structure of the UAV puts a radius restriction R_{max} on selecting the size range of propellers that can be used for the propulsion system design; i.e., $R_p \leq R_{max}$, where R_p is the radius of the selected propeller(s). For instance, if more than one propeller are positioned in the same plane, the radius size is restricted by a safety margin among blades so that they do not overlap. On the other hand, if only one propeller is used for the propulsion system, or a set of propellers but they are in different planes, the maximum allowed radius of the propellers increases. If the maximum size of propellers is not specified, an infinite size range of propellers can be employed in the design, however,

practical aspects of the design puts limits on the size of propellers that can be used in the design procedure.

The total weight of the UAV system includes the weight of the mechanical structure, on-board equipment, the propulsion system and payload. Given the estimated total weight of the vehicle M_{total} , the design objective of the propulsion system is always to achieve a taking-off thrust $f_h > M_{total}$ using the lightest possible components available in the market. The weight of the ESC and the propeller are negligible compared to the weight of the battery pack and electric motor which contributes the major part of the propulsion system's weight.

The propulsion system should enable the UAV to fly at least for a specified flight time t_{fmin} . The minimum flight time is important to decide on the required battery pack that in turn affects the weight of the propulsion system. Hence, a good propulsion system design calls for maximum thrust-to-weight ratio while achieving maximum possible flight time.

In total, the inputs to the design procedure are (i) the maximum allowable radius of the propeller: R_{max} , (ii) the total weight of the UAV: M_{total} , (iii) the allowance for the propulsion system weight: $M_{smax} = M_{total} - M_{pl}$ where M_{pl} is known and it is the weight of the vehicle structure⁶ and desired payload, and (iv) the required minimum flight time, t_{fmin} .

Design Procedure

Given the design specifications of M_{total} , M_{smax} and t_{fmin} , the following steps are proposed to design the electric propulsion system for VTOL UAVs:

1. Set the required thrust $f_h = \alpha M_{total}$, where $\alpha > 1$ is a safety factor to be chosen by the designer (e.g. $\alpha \approx 1.2$).
2. Selecting a set of propellers:

⁶The structure weight includes all components for control, signal processing and other on-board equipment.

- (a) Choose a set of commercially available propellers \mathbb{P} whose radius are $R_p \leq R_{max} \forall p \in \mathbb{P}$. The set \mathbb{P} may contain propellers of same radius but different pitches. If the pitch of the propeller is specified in terms of pitch length β_p , obtain its pitch angle θ_p using Eq. (3.14).
- (b) For each propeller $p \in \mathbb{P}$, calculate the minimum rotational speed ω_p (using Eq. (3.6) and Eq. (3.8)) and the corresponding minimum mechanical power P_{f_p} (using Eq. (3.11) or Eq. (3.12)) necessary to generate the required thrust f_h given in Step 1. A propeller $p \in \mathbb{P}$ is feasible to generate the required thrust if the condition $\omega_p \leq \omega_{p_{max}}$ is fulfilled, where $\omega_{p_{max}}$ is the maximum allowed rotational speed (specified by the manufacturer) of the propeller p . If not, the propeller cannot be used to generate the required thrust f_h and must be excluded from the design procedure.
- (c) Define the new set $\bar{\mathbb{P}} \subseteq \mathbb{P}$ that contains only the feasible propellers that can generate the given thrust; i.e., $\omega_p \leq \omega_{p_{max}} \forall p \in \bar{\mathbb{P}}$. Over all propellers $p \in \bar{\mathbb{P}}$, find the minimum rotational speed and minimum mechanical power necessary to generate the required thrust; i.e.,

$$\omega_{min} = \min_{p \in \bar{\mathbb{P}}}(\omega_p) \quad \text{and} \quad P_{min} = \min_{p \in \bar{\mathbb{P}}}(P_{f_p}).$$

3. Selecting a set of motors:

- (a) Select a set of commercially available BLDC motors \mathbb{M} such that $\forall m \in \mathbb{M}$ the following conditions are fulfilled:

$$P_{m_{max}} \geq P_{min} \quad , \quad \omega_{m_{max}} \geq \omega_{min} \quad \text{and} \quad M_m < M_{s_{max}}.$$

The above conditions imply that all chosen motors must have power rating $P_{m_{max}}$ greater than or equal to the least mechanical power P_{min} necessary to generate the required thrust by any feasible propeller and maximum rotational speed capability $\omega_{m_{max}}$ greater than or equal to the least necessary speed ω_{min} among all feasible propellers, where P_{min} and ω_{min} are obtained in Step 2c. In addition, the weight of any chosen motor $M_m \forall m \in \mathbb{M}$ should be less than the permissible weight of the propulsion system $M_{s_{max}}$.

- (b) Construct motor-propellers groups G_j , $j = 1, 2, \dots, n(\mathbb{M})$, where $n(\mathbb{M})$ denotes the number of the motors in the set \mathbb{M} . The j th group G_j contains a motor $m_j \in \mathbb{M}$ and a subset of propellers $\mathbb{I}_j \subseteq \overline{\mathbb{P}}$, where $\mathbb{I}_j := \{p \in \overline{\mathbb{P}} : \omega_p \leq \omega_{m_{j_{\max}}}, P_{f_p} \leq P_{m_{j_{\max}}}\}$. This means that the power rating $P_{m_{j_{\max}}}$ and the rotational speed capability $\omega_{m_{j_{\max}}}$ of the motor m_j must be greater than or equal to respectively the mechanical power P_{f_p} and rotational speed ω_p necessary to generate the required thrust $\forall p \in \mathbb{I}_j$.
- (c) For the j th group G_j , calculate V_p^j and $I_p^j \forall p \in \mathbb{I}_j$, where $V_p^j = \frac{\omega_p}{k_{v_{m_j}}}$ and I_p^j is obtained from the operational chart of the motor m_j (see for example Figure 3.4). V_p^j and I_p^j are respectively the required voltage and current for the motor m_j to rotate the propeller p at the minimum speed ω_p necessary to generate the required thrust f_h .
- (d) Select all feasible pairs in G_j , $j = 1, 2, \dots, n(\mathbb{M})$, where in a group G_j , the pair (m_j, p) , $p \in \mathbb{I}_j$, is feasible for the design if $I_p^j \leq I_{m_{j_{\max}}}$ given that $I_{m_{j_{\max}}}$ is the maximum allowed continuous current of the motor m_j (specified by the manufacturer).

4. Selecting a set of batteries:

- (a) For each feasible pair $(m_j, p) \in G_j$, select a set of commercially available battery packs \mathbb{B}_p^j such that $\forall b \in \mathbb{B}_p^j$ the following conditions are fulfilled:

$$V_b \geq V_p^j, \quad I_p^j \leq I_{b_{\max}} \quad \text{and} \quad M_b \leq M_{s_{\max}} - M_{m_j},$$

where V_b and $I_{b_{\max}}$ are respectively the effective voltage and maximum continuous discharging current of the battery $b \in \mathbb{B}_p^j$, and M_b is the weight of the corresponding battery pack.

- (b) $\forall b \in \mathbb{B}_p^j$, calculate the weight of the propulsion system (m_j, p, b) and the minimum (i.e., full load) flight time as:

$$M_{(m_j, p, b)} = M_{m_j} + M_b \quad \text{and} \quad t_{(m_j, p, b)} = \frac{I_{b_0}}{I_p^j},$$

where $(m_j, p) \in G_j$ is a feasible pair and I_{b_0} is the current rate of the battery $b \in \mathbb{B}_p^j$.

If $t_{(m_j,p,b)} < t_{f_{min}}$, the battery pack b cannot provide the required flight time when used with the pair (m_j, p) and must be excluded from \mathbb{B}_p^j .

(c) Calculate $M_{(m_j,p,b)}$ and $t_{(m_j,p,b)}$ for all feasible pairs $(m_j, p) \in G_j, j = 1, 2, \dots, n(\mathbb{M})$.

5. From all feasible combinations of motors, propellers and battery packs, we can choose two best designs:

(a) Based on maximum flight time: (m_t, p_t, b_t)

(b) Based on minimum propulsion system weight: (m_w, p_w, b_w)

These are two different selections, based on two different feasible combinations, where the first design gives the best possible (maximum) flight time and the second design gives the best possible (minimum) propulsion system weight. If the concern is for both flight time and weight, another selection that has a trade off between these two factors can be chosen.

Remark 2. The constraint on the motor weight specified in Step 3a is weak because it does not indicate any allowance for the weight of the battery pack. This might lead to unrealistic choices of heavy motors and subsequently the infeasibility of these heavy motors cannot be avoided when choosing the battery pack in the following steps. Therefore, in order to speed up the procedure and hence for efficient motor selection, the designer is advised to choose a reasonable weight limit for the motor that leaves reasonable allowance for the battery. In general, one can set the constraint for the motor weight as $M_m \leq \frac{1}{3}M_{s_{max}} \quad \forall m \in \mathbb{M}$. The scale $\frac{1}{3}$ is chosen due to the fact that battery packs are usually twice as heavy as the motors they are powering.

Remark 3. While checking the current constraint in Step 3c, the pair (m_j, p) is feasible but is not efficient if $I_p^j \ll I_{m_{max}}$, as the motor will not operate in the efficient region that is specified usually by a current region close to $I_{m_{max}}$. Therefore, the designer is advised to select only the efficient feasible pairs.

Remark 4. If a set of batteries having equal nominal currents I_{b_0} and different maximum discharging rate $c_{b_{max}}$ or different nominal voltages V_{b_0} , the designer must select those batteries (set \mathbb{B}_p^j in Step 4a) that have minimum but sufficient discharging rate $c_{b_{max}}$ and minimum but sufficient nominal voltage V_{b_0} such that achieving $I_{b_{max}} = c_{b_{max}}I_{b_0} \geq I_p^j$ and

$V_{b_0} - R_{b_0} I_p^j = V_p^j \quad \forall b \in \mathbb{B}_p^j$. This is due to the fact that the weight of the battery M_b is a function of $\{V_{b_0}, c_{b_{max}}, I_{b_0}\}$ while the designed flight time $t_{(m_j, p, b)}$ depends only on I_{b_0} and I_p^j . Therefore, when I_{b_0} is fixed, increasing $c_{b_{max}}$ or V_{b_0} beyond the required values will increase the weight of the battery pack and does not improve the flight time.

All contents of these three remarks are handled automatically in the design procedure but it is wise to keep these comments in mind in order to avoid generating large sets of components that are infeasible at subsequent steps.

3.4 Summary

Unmanned Aerial Vehicles (UAVs) of different shapes and sizes use electric propulsion systems to generate the required amount of thrust. An efficient design of the propulsion system enhances the performance, maximizes the endurance, increase payload capabilities and prolongs the flight time of the vehicle. In this chapter, a new procedure is introduced to enhance the design of electric propulsion systems for VTOL rotary-wing UAVs. The suggested algorithm chooses the components of the electric propulsion system- namely the propeller, electric motor and battery pack- in order to obtain the specified amount of thrust subject to minimizing the weight and power consumption of the propulsion system, and hence maximizing the flight time. To make the design procedure more practical, a simple models of thrust and mechanical power for air propellers are presented.

Chapter 4

A New Cost Effective Indoor Navigation Technique for UAV Systems

This chapter proposes a novel laser based navigation system that can be used as a cheap and easy-to-construct solution for indoor navigation problem. The system employs three laser beams along with a computer vision algorithm to obtain fully the position and orientation of the UAV. The proposed navigation system is introduced for indoor applications where the cost, size and weight of the vehicle is limited.

The chapter starts in Section 4.1 by emphasizing the need for new solution to indoor navigation problem and a summary of what has been done in this aspect. Section 4.2 presents a description of the proposed navigation system. The mathematical formulation of the proposed system and the derivation of UAV position and orientation are drawn in Section 4.3. The implementation procedure along with some technical issues related to the implementation process is discussed in Section 4.4. The chapter is concluded by some remarks and summary in Section 4.5.

4.1 Introduction and Related Work

A crucial step for the process of control and guidance of UAVs is the measurement of the 3D position and orientation of the vehicle. To achieve autonomy, UAVs need a navigation system that gives information regarding the status of the vehicle and feeds this information to the controller for an appropriate action to be taken. The common navigation system for orientation and position used in UAV applications is the Inertial Navigation System combined with Global Positioning System (INS/GPS) [63, 64, 65]. The INS integrates the vehicle's acceleration over time to estimate the velocity and position of the UAV. The GPS data is then used to correct the integration error accumulated over time [64]. Hence, seeking accurate estimation with less noise and errors requires good GPS signal reception. In practice, the GPS signal might not be available or it is in bad quality at clutter environments or urban areas [65]. Moreover, the weight, size and cost limitations of small UAVs impose further constraints to the use of the conventional INS/GPS system. Therefore, the need rises for alternative navigation methods for small UAVs and indoor applications.

In literature, different alternative navigation techniques have been investigated recently such as pressure sensors for altitude, magneto-resistive magnetometer, laser range finder, radar and ultra sound for position estimation and obstacles detection [65, 66]. In this regard, vision-based systems have attained growing interest to be used for indoor and outdoor navigation [63, 64, 65, 67] due to the fact that vision based systems are lightweight, passive and produce rich information about the motion of the vehicle [65]. Computer vision navigation algorithms were used initially for ground mobile robots and then imported to the field of UAV systems [68, 69] where several techniques are developed to estimate the motion of air vehicle, e.g., ego-motion, object tracking, optical flow and scene recognition [65].

Ideally, in vision based navigation systems, the path of the UAV needs to be known a priori. Images of the environment of the UAV flying path are captured, analyzed and stored in the system memory a priori to identify the basic features of the flying path. The navigation task is then implemented by comparing the real time images, taken from a single or multi on-board cameras, with the visual memory of the vehicle to identify

the recognized features and estimate the motion of the UAV. Different algorithms and schemes are developed to excel the feature detection process and speed up the comparison algorithms [70, 71, 72]. Among the developed computer vision algorithms, the Scale Invariant Feature Transform (SIFT) algorithm developed in [73] and its modified versions are used in many vision navigation systems and show good results in terms of processing time and accuracy [72, 74, 75, 76]. The SIFT algorithm determines the features of images that are invariant to rotation, scaling, viewpoint and partially illumination.

Computer vision based algorithms might be used solely to estimate the motion and orientation of the vehicle by tracking features in two consecutive images of the surrounding environment of the UAV [68]. However, this method is complicated, involves heavy computational burden, affected highly by the quality of the image and the number of features to be analyzed [77]. This type of algorithms works efficiently only in specific territories with good images. To reduce the complexity and computational costs, the image analysis is chosen in [78, 79] to be on a ground station where the data is communicated to the UAV via a wireless link. This type of implementation reduces the autonomy of the UAV and puts the vehicle at risk in case of wireless communication failure. In [80, 81], the vision-based information is integrated with data from other sensors such as GPS/gyroscope to refine the data and correct the UAV motion. This implementation again requires a good GPS signal which is infeasible for indoor applications and urban territories. In [64] and [82], the path of the UAV is identified by using the Digital Elevation Map (DEM) of the area of flight. The estimation problem of position and orientation is formulated as a tracking problem and solved using Extended Kalman Filter. Information from the vision system is connected with DEM data to estimate the position of the UAV. However, the use of DEM data requires the flight of the UAV to be in high attitude and long enough to cover many sites. In addition, DEM is not available for all areas and therefore it is infeasible for indoor applications. The scene reconstruction technique is used in [83] to build a 3D terrain map of the flying path. The position of the UAV is estimated by matching the reconstructed image with a pre-stored path map. This approach is a very difficult inverse-problem and involves practical difficulties. The authors in [84] proposes a laser based navigation system that is similar to the one proposed in this chapter where the projection of four diode spots on the ground are used to estimate the position of a helicopter. However, in the proposed technique of this reference, the estimation of the motion of the

helicopter is made by the maximum likelihood method, where the used algorithm contains an overdetermined nonlinear equations, and the authors did not discuss how to solve these equations. The focus of the authors was on the control system of the helicopter and the navigation system performance was not tackled enough. To sum up, vision based navigation systems are still developing, have many software and hardware issues and far from optimal [85]. This keeps the door open for further research and exploring to the indoor navigation problem.

In this chapter, we employ a computer vision algorithm only to identify the positions of three laser dots generated by three laser beams that are fixed to the body of the vehicle. The positions of the laser dots are used to obtain the orientation and 3D position of the UAV. The image processing requirement for the proposed system can be done on-board or on aground station. Furthermore, the quality of the image has less impact on the system reliability as the aim of the image is only to recognize the laser dots and identify their coordinates. The proposed system uses the location of three laser dots to navigate the UAV without further requirement for fusing data estimation method like Extended Kalman Filter or additional GPS/IMU sensors. The proposed system is developed for indoor UAVs, however, it can be used for outdoors missions in areas where the UAV flies in low attitude over planar surfaces such as sport fields.

4.2 System Description

Figure 4.1 shows a schematic diagram of the proposed navigation system. The proposed system composes of three laser beams that are fixed at the center of mass CG of the vehicle and they shoot downwards on the ground. The laser beams from the center of mass of the vehicle to the ground is forming three vectors \bar{l}_1 , \bar{l}_2 and \bar{l}_3 . The angles between any two laser vectors is α and the length of the laser vectors are respectively l_1 , l_2 and l_3 . The angle α is identical between any two laser vectors and is fixed in the open set $(0, \frac{2\pi}{3})$. If $\alpha \geq \frac{2\pi}{3}$, the laser beams are either in the same plane of the UAV or shooting upwards opposite to the ground, which is infeasible and not to be considered. The global earth frame system is represented by the right hand Cartesian system $X_e Y_e Z_e$ where the plane $X_e Y_e$ represents the ground of the flying path. The UAV fixed body coordinate system is

denoted by the axes $X_b Y_b Z_b$. In the sequel, we use a superscript letter (e for earth frame or b for body frame) to denote the coordinate system in which the vector is represented.

The three laser beams form three laser spots on the ground d_1 , d_2 and d_3 . a_1 , a_2 and a_3 are the lengths between the laser dots respectively as shown in Figure 4.1. The three laser dots on the ground have certain coordinates in the global earth frame; i.e., $(x_1^e, y_1^e, 0)$, $(x_2^e, y_2^e, 0)$ and $(x_3^e, y_3^e, 0)$ respectively. To obtain the coordinates of the laser spots, different techniques can be used to capture the laser dots on the ground first and then analyze the picture to obtain the coordinates of the dots. By knowing the coordinates of these three laser spots, the proposed system aims to determine the position of the UAV in the global earth frame in form of the Cartesian coordinates (x_v^e, y_v^e, z_v^e) and the attitude of the vehicle in the form of roll, pitch and yaw angles $(\phi_v, \theta_v, \psi_v)$.

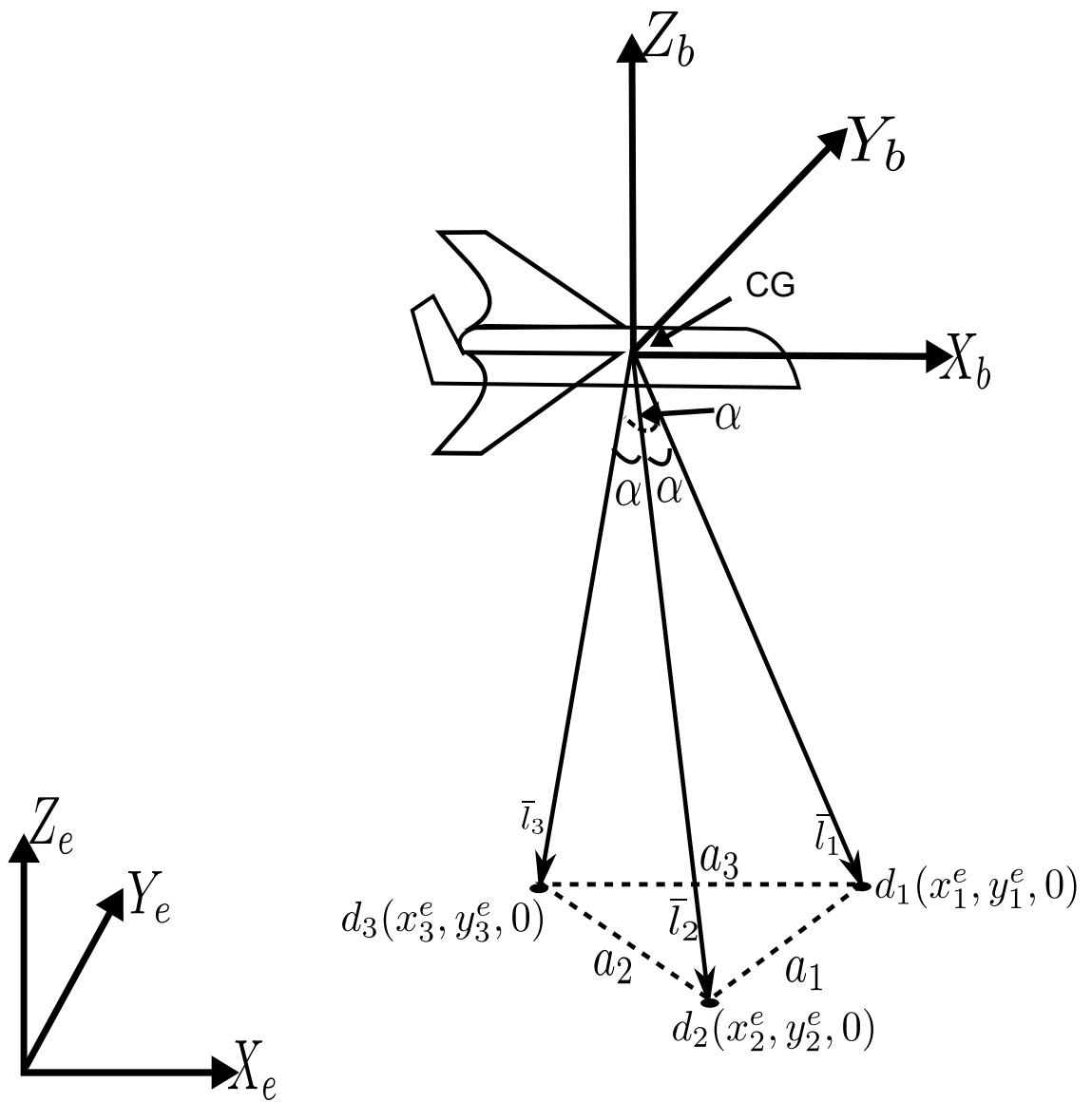


Figure 4.1: The schematic diagram for structure and notations of the proposed navigation system.

4.3 Theoretical Formulation

In this section, all measurements and values are considered to be in earth frame e unless specified, and for simplicity of representation the superscript e is not written. For the proposed navigation system, we consider the navigation problem of obtaining the spacial position (x_v, y_v, z_v) and orientation $(\phi_v, \theta_v, \psi_v)$ of the center of mass of the vehicle from the data of the laser dots coordinates $(x_1, y_1, 0)$, $(x_2, y_2, 0)$, $(x_3, y_3, 0)$.

4.3.1 UAV Position

In the Cartesian space, see Figure 4.1, we have:

$$l_1^2 = (x_v - x_1)^2 + (y_v - y_1)^2 + z_v^2, \quad (4.1)$$

$$l_2^2 = (x_v - x_2)^2 + (y_v - y_2)^2 + z_v^2, \quad (4.2)$$

$$l_3^2 = (x_v - x_3)^2 + (y_v - y_3)^2 + z_v^2. \quad (4.3)$$

Solving this set of equations for x_v , y_v and rewriting in matrix form gives:

$$\begin{bmatrix} x_v \\ y_v \end{bmatrix} = \frac{1}{2} \begin{bmatrix} -x_1 + x_2 & -y_1 + y_2 \\ -x_2 + x_3 & -y_2 + y_3 \end{bmatrix}^{-1} \begin{bmatrix} l_1^2 - l_2^2 + x_2^2 + y_2^2 - x_1^2 - y_1^2 \\ l_2^2 - l_3^2 + x_3^2 + y_3^2 - x_2^2 - y_2^2 \end{bmatrix}. \quad (4.4)$$

Subsequently z_v is a function of x_v and y_v and can be given from Eq. (4.1) as:

$$z_v = \sqrt{l_1^2 - (x_v - x_1)^2 - (y_v - y_1)^2}. \quad (4.5)$$

Alternatively, z_v can be obtained from (4.2) and (4.3) as a function of the position of laser dot d_2 and the laser beam length l_2 or as a function of the position of laser dot d_3 and the laser beam length l_3 . Obtaining the lengths of the laser beams l_1 , l_2 and l_3 can be calculated from the coordinates of the laser dots by using the cosine rule for the side

triangles of the pyramid formed by the laser beams as:

$$a_1^2 = l_1^2 + l_2^2 - 2l_1l_2 \cos \alpha, \quad (4.6)$$

$$a_2^2 = l_2^2 + l_3^2 - 2l_2l_3 \cos \alpha, \quad (4.7)$$

$$a_3^2 = l_1^2 + l_3^2 - 2l_1l_3 \cos \alpha, \quad (4.8)$$

where a_1 , a_2 and a_3 are the length of triangle sides that is formed by the laser dots on the ground as shown in Figure 4.1. In the Cartesian space, these three lengths can be obtained by:

$$a_1 = ((x_1 - x_2)^2 + (y_1 - y_2)^2)^{\frac{1}{2}}, \quad (4.9)$$

$$a_2 = ((x_2 - x_3)^2 + (y_2 - y_3)^2)^{\frac{1}{2}}, \quad (4.10)$$

$$a_3 = ((x_1 - x_3)^2 + (y_1 - y_3)^2)^{\frac{1}{2}}. \quad (4.11)$$

Therefore, the laser beam lengths can be calculated by solving the nonlinear equations (4.6) - (4.8) for the unknowns l_1 , l_2 and l_3 . The lengths of the laser beams will be discussed in details in Section 4.4.

Note that, Eq. (4.4) is solvable and hence x_v and y_v can be obtained always when l_i , x_i and y_i are known, $i = 1, 2, 3$. The singularity of the inverted matrix in (4.4) occurs only when:

$$\begin{aligned} (x_2 - x_1)(y_3 - y_2) &= (x_3 - x_2)(y_2 - y_1) \\ \Rightarrow \frac{(y_3 - y_2)}{(x_3 - x_2)} &= \frac{(y_2 - y_1)}{(x_2 - x_1)} \\ \Rightarrow \bar{a}_1 &\parallel \bar{a}_2 \end{aligned}$$

where \bar{a}_1 , \bar{a}_2 are the vectors between the laser dots d_1 , d_2 and d_3 respectively. This case is not possible practically because \bar{a}_1 and \bar{a}_2 are two sides in the triangle $d_1d_2d_3$. Therefore, Eq. (4.4) is practically always solvable.

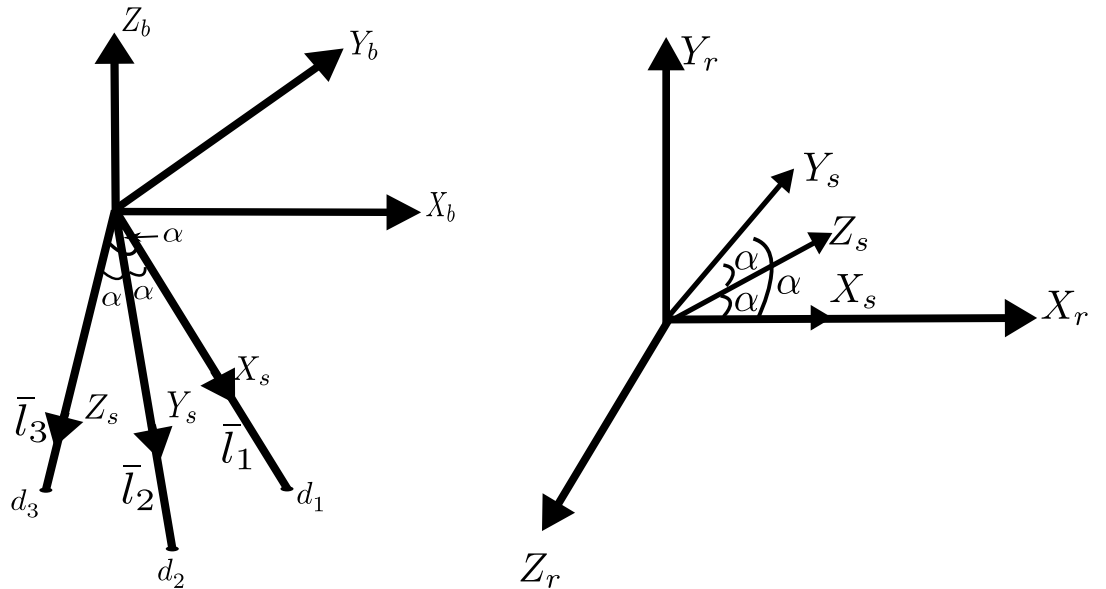
4.3.2 UAV Orientation

To obtain the orientation of the vehicle, in addition to the earth coordinate system and the body coordinate system defined before in Section 4.2, we consider the following coordinate systems:

s: a coordinate system whose axes $X_s Y_s Z_s$ coincide with the laser beam vectors \bar{l}_1, \bar{l}_2 and \bar{l}_3 respectively. Therefore, the angle between any two axes X_s, Y_s, Z_s is α and the system in general is not orthogonal.

r: an auxiliary orthogonal coordinate system that is used to obtain the orientation of the UAV.

Without loss of generality, we can choose X_r to be aligned with X_s while Y_r is in the plane $X_s Y_s$. Figure 4.2 shows the coordinates systems used to get the orientation of the UAV.



(a) The body coordinate system and the laser beams coordinate system.

(b) Transforming the laser beams to an orthogonal coordinate system.

Figure 4.2: The coordinate systems used to develop the proposed navigation algorithm.

The orientation of the vehicle can be determined by finding the rotation matrix between the body coordinate system and the fixed earth coordinate system. Assuming that the center of mass of the UAV coincides with the origin of the laser beams, we can write:

$$\bar{l}_i^e = R_b^e R_r^b T_s^r \bar{l}_i^s, \quad i = 1, 2, 3 \quad (4.12)$$

where

\bar{l}_i^s : the laser beam vector in the laser coordinate system.

T_s^r : the transformation matrix from the laser coordinate system s to the orthogonal laser coordinate system r .

R_r^b : the rotation matrix from the orthogonal coordinate system of the laser beams r to the body frame b .

R_b^e : the rotation matrix from the body frame b to the earth frame e .

\bar{l}_i^e : the laser beam vector in the general earth frame e .

In the Cartesian space, we can write:

$$\bar{l}_1^e = \begin{bmatrix} x_1 - x_v \\ y_1 - y_v \\ -z_v \end{bmatrix}, \quad \bar{l}_2^e = \begin{bmatrix} x_2 - x_v \\ y_2 - y_v \\ -z_v \end{bmatrix}, \quad \bar{l}_3^e = \begin{bmatrix} x_3 - x_v \\ y_3 - y_v \\ -z_v \end{bmatrix} \quad (4.13)$$

and

$$\bar{l}_1^s = \begin{bmatrix} l_1 \\ 0 \\ 0 \end{bmatrix}, \quad \bar{l}_2^s = \begin{bmatrix} 0 \\ l_2 \\ 0 \end{bmatrix}, \quad \bar{l}_3^s = \begin{bmatrix} 0 \\ 0 \\ l_3 \end{bmatrix} \quad (4.14)$$

From Eq. (4.12) and in matrix form we write:

$$U^e = R_b^e R_r^b T_s^r U^s \quad (4.15)$$

and equivalently this leads to:

$$R_b^e = U^e \left(R_r^b T_s^r U^s \right)^{-1} \quad (4.16)$$

$$= U^e (U^s)^{-1} (T_s^r)^{-1} \left(R_r^b \right)^{-1} \quad (4.17)$$

where $U^e = \begin{bmatrix} \bar{l}_1^e & \bar{l}_2^e & \bar{l}_3^e \end{bmatrix}$ is a matrix of the laser beam coordinates in the earth frame and $U^s = \begin{bmatrix} \bar{l}_1^s & \bar{l}_2^s & \bar{l}_3^s \end{bmatrix}$ is a matrix of the laser beam coordinates in the laser frame. Practically speaking, U and U^s exist always and they are nonsingular.

Given a vector $[x_s \ y_s \ z_s]^T$ in the laser beams coordinate s , the coordinates of the same vector in the coordinate system r can be given by:

$$\begin{bmatrix} x_r \\ y_r \\ z_r \end{bmatrix} = \begin{bmatrix} t_{11} & t_{12} & t_{13} \\ t_{21} & t_{22} & t_{23} \\ t_{31} & t_{32} & t_{33} \end{bmatrix} \begin{bmatrix} x_s \\ y_s \\ z_s \end{bmatrix} \quad (4.18)$$

where t_{ij} , $i, j = 1, 2, 3$ represent the elements of transformation matrix T_s^r from frame s to frame r . In geometry, t_{ij} represent the coordinates of the unit vectors of the frame s in the frame r . Assuming both coordinate systems s and r have the same scale grids and with coordinate choice as in Figure 4.2(b), then it can be concluded easily that:

$$T_s^r = \begin{bmatrix} 1 & \cos \alpha & \cos \alpha \\ 0 & \sin \alpha & t_{23} \\ 0 & 0 & t_{33} \end{bmatrix} \quad (4.19)$$

The inner products of the unit vectors of Y_s and Z_s gives:

$$(t_{12}t_{13}) + (t_{22}t_{23}) + (t_{32}t_{33}) = |1||1| \cos \alpha$$

$$\Rightarrow t_{23} = \frac{\cos \alpha (1 - \cos \alpha)}{\sin \alpha}$$

The cosine directions of any vector in an orthogonal coordinate system is equal to 1. In our case, this means:

$$t_{13}^2 + t_{23}^2 + t_{33}^2 = 1$$

$$\Rightarrow t_{33} = \frac{\sqrt{1 - 3\cos^2 \alpha + 2\cos^3 \alpha}}{\sin \alpha}.$$

and this makes the matrix T_s^r as:

$$T_s^r = \begin{bmatrix} 1 & \cos \alpha & \cos \alpha \\ 0 & \sin \alpha & \frac{\cos \alpha(1-\cos \alpha)}{\sin \alpha} \\ 0 & 0 & \frac{\sqrt{1-3\cos^2 \alpha+2\cos^3 \alpha}}{\sin \alpha} \end{bmatrix}, \quad \alpha \in \left(0, \frac{2\pi}{3}\right). \quad (4.20)$$

Eq. (4.20) shows clearly that T_s^r is only a function of the angle α and not related to the status of the vehicle. In the specified range, T_s^r is not singular and invertible.

R_r^b represents the rotation matrix from the orthogonal system r to the body frame b . This rotation matrix is related only to the physical angles between the laser beams and the body of the UAV and therefore it is constant. To obtain R_r^b , we assume there is no rotation between the global earth system and the zero-time body frame, i.e., the vehicle is above the ground in a horizontal alignment with the ground with no yaw rotation before any change in the attitude of the vehicle. At this point of time, R_b^e is a unity matrix, i.e., $R_{b_0}^e = I_{3 \times 3}$. Now, from Eq. (4.15) we can write:

$$R_r^{b_0} = U_0^e (U_0^s)^{-1} (T_s^r)^{-1} \quad (4.21)$$

where U_0^e and U_0^s represent the coordinates matrices of the laser beam vectors in earth frame and laser frame respectively before the vehicle makes any attitude change and its above the ground in a complete horizontal alignment with the ground, i.e.,

$$U_0^e = \begin{bmatrix} x_{1_0} - x_{v_0} & x_{2_0} - x_{v_0} & x_{3_0} - x_{v_0} \\ y_{1_0} - y_{v_0} & y_{2_0} - y_{v_0} & y_{3_0} - y_{v_0} \\ -z_{v_0} & -z_{v_0} & -z_{v_0} \end{bmatrix} \quad (4.22)$$

$$U_0^s = \begin{bmatrix} l_{1_0} & 0 & 0 \\ 0 & l_{2_0} & 0 \\ 0 & 0 & l_{3_0} \end{bmatrix} \quad (4.23)$$

Eq. (4.21) indicates that the rotation matrix $R_r^{b_0}$ is time independent and therefore it is

always true that $R_r^b = R_r^{b_0}$. Now, substituting Eq. (4.21) in Eq. (4.17) gives:

$$R_b^e = U^e(U^s)^{-1} (T_s^r)^{-1} (R_r^b)^{-1} \quad (4.24)$$

$$= U^e(U^s)^{-1} (T_s^r)^{-1} (U_0^e(U_0^s)^{-1} (T_s^r)^{-1})^{-1} \quad (4.25)$$

$$= U^e(U^s)^{-1} (T_s^r)^{-1} T_s^r U_0^s (U_0^e)^{-1} \quad (4.26)$$

$$= U^e(U^s)^{-1} U_0^s (U_0^e)^{-1} \quad (4.27)$$

The standard orientation angles are defined as the rotation angles from e to b and this means that the required rotation matrix is R_e^b . From Eq. (4.27), we have:

$$R_e^b = (R_b^e)^{-1} = U_0^e(U_0^s)^{-1} U^s (U^e)^{-1} \quad (4.28)$$

The general form of the rotation matrix from the earth frame e to the body frame b using the standard rotation angles Roll ϕ_v , Pitch θ_v and Yaw ψ_v is given in [86] as:

$$R_e^b = \begin{bmatrix} C_{\theta_v} C_{\psi_v} & C_{\theta_v} S_{\psi_v} & -S_{\theta_v} \\ -C_{\phi_v} S_{\psi_v} + S_{\phi_v} S_{\theta_v} C_{\psi_v} & C_{\phi_v} C_{\psi_v} + S_{\phi_v} S_{\theta_v} S_{\psi_v} & S_{\phi_v} C_{\theta_v} \\ S_{\phi_v} S_{\psi_v} + C_{\phi_v} S_{\theta_v} C_{\psi_v} & -S_{\phi_v} C_{\psi_v} + C_{\phi_v} S_{\theta_v} S_{\psi_v} & C_{\phi_v} C_{\theta_v} \end{bmatrix} \quad (4.29)$$

where $C. = \cos(\cdot)$, $S. = \sin(\cdot)$ and the sequence of the rotation is ψ_v , θ_v and then ϕ_v . Matching the rotation matrix R_e^b in Eq. (4.28) with the general form of the rotation matrix in Eq (4.29) gives the required attitude angles ϕ_v , θ_v and ψ_v given that $-\frac{\pi}{2} < \theta_v < \frac{\pi}{2}$.

4.4 Implementation

The previous section shows that the position and orientation of the UAV can be obtained by knowing the global position of the laser dots. This section discusses how to get the required information of the laser dots coordinates and the dependent values of the laser beams lengths. It starts by focusing on the length of the laser beams in Section 4.4.1 and then presents the possible techniques to capture the laser dots coordinates in Section 4.4.2.

A fundamental assumption for the implementation process is that the laser beams hits the ground and that the ground is flat. This assumption is necessary in order to capture the coordinates of the laser dots correctly in the earth coordinate frame.

4.4.1 Obtaining the lengths of the Laser Beams

In order to get the position and orientation of the UAV using Equations (4.4) and (4.28), the lengths of the laser beams l_1 , l_2 and l_3 should be known. It has been shown in Section 4.3 that to get the length of the laser beams, we need to solve a set of nonlinear equations (4.6) - (4.8).

Solving the nonlinear equations to obtain the laser beam lengths has computational cost as it needs a search algorithm. To enhance the nonlinear algorithm, the starting point of the search algorithm can be given using data from three laser range finders. The laser range finders are used to generate the laser beams and supply the measured length of the beams. The laser range finder should not be used independently to obtain the leaser beam lengths. This is due to the fact that any inaccuracy of measurement or uncertainty of laser range sensors will result in wrong calculation of the UAV position and orientation.

In order to avoid the nonlinearity, the angle between the laser beam can be set to $\alpha = 90^\circ$. In this case, the set of nonlinear equations (4.6) - (4.8) is simplified to:

$$a_1^2 = l_1^2 + l_2^2, \quad (4.30)$$

$$a_2^2 = l_2^2 + l_3^2, \quad (4.31)$$

$$a_3^2 = l_1^2 + l_3^2, \quad (4.32)$$

and a closed form solution is obtained as:

$$l_1 = \left(\frac{a_1^2 - a_2^2 + a_3^2}{2} \right)^{\frac{1}{2}}, \quad (4.33)$$

$$l_2 = \left(\frac{a_1^2 + a_2^2 - a_3^2}{2} \right)^{\frac{1}{2}}, \quad (4.34)$$

$$l_3 = \left(\frac{-a_1^2 + a_2^2 + a_3^2}{2} \right)^{\frac{1}{2}}. \quad (4.35)$$

Therefore, the configuration of $\alpha = 90^\circ$ is advantageous for getting the laser beam lengths where there is no need for any search algorithm to solve the nonlinear equation. This in turn means less computational time and more accuracy. However, as it will be seen in next section, setting the angle between the laser beams $\alpha = 90^\circ$ implies special requirement for the used camera to capture the positions of the laser dots on the ground in case of using on board camera to capture the dots. The requirement of the camera is related to its focal length and sensor dimension, see Remark 5.

4.4.2 Capturing The Laser Dots Coordinates

In order to identify the global coordinates of the laser dots, the system needs to capture the dots on the ground first and then process the image to get the position of the laser dots. Different techniques can be used to capture the dots on the ground, for instance, a fixed camera at the flying area can be used to capture the laser dots in the flying path. This option can be used in small zones where the whole flying area can be captured by one camera. For wide spaces, more than one camera should be used to cover the flying path. The image(s) from the camera(s) are then analyzed by a computer vision algorithm to identify the laser dots and obtain their coordinates. In general, the fixed camera technique is simple but it needs a communication channel between the UAV and the ground station to communicate the data of the laser coordinates, which in return reduces the level of autonomy of the UAV.

Another alternative method for capturing the laser dots and identify their coordinates is to

use on-board camera and do the required analysis on-board. This choice increases the autonomy of the vehicle and makes the system flexible to be used in different environments. In this case, fixed landmarks in the flying path should be used to obtain the global coordinates of the laser dots. The global positions of the landmarks should be known a priori so that they can be used as database to obtain the global position of the laser dots. In details, the process starts by capturing the three laser dots and landmarks that are appearing in the view to the on-board camera. Then, a computer vision algorithm, e.g., SIFT, is used to analyze the captured photo and identify its components. When a landmark is recognised in the photo, a mapping matrix between the local position of the landmark in the image reference system and its predefined global position in the earth frame is calculated. In the image coordinate frame, it is possible to get the positions of the laser dots in relative to the recognized landmarks. Thereafter, the mapping data of the landmark positions in both reference systems is used to rotate the laser dots into the global earth frame and get their global coordinates. However, in order for the laser dots to be seen by the camera at all times, a restriction to the angle α between the laser beams should be considered. The angle constraint is related to the specifications of the used camera and will be discussed in next section.

4.4.3 On-board camera: restrictions to the angle α between the laser beams

In case of using on-board camera to capture the laser dots, the angle α between the laser beams should be chosen so that the camera can capture all the three laser dots on the ground at all times. In other words, the laser dots have to be inside the Field of View (FoV) of the camera at all times. The minimum FoV occurs in case of horizontal alignment between the camera and the captured body. For a rectilinear image camera, the FoV of a camera with lens of focal length l_f and optical sensor dimension d_s is represented in

Figure 4.3 and given by:

$$\tan \delta = \frac{d_s/2}{l_f} = \frac{d_e/2}{z_l} \quad (4.36)$$

$$\Rightarrow d_e = \frac{d_s z_l}{l_f} \quad (4.37)$$

where z_l is the height of the lens above the laser dots on the ground and 2δ is angle of FoV.

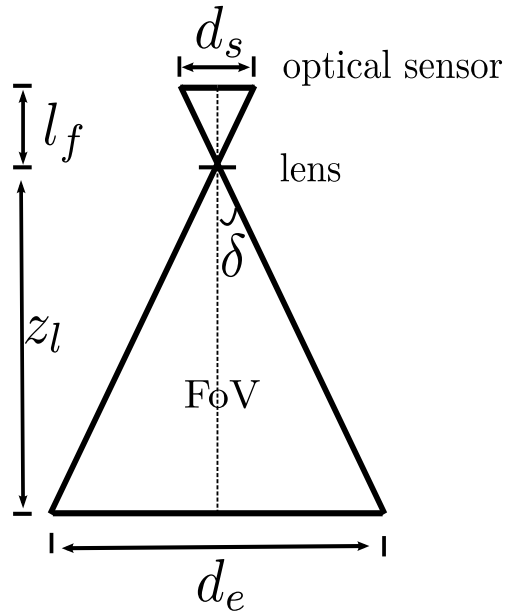


Figure 4.3: The FoV of on-board camera.

For the proposed system, it is assumed that the lens of the camera is fixed at the center of the UAV and hence $z_l = z_v$.

The three laser dots form a triangle of sides lengths a_1 , a_2 and a_3 , as shown in Figure 4.1. This triangle must fit inside the FoV at all times. In other words, the circumcircle of radius r_c that passes through the vertices of the triangle $a_1 a_2 a_3$ should be inside the FoV. Mathematically, we write:

$$r_c \leq \frac{d_e}{2}. \quad (4.38)$$

The relation between the radius of the circumcircle r_c and the lengths of the triangle sides a_1, a_2, a_3 is given in [87] as:

$$r_c = \frac{a_1 a_2 a_3}{\sqrt{(a_1 + a_2 + a_3)(-a_1 + a_2 + a_3)(a_1 - a_2 + a_3)(a_1 + a_2 - a_3)}}. \quad (4.39)$$

Without loss of generality, the laser system can be constructed in such a way to give $a_1 = a_2 = a_3 = a$ and $l_1 = l_2 = l_3 = l$ when the UAV is in horizontal alignment with the ground. In this case, we can write:

$$r_c = \frac{a}{\sqrt{3}}, \quad (4.40)$$

Using Equations (4.37) - (4.40), the distance between the laser dots on the ground is given by:

$$a = \sqrt{3} r_c \quad (4.41)$$

$$\leq \sqrt{3} \frac{d_e}{2} \quad (4.42)$$

$$\leq \frac{\sqrt{3} d_s z_v}{2 l_f}. \quad (4.43)$$

In the horizontal alignment and following the construction assumption of $a_1 = a_2 = a_3 = a$ and $l_1 = l_2 = l_3 = l$, the relation between z_v and the triangle $d_1 d_2 d_3$ can be defined from Figure 4.1 as:

$$l^2 = z_v^2 + \frac{a^2}{3}. \quad (4.44)$$

From Eq. (4.6) we have:

$$a^2 = 2l^2 - 2l^2 \cos \alpha \quad (4.45)$$

Using Eq. (4.45) in (4.43) leads to:

$$\cos \alpha \geq \frac{2 - \frac{d_s^2}{4l_f^2}}{2 + \frac{d_s^2}{2l_f^2}}.$$

Therefore, using a camera of focal length l_f and sensor dimension d_s implies that the

designed angle between the laser beams has the constraint:

$$\cos \alpha \geq \frac{2 - \frac{d_s^2}{4l_f^2}}{2 + \frac{d_s^2}{2l_f^2}}. \quad (4.46)$$

Remark 5. : If the design implies a certain angle α and then the camera is to be chosen accordingly, by following similar analysis we can write:

$$\frac{d_s}{l_f} \geq 2\sqrt{2} \left(\frac{1 - \cos \alpha}{1 + 2 \cos \alpha} \right)^{0.5}, \quad (4.47)$$

and for the special case of $\alpha = 90^\circ$, the chosen camera should satisfy $d_s \geq 2\sqrt{2}l_f$.

4.4.4 The Implementation Algorithm

This section summarizes the implementation steps of the proposed laser-based navigation system. We consider the case of on-board camera as it is more efficient compared to the fixed camera technique. In this case, the implementation process has two parts, off-line pre-processing and on-line navigation processing. We assume that the UAV flies above a flat surface and the laser dots are on the ground. In addition, the UAV takes off from a stand where the initial height of the UAV z_{v_0} is not zero and the vehicle is in horizontal alignment with the ground. These assumptions are to ensure the availability of the matrices U_0^e and U_0^s in Eq. (4.28) and the correct measurement of the global coordinates of the laser dots.

- Off-line process:
 1. Identify the landmarks on the ground and determine the global position of each landmark.
 2. At time ($t = 0$), obtain the length of the laser beams l_{1_0} , l_{2_0} , l_{3_0} and then the position of the vehicle x_{v_0} , y_{v_0} , z_{v_0} accordingly.
 3. Obtain the matrices U_0^e and U_0^s using Equations (4.22) - (4.23).

- On-line process:
 1. Obtain the frame from the video stream of the on-board camera and run the preferred computer vision algorithm to recognize at least one landmark and the three laser dots.
 2. Determine the locations of the three laser dots in relative to the position of the most successfully recognized landmark.
 3. Obtain the global positions of the three laser dots $x_i, y_i, i = 1, 2, 3$.
 4. Obtain the lengths of the laser beams $l_i, i = 1, 2, 3$.
 5. Find the position and altitude of the UAV using Equations (4.4) and (4.5).
 6. Find the orientation angles of the UAV using Eq. (4.28) .

Remark 6. In order to minimize the number of landmarks needed to be recognized to identify the coordinates of the laser dots, the landmarks should be chosen not to be symmetric objects and therefore any rotation around the landmark can be recognized. In case of symmetric landmarks, at least two landmarks are needed to be recognized to identify the coordinates of the laser dots.

Remark 7. In order to reduce the computation time of the computer vision algorithm, when a landmark is recognized, the search in next video frames always starts from the identified landmark. If the previous seen landmark is not found, the search considers the closest landmark before moving to the further ones. Given landmarks are not symmetric in shapes around any axis, identifying one landmark is enough to determine the coordinates of the laser dots on the ground.

4.5 Summary

This chapter proposes a new, cost-effective and simple navigation system for UAVs. The system is proposed for indoor applications, yet, it can be used also in outdoor missions if the UAV flies at low altitude above plain and predetermined areas. This makes the system ideal for testing stages of mini UAV systems where the possibility of crash is high and it is preferable not to use expensive navigation system during these flight tests. The

system provides full information about the position and orientation of the UAV using three laser beams fixed to the vehicle's body system and pointing downward to the ground. A computer vision algorithm is needed to identify the dots and determine their positions. The system is more efficient when the angle between the laser beams is $\alpha = 90^\circ$ as it becomes possible to get the length of the laser beams without the need for extra sensors or estimation algorithms. In this case, when using on-board camera, the specifications of the camera should satisfy certain condition related to α so that the camera can capture the laser dots on the ground always.

Chapter 5

Case Study: Design and Control of Novel Tri-Rotor UAV

This chapter is dedicated to the design and control of a novel tri-rotor UAV. The proposed vehicle is novel in structure and operation in which a tri-rotor arrangement associated with tilt-rotor mechanism is utilized to achieve six degree of freedom with full authority of force and torque vectoring. A centralized rotational and translational motion control system for the proposed platform is also developed using feedback linearisation associated with \mathcal{H}_∞ loop shape design. Throughout the control design of the system, a simulation based analysis is presented to show the effect of unmodeled actuator dynamics on the stability of the vehicle. In addition, a comparison study is conducted between the two stage feedback linearisation proposed previously in this thesis and the classical feedback linearisation of the whole UAV system to handle actuator dynamics.

The motivation behind the contributed design is pointed out in Section 5.1 and then it is followed by a functional description of the proposed vehicle in Section 5.2. A mathematical model that captures the dynamics of the UAV and govern the behaviour of the system is derived in Section 5.3. The control design of the proposed UAV is discussed in Section 5.4. Section 5.5 is dedicated for the propulsion system design of the platform while Section 5.6 presents the hardware assembly of the vehicle. The chapter concludes by a summary in Section 5.7.

5.1 Background and Motivation

In recent decades, Unmanned Aerial Vehicles (UAVs) have attracted growing attention in research due to their wide applications and large potential [88, 89, 90, 18]. The ultimate goal of all studies in both industry and research centres is to minimize the power requirements, and improve the capability and stability of UAVs (see [3] and the references therein). These development factors lead to various conventional and non-conventional structure designs and configurations of UAV systems aiming for more efficiency in term of size, autonomy, payload capacity and maneuverability among other factors [3, 91]. One such design that attracts increasing interest is the vertical-take-off-and-landing (VTOL) tri-rotor configuration. Tri-rotor vehicles are systems of three rotors arrangement. This configuration has been proposed as less-expensive and efficient design with more flexibility and great agility [91, 50, 63, 92]. Compared to quadrotors, tri-rotor UAVs are smaller in size, less complex, less costly and have longer flight time due to the reduction in number of motors [91, 63], which makes tri-rotor vehicles ideal for deployment in various research projects and missions [92, 93, 94].

On another perspective, thrust vectoring has been used in various designs of aerial vehicles to maximize the capability of UAVs [9]. Thrust vectoring is of significant benefit in some applications to arbitrarily orient the vehicle body with respect to the vehicle acceleration vector, e.g., for aircrafts carrying directional sensors that have to be pointed at targets in the earth reference frame [95]. In addition, thrust vectoring mechanism is used to give UAVs the capability of taking-off and landing in very narrow areas [96]. Large scale helicopters and aircrafts employ complex mechanisms to achieve thrust vectoring capabilities [97]. In small aircrafts and UAVs, a simple technique of tilt-rotor mechanism can be used to obtain thrust vectoring where the propulsion unit(s) are inclined in certain angles using an additional control motor to get the desired thrust in different directions. In general, tilt-rotor mechanism is used in tri-rotor systems to control the horizontal forces and yaw torque of the vehicle. Typically, one rotor only, referred to as the tail rotor, has the ability to tilt to control the yaw moment in tri-rotor systems, see for example [92, 50, 98].

Dynamics of tri-rotor vehicles are highly coupled and nonlinear, which makes the control design of these vehicles the key for successful flight and operations [63]. Compared

to quadrotor systems, the yaw control of tri-rotor systems is a further challenge due to the asymmetric configuration of the system. For instance, the reactive yaw moments in quadrotor systems is decoupled from pitch and roll moments which simplifies the yaw control design in such systems. In contrary, pitch, roll and yaw moments are highly coupled in tri-rotor systems. Moreover, attitude control of these vehicles is more challenging compared to quadrotor systems due to gyroscopic and Coriolis terms. In [63], the authors propose a tri-rotor system of which the control design is implemented by four loops for attitude control and guidance. This control design is complicated with coupling between attitude and position control loops and high computation load. The authors in [91] propose a tri rotor configuration in which all rotors of the system are tilting simultaneously to the same angle to attain yaw control. The control design considers only the attitude stabilization and neglects the trajectory tracking. The control algorithm in [50] is based on nest saturation for decoupled channels where the configuration of the vehicle makes the separate control of attitude and position possible. The control design of the tri-rotor UAV proposed in [94] discusses only the hovering position. In [99], the attitude of the proposed tri-rotor UAV is controlled by using differential thrust concept between the rotors. The control system design in [100] controls the yaw angle of the proposed tri-rotor UAV by differentially tilting the two main rotors in the plane of symmetry while a fixed up-right propeller is used at the tail to control the pitch moment.

This chapter proposes a novel tri-rotor platform, herein referred to as the Tri-rotor UAV, with six degree of freedom using thrust vectoring technique. Few researchers have identified the structure of tri-rotor UAV combined with full independent tilt-rotor capability. The proposed UAV system is designed to achieve six degree of freedom with the highest level of flexibility, manoeuvrability and minimum requirement of power. The Tri-rotor has a triangular shape of three arms where at the each arm, a fixed pitch propeller is driven by a DC motor, and a tilting mechanism is employed to tilt the motor-propeller assembly and produce thrust in the desired direction. The three propellers can tilt independently to achieve full authority of torque and force vectoring. A centralized feedback linearisation control associated with \mathcal{H}_∞ loop shaping design is proposed to stabilize the vehicle's attitude and track the position trajectory. This centralized control is advantageous in which it is a single loop control that manages all channels simultaneously and helps to attenuate unmodeled coupling dynamics between translational and rotational motion.

5.2 System Structure and Design

The structure of the proposed Tri-rotor UAV is depicted in Figure 5.1 and Figure 5.2. It has a triangular structure of three arms of identical length l and at the end of each arm, a force generating unit is mounted to produce part of the required controlling force/torque. All three force generating units are identical and each unit consists of a fixed pitch propeller driven by a brushless DC (BLDC) motor to generate thrust. The three motors can be powered by a single battery pack or three separate packs located at the center of the body. The design of the propulsion unit of the Tri-rotor UAV will be discussed in detail in Section 5.5 while the hardware assembly of the system is investigated in Section 5.6.

The propeller-motor assembly is attached to the body arm via a servo motor that can rotate in a vertical plane to tilt the propeller-motor assembly with an angle α_s in the range $-\frac{\pi}{2} \leq \alpha_s \leq \frac{\pi}{2}$ to produce a horizontal component of the generated force in addition to the vertical part, see Figure 5.3. All three propellers can be tilted independently to give full authority of thrust vectoring. The system has six degree of freedom in which all movements can be achieved independently and directly by changing the norm of the generated thrust and the tilting angles. This configuration enables the vehicle body to stay aligned in the required direction regardless of the movement the UAV makes.

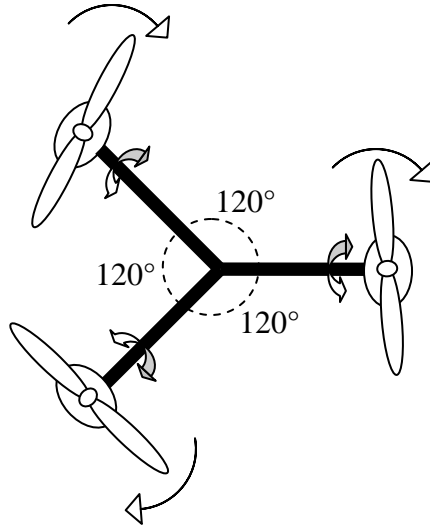


Figure 5.1: The design of the Tri-rotor UAV (top view).

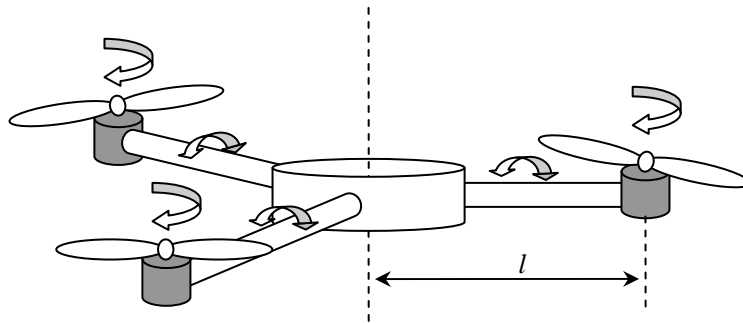


Figure 5.2: The design of the Tri-rotor UAV (3D view).

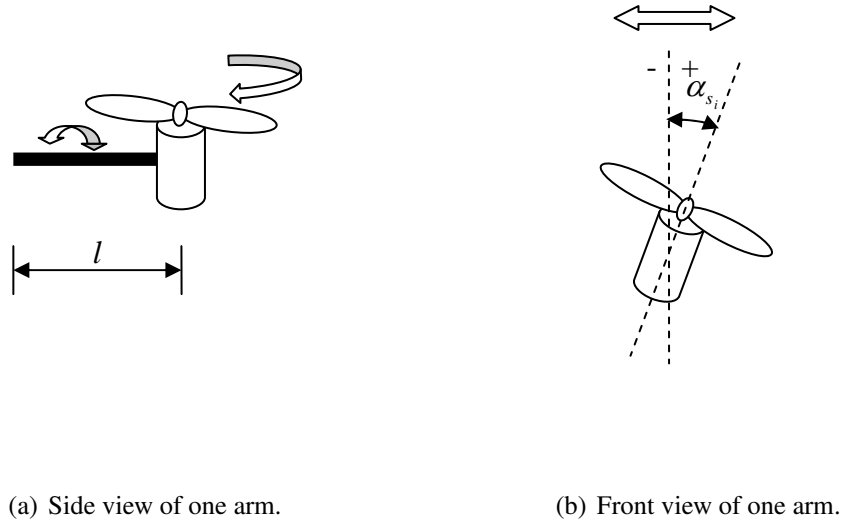


Figure 5.3: The design of one arm of the Tri-rotor UAV.

5.3 Mathematical Modeling

This section presents in detail a mathematical model that captures the dynamics of the Tri-rotor UAV. It starts by listing all variables and coordinate systems used to derive the model of the vehicle. Then, the dynamics of the system along with the torques and forces generated by the actuators is derived.

5.3.1 Reference Coordinate Systems and Notations

We consider the following right hand coordinate systems shown in Figure 5.4:

e: the generalized earth coordinate system of axes X_e, Y_e, Z_e .

b: the body fixed coordinate system in which the origin coincides with the centre of mass of the UAV. The axes of frame *b* are denoted X_b, Y_b, Z_b .

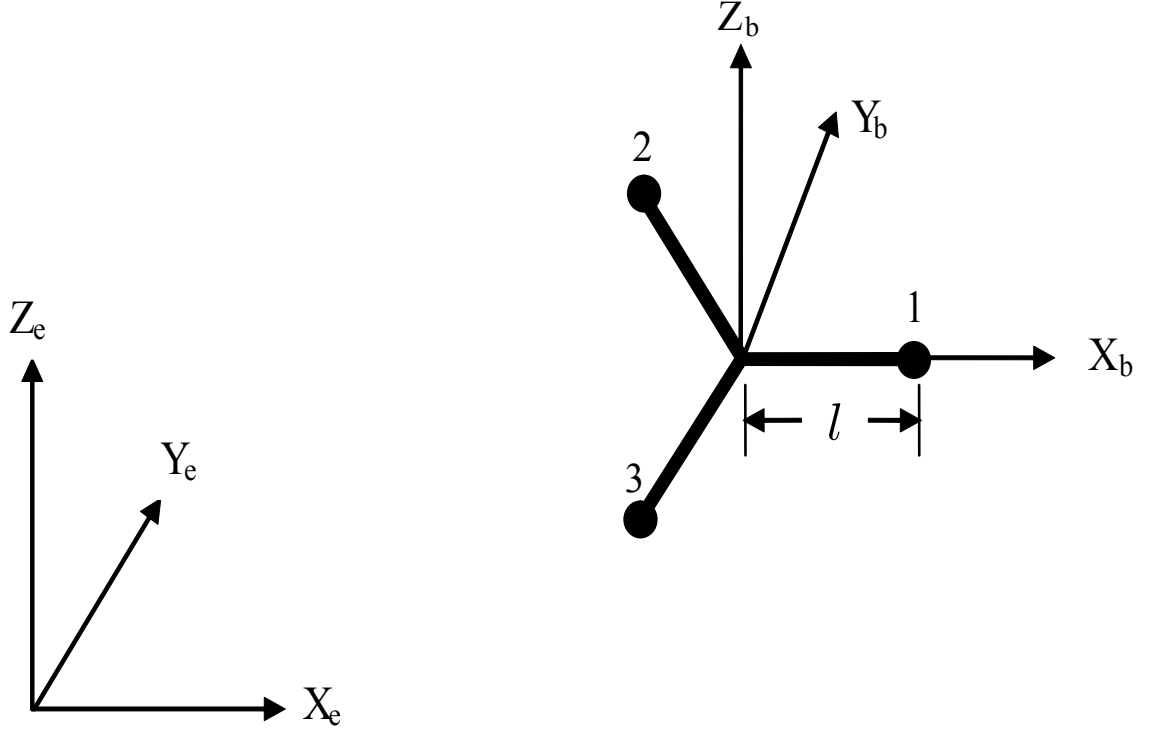


Figure 5.4: Coordinate systems used to develop the UAV dynamic model.

In addition, we choose three right hand coordinate systems l_i of axes X_{l_i} , Y_{l_i} , Z_{l_i} with $i = 1, 2, 3$. These coordinate systems are termed as local coordinate systems which are located at the three propeller locations, see Figure 5.5. The origin of each local coordinate system coincides with the joining point between the UAV arm and the propulsion unit where X_{l_i} is extended outside the i^{th} arm of the UAV and Z_{l_i} is along the BLDC motor shaft axis when the tilting angle is zero.

The rotation matrices between the defined coordinate systems are denoted by:

\mathbf{R}_e^b : the rotational matrix from frame e to frame b .

\mathbf{R}_b^e : the rotational matrix from frame b to frame e .

$\mathbf{R}_{l_i}^b$: the rotational matrix from coordinate system l_i to coordinate system b , $i = 1, 2, 3$.

In the sequel, the following notations are used to indicate the coordinate system in which

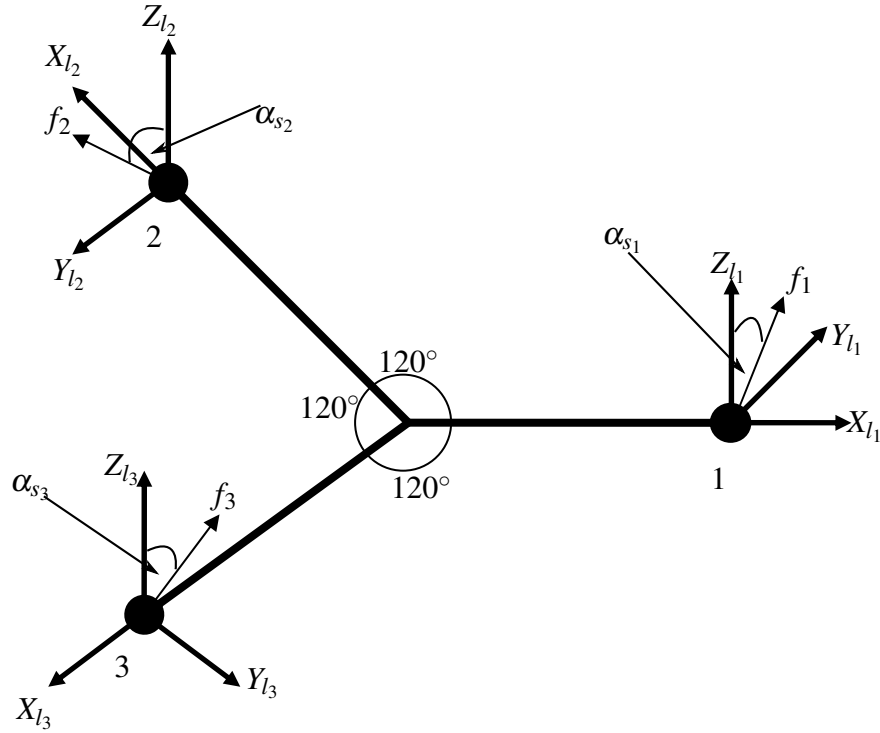


Figure 5.5: Local coordinate systems at the three propulsion units.

vectors are expressed.

The superscript b denotes the body coordinate system.

The superscript e denotes the earth coordinate system.

The superscript l_i denotes the i^{th} local coordinate system.

In addition to the coordinate systems, the following notations are used in the following sections:

ω_{m_i} : rotational speed of the i^{th} BLDC motor.

ω_{p_i} : rotational speed of the i^{th} propeller.

α_{s_i} : tilting angle of the i^{th} servo motor.

f_i : the generated propulsive force from the i^{th} propeller in the direction of the motor shaft.

F_{p_i} : the generated propulsive force vector from the i^{th} propeller expressed in the Cartesian Space.

$F_{p\Sigma}$: total propulsive force generated by all propellers.

F_g : force due to gravity.

k_f : thrust to speed constant of the propeller.

k_t : drag torque to speed constant resulting from the rotation of the propeller.

g : gravitational acceleration.

M_{tot} : the total mass of the UAV.

l : length of Tri-rotor UAV arm which is the distance between the propulsion unit and the center of mass of the UAV (identical for the three motors).

τ_{p_i} : propulsive torque resulting from the generated propulsive force of the i^{th} propeller around the center of mass of the UAV and expressed in the Cartesian Space.

$\tau_{p\Sigma}$: total propulsive torque from all propellers around the center of mass of the vehicle.

$\tau_{d_{p_i}}$: drag torque due to the rotation of the i^{th} propeller.

$\tau_{d\Sigma}$: total drag torque from all three propellers.

I_v : inertia matrix of the UAV.

v_v : velocity vector of the UAV expressed in the Cartesian Space.

ω_v : angular velocity vector of the UAV expressed in the Cartesian Space.

ϕ_v : the roll angle of the UAV related to the earth coordinate system.

θ_v : the pitch angle of the UAV related to the earth coordinate system.

ψ_v : the yaw angle of the UAV related to the earth coordinate system.

x_v : the x coordinate position of the UAV in the earth coordinate system.

y_v : the y coordinate position of the UAV in the earth coordinate system.

z_v : the altitude of the UAV in the earth coordinate system.

5.3.2 UAV Model

In order to obtain the dynamic equations of the UAV, we need to obtain all forces and torques acting on the system before deriving the dynamic equations of the vehicle. In the sequel, the subscript i refers to the i^{th} BLDC motor, servo motor or propeller as applies where $i = 1, 2, 3$. At this stage, we assume actuators, i.e., BLDC motors and servo motors, are very fast and their dynamics are neglected. This assumption is revisited again in details when considering the control design of the UAV in Section 5.4.

5.3.2.1 Forces

There are two main forces acting on the UAV which are the propulsive force and the gravitational force.

The propulsive force

The total propulsive force $F_{p\Sigma}$ is equal to the algebraic sum of the three individual propulsive forces generated from propellers. The individual propulsive forces of the three propellers expressed in the local coordinate systems can be written as:

$$F_{p_i}^{l_i} = \begin{bmatrix} 0 \\ f_i \sin(\alpha_{s_i}) \\ f_i \cos(\alpha_{s_i}) \end{bmatrix}, \quad i = 1, 2, 3. \quad (5.1)$$

Following [54], the individual propulsive force from each propeller in the direction of rotation can be represented as $f_i = k_f \omega_{p_i}^2$, where k_f is identical for all three propellers. We assume that the motor is driving the propeller directly and therefore the rotational speed of the motor equals the rotational speed of the propeller; i.e., $\omega_{m_i} = \omega_{p_i}$. Then, the individual propulsive forces in the local coordinate systems are:

$$F_{p_i}^{l_i} = \begin{bmatrix} 0 \\ k_f \omega_{m_i}^2 \sin(\alpha_{s_i}) \\ k_f \omega_{m_i}^2 \cos(\alpha_{s_i}) \end{bmatrix}. \quad (5.2)$$

In the body coordinate system, the propulsive forces are given by:

$$F_{p_i}^b = \mathbf{R}_{l_i}^b F_{p_i}^{l_i}. \quad (5.3)$$

Therefore, to obtain the propulsive force in the body frame b , we need to find the rotation matrices $\mathbf{R}_{l_1}^b$, $\mathbf{R}_{l_2}^b$ and $\mathbf{R}_{l_3}^b$. The general form of the rotation matrix from a fixed coordinate system 1 to a rotating coordinate system 2 using the notation of the rotation angles Roll

ϕ_{12} , Pitch θ_{12} and Yaw ψ_{12} is given in [101] as:

$$\mathbf{R}_1^2 = \begin{bmatrix} C_{\theta_{12}}C_{\psi_{12}} & C_{\theta_{12}}S_{\psi_{12}} & -S_{\theta_{12}} \\ -C_{\phi_{12}}S_{\psi_{12}} + S_{\phi_{12}}S_{\theta_{12}}C_{\psi_{12}} & C_{\phi_{12}}C_{\psi_{12}} + S_{\phi_{12}}S_{\theta_{12}}S_{\psi_{12}} & S_{\phi_{12}}C_{\theta_{12}} \\ S_{\phi_{12}}S_{\psi_{12}} + C_{\phi_{12}}S_{\theta_{12}}C_{\psi_{12}} & -S_{\phi_{12}}C_{\psi_{12}} + C_{\phi_{12}}S_{\theta_{12}}S_{\psi_{12}} & C_{\phi_{12}}C_{\theta_{12}} \end{bmatrix}, \quad (5.4)$$

where $C. = \cos(\cdot)$, $S. = \sin(\cdot)$ and the sequence of the rotation is ψ_{12} , θ_{12} and then ϕ_{12} .

In our case, the rotation angles from the local coordinate systems to the body coordinate system can be deduced from Figure 5.5 as:

From l_1 to b : $\phi_{l_1b} = 0$, $\theta_{l_1b} = 0$ and $\psi_{l_1b} = 0$.

From l_2 to b : $\phi_{l_2b} = 0$, $\theta_{l_2b} = 0$ and $\psi_{l_2b} = -2\pi/3$.

From l_3 to b : $\phi_{l_3b} = 0$, $\theta_{l_3b} = 0$ and $\psi_{l_3b} = 2\pi/3$.

Replacing the above angles in Eq. (5.4), we have the required rotation matrices from the local coordinate systems l_1 , l_2 and l_3 to the body coordinate system b as:

$$\mathbf{R}_{l_1}^b = \begin{bmatrix} 1 & 0 & 0 \\ 0 & 1 & 0 \\ 0 & 0 & 1 \end{bmatrix}, \quad (5.5)$$

$$\mathbf{R}_{l_2}^b = \begin{bmatrix} -\frac{1}{2} & -\frac{\sqrt{3}}{2} & 0 \\ \frac{\sqrt{3}}{2} & -\frac{1}{2} & 0 \\ 0 & 0 & 1 \end{bmatrix}, \quad (5.6)$$

$$\mathbf{R}_{l_3}^b = \begin{bmatrix} -\frac{1}{2} & \frac{\sqrt{3}}{2} & 0 \\ -\frac{\sqrt{3}}{2} & -\frac{1}{2} & 0 \\ 0 & 0 & 1 \end{bmatrix}. \quad (5.7)$$

Using Equations (5.5) - (5.7), the individual propulsive force in the body coordinate system are:

$$F_{p_1}^b = \begin{bmatrix} 0 \\ k_f \omega_{m_1}^2 \sin(\alpha_{s_1}) \\ k_f \omega_{m_1}^2 \cos(\alpha_{s_1}) \end{bmatrix}, \quad (5.8)$$

$$F_{p_2}^b = \begin{bmatrix} -\frac{\sqrt{3}}{2} k_f \omega_{m_2}^2 \sin(\alpha_{s_2}) \\ -\frac{1}{2} k_f \omega_{m_2}^2 \sin(\alpha_{s_2}) \\ k_f \omega_{m_2}^2 \cos(\alpha_{s_2}) \end{bmatrix}, \quad (5.9)$$

$$F_{p_3}^b = \begin{bmatrix} \frac{\sqrt{3}}{2} k_f \omega_{m_3}^2 \sin(\alpha_{s_3}) \\ -\frac{1}{2} k_f \omega_{m_3}^2 \sin(\alpha_{s_3}) \\ k_f \omega_{m_3}^2 \cos(\alpha_{s_3}) \end{bmatrix}, \quad (5.10)$$

and finally the total propulsive force is:

$$F_{p\Sigma}^b = F_{p_1}^b + F_{p_2}^b + F_{p_3}^b \quad (5.11)$$

$$= k_f \mathbf{H}_f \boldsymbol{\rho}. \quad (5.12)$$

where

$$\mathbf{H}_f = \begin{bmatrix} 0 & -\frac{\sqrt{3}}{2} & \frac{\sqrt{3}}{2} & 0 & 0 & 0 \\ 1 & -\frac{1}{2} & -\frac{1}{2} & 0 & 0 & 0 \\ 0 & 0 & 0 & 1 & 1 & 1 \end{bmatrix}, \quad (5.13)$$

and

$$\boldsymbol{\rho} = \begin{bmatrix} \omega_{m_1}^2 \sin(\alpha_{s_1}) \\ \omega_{m_2}^2 \sin(\alpha_{s_2}) \\ \omega_{m_3}^2 \sin(\alpha_{s_3}) \\ \omega_{m_1}^2 \cos(\alpha_{s_1}) \\ \omega_{m_2}^2 \cos(\alpha_{s_2}) \\ \omega_{m_3}^2 \cos(\alpha_{s_3}) \end{bmatrix}. \quad (5.14)$$

The gravity force

The gravitational force in the generalized earth coordinate system is given as:

$$F_g^e = \begin{bmatrix} 0 \\ 0 \\ -gM_{tot} \end{bmatrix}. \quad (5.15)$$

In the body coordinate system, we have:

$$F_g^b = \mathbf{R}_e^b F_g^e. \quad (5.16)$$

Obtaining \mathbf{R}_e^b from Eq. (5.4) by using the attitude angles of the UAV ϕ_v , θ_v and ψ_v defined in Section 5.3.1, we have:

$$F_g^b = gM_{tot}H_g \quad (5.17)$$

where

$$H_g = \begin{bmatrix} \sin(\theta_v) \\ -\sin(\phi_v)\cos(\theta_v) \\ -\cos(\phi_v)\cos(\theta_v) \end{bmatrix}. \quad (5.18)$$

Now, the total force acting on the UAV and expressed in the body coordinate system is:

$$F^b = F_{p\Sigma}^b + F_g^b \quad (5.19)$$

$$= k_f \mathbf{H}_f \boldsymbol{\rho} + gM_{tot}H_g. \quad (5.20)$$

5.3.2.2 Torques

Two main torques are acting on the UAV which are namely, the propulsive torque and the drag torque. Expressed in the body coordinate system, these torques are analyzed as following:

The propulsive torque

The propulsive torque is the torque resulting from the generated propulsive force around the center of mass of the vehicle. For the case of the Tri-rotor UAV, we have three identical arms and then the components of the propulsive torque are:

$$\boldsymbol{\tau}_{p_i}^b = \boldsymbol{l}_i^b \times \boldsymbol{F}_{p_i}^b, \quad i = 1, 2, 3 \quad (5.21)$$

where \boldsymbol{l}_i^b is the vector of the i^{th} arm between the centre of mass of the UAV and the propulsion unit expressed in the body coordinate system. $\boldsymbol{F}_{p_i}^b$ is obtained from Equations (5.8) - (5.10) while \boldsymbol{l}_i^b is given by:

$$\boldsymbol{l}_i^b = \boldsymbol{R}_{i_i}^b \begin{bmatrix} l \\ 0 \\ 0 \end{bmatrix}, \quad i = 1, 2, 3, \quad (5.22)$$

where l is the length of the vehicle's arm vector measured between the centre of mass of the UAV and the propulsion unit (identical for the three arms).

Substituting as required from Equations (5.5) - (5.10), the total propulsive torque expressed in the body coordinate system is:

$$\boldsymbol{\tau}_{p_\Sigma}^b = \boldsymbol{\tau}_{p_1}^b + \boldsymbol{\tau}_{p_2}^b + \boldsymbol{\tau}_{p_3}^b \quad (5.23)$$

$$= k_f \boldsymbol{H}_t \boldsymbol{\rho} \quad (5.24)$$

where

$$\boldsymbol{H}_t = l \begin{bmatrix} 0 & 0 & 0 & 0 & \frac{\sqrt{3}}{2} & -\frac{\sqrt{3}}{2} \\ 0 & 0 & 0 & -1 & \frac{1}{2} & \frac{1}{2} \\ 1 & 1 & 1 & 0 & 0 & 0 \end{bmatrix}, \quad (5.25)$$

and $\boldsymbol{\rho}$ is defined in Eq. (5.14).

The drag torque

The drag torque is defined as the torque resulting from the aerodynamic drag forces exerted by the ambient fluid (air) on the propeller [102]. Drag torque is in the opposite direction to the direction of rotation. In our case, the resulting drag torque on the i^{th} propeller can be approximated by $\tau_{d_i} = -k_t \omega_{p_i}^2$ [55]. In the local coordinate systems l_i , the drag torque can be written as:

$$\tau_{d_i}^{l_i} = \begin{bmatrix} 0 \\ -k_t \omega_{m_i}^2 \sin(\alpha_{s_i}) \\ -k_t \omega_{m_i}^2 \cos(\alpha_{s_i}) \end{bmatrix}, \quad i = 1, 2, 3, \quad (5.26)$$

where we consider the DC motors drives the propeller directly, i.e., $\omega_{p_i} = \omega_{m_i}$.

In the body coordinate system, the individual drag torques can be represented as:

$$\tau_{d_1}^b = \mathbf{R}_{l_1}^b \tau_{d_1}^{l_1}, \quad (5.27)$$

$$\tau_{d_2}^b = \mathbf{R}_{l_2}^b \tau_{d_2}^{l_2}, \quad (5.28)$$

$$\tau_{d_3}^b = \mathbf{R}_{l_3}^b \tau_{d_3}^{l_3}. \quad (5.29)$$

Using definitions (5.5) - (5.7), we have:

$$\tau_{d_1}^b = \begin{bmatrix} 0 \\ -k_t \omega_{m_1}^2 \sin(\alpha_{s_1}) \\ -k_t \omega_{m_1}^2 \cos(\alpha_{s_1}) \end{bmatrix}, \quad (5.30)$$

$$\tau_{d_2}^b = \begin{bmatrix} \frac{\sqrt{3}}{2} k_t \omega_{m_2}^2 \sin(\alpha_{s_2}) \\ \frac{1}{2} k_t \omega_{m_2}^2 \sin(\alpha_{s_2}) \\ -k_t \omega_{m_2}^2 \cos(\alpha_{s_2}) \end{bmatrix}, \quad (5.31)$$

$$\tau_{d_3}^b = \begin{bmatrix} -\frac{\sqrt{3}}{2} k_t \omega_{m_3}^2 \sin(\alpha_{s_3}) \\ \frac{1}{2} k_t \omega_{m_3}^2 \sin(\alpha_{s_3}) \\ -k_t \omega_{m_3}^2 \cos(\alpha_{s_3}) \end{bmatrix}. \quad (5.32)$$

Finally, the total drag torque in the body system is given by:

$$\boldsymbol{\tau}_{d\Sigma}^b = \boldsymbol{\tau}_{d_1}^b + \boldsymbol{\tau}_{d_2}^b + \boldsymbol{\tau}_{d_3}^b \quad (5.33)$$

$$= -k_t \mathbf{H}_f \boldsymbol{\rho}, \quad (5.34)$$

where \mathbf{H}_f and $\boldsymbol{\rho}$ are defined in (5.13) and (5.14) respectively.

Now, the total torque acting on the Tri-rotor and expressed in the body coordinate system is:

$$\boldsymbol{\tau}^b = \boldsymbol{\tau}_{p\Sigma}^b + \boldsymbol{\tau}_{d\Sigma}^b \quad (5.35)$$

$$= (k_f \mathbf{H}_t - k_t \mathbf{H}_f) \boldsymbol{\rho} \quad (5.36)$$

In practice, there is another torque acting on the vehicle referred to as gyroscopic torque. The gyroscopic torque results from the titling of the rotating propellers and the angular motion of the UAV body. In UAV literature, it is commonly assumed the gyroscopic torque has a stabilizing effect and therefore it is neglected safely from the model of the system, see for example [103, 104] and the references therein.

Equations (5.12) and (5.36) give mapping between the force and torque exerted on the UAV and the actuators variables. For the static case, we have:

$$\begin{bmatrix} F^b \\ \boldsymbol{\tau}^b \end{bmatrix} = \begin{bmatrix} k_f \mathbf{H}_f \\ -k_t \mathbf{H}_f + k_f \mathbf{H}_t \end{bmatrix} \boldsymbol{\rho}. \quad (5.37)$$

In order to control the Tri-rotor UAV, we need to get the actuators variables in terms of the forces and torques. Therefore, we write:

$$\boldsymbol{\rho} = \begin{bmatrix} k_f \mathbf{H}_f \\ -k_t \mathbf{H}_f + k_f \mathbf{H}_t \end{bmatrix}^{-1} \begin{bmatrix} F^b \\ \boldsymbol{\tau}^b \end{bmatrix}. \quad (5.38)$$

The mapping matrix is of size (6×6) and not singular for any combination of real values for k_t and k_f . The condition number of the mapping matrix depends on the value of k_t and k_f . Broadly speaking k_f is greater than k_t by ten times for small motors. For a normalized values of $k_t = 1$ and $k_f = 10$, the condition number of the mapping matrix is 4.04. Hence the mapping matrix is not ill-conditioned, the inverse exists always and the Tri-rotor UAV is controllable.

5.3.2.3 Dynamic Model

Assuming that the Tri-rotor UAV is a rigid body of fixed mass, the vehicle's motion can be described by the Newton-Euler second's law as [105]:

for translational motion:

$$F^e = \frac{\partial(M_{tot} v_v^e)}{\partial t} = M_{tot} \frac{\partial v_v^e}{\partial t} \quad (5.39)$$

for rotational motion:

$$\tau^e = \frac{\partial(I_v^e \omega_v^e)}{\partial t} \quad (5.40)$$

where F^e and τ^e are respectively the total force and torque acting on the UAV and expressed in the general earth frame system. I_v^e is the inertia matrix of the UAV in regard to the inertial principle axes of the earth coordinate system.

To transfer Equations (5.39) - (5.40) to the body coordinate system, we have:

$$v_v^e = \mathbf{R}_b^e v_v^b \quad (5.41)$$

$$\Rightarrow \frac{\partial v_v^e}{\partial t} = \frac{\partial(\mathbf{R}_b^e v_v^b)}{\partial t} \quad (5.42)$$

$$= \dot{\mathbf{R}}_b^e v_v^b + \mathbf{R}_b^e \dot{v}_v^b \quad (5.43)$$

From the general properties of the rotation matrix, we have:

$$\mathbf{R}_b^e = (\mathbf{R}_e^b)^{-1} = (\mathbf{R}_e^b)^T, \quad (5.44)$$

$$\frac{d((\mathbf{R}_e^b)^T)}{dt} = (\dot{\mathbf{R}}_e^b)^T, \quad (5.45)$$

$$\dot{\mathbf{R}}_e^b = -\mathbf{S}(\omega^b)\mathbf{R}_e^b. \quad (5.46)$$

This leads to [106]:

$$\dot{\mathbf{R}}_b^e = \mathbf{R}_b^e \mathbf{S}(\omega^b) \quad (5.47)$$

and then we write:

$$\frac{\partial \mathbf{v}_v^e}{\partial t} = \mathbf{R}_b^e \dot{\mathbf{v}}_v^b + \mathbf{R}_b^e \mathbf{S}(\omega_v^b) \mathbf{v}_v^b, \quad (5.48)$$

where $\mathbf{S}(\omega^b)$ is the skew matrix of the vector ω_v^b . Given that ω_v^b is written in the Cartesian space as:

$$\omega_v^b = \begin{bmatrix} p \\ q \\ r \end{bmatrix}, \quad (5.49)$$

then, the skew matrix $\mathbf{S}(\omega^b)$ is given as:

$$\mathbf{S}(\omega_v^b) = \begin{bmatrix} 0 & -r & q \\ r & 0 & -p \\ -q & p & 0 \end{bmatrix}. \quad (5.50)$$

Similarly, for Eq. (5.40), we have:

$$\frac{\partial (\mathbf{I}_v^e \omega_v^e)}{\partial t} = \mathbf{R}_b^e \mathbf{I}_v^b \dot{\omega}_v^b + \mathbf{R}_b^e \mathbf{S}(\omega_v^b) \mathbf{I}_v^b \omega_v^b, \quad (5.51)$$

where \mathbf{I}_v^b is the inertia matrix of the UAV with respect to the fixed body coordinate system. Assuming no mass change over time, \mathbf{I}_v^b is fixed.

Finally, knowing that $F^e = \mathbf{R}_b^e F^b$, $\tau^e = \mathbf{R}_b^e \tau^b$ and using (5.48) and (5.51) in (5.39) - (5.40)

leads to:

$$\mathbf{F}^b = M_{tot} \left(\dot{\mathbf{v}}_v^b + \mathbf{S}(\boldsymbol{\omega}_v^b) \mathbf{v}_v^b \right) \quad (5.52)$$

$$\boldsymbol{\tau}^b = \mathbf{I}_v^b \dot{\boldsymbol{\omega}}_v^b + \mathbf{S}(\boldsymbol{\omega}_v^b) \mathbf{I}_v^b \boldsymbol{\omega}_v^b \quad (5.53)$$

Substituting \mathbf{F}^b and $\boldsymbol{\tau}^b$ from (5.20) and (5.36) gives:

$$k_f \mathbf{H}_f \boldsymbol{\rho} + g M_{tot} \mathbf{H}_g = M_{tot} \left(\dot{\mathbf{v}}_v^b + \mathbf{S}(\boldsymbol{\omega}_v^b) \mathbf{v}_v^b \right) \quad (5.54)$$

$$(k_f \mathbf{H}_t - k_t \mathbf{H}_f) \boldsymbol{\rho} = \mathbf{I}_v^b \dot{\boldsymbol{\omega}}_v^b + \mathbf{S}(\boldsymbol{\omega}_v^b) \mathbf{I}_v^b \boldsymbol{\omega}_v^b \quad (5.55)$$

Let $\boldsymbol{\eta}_v$ and $\boldsymbol{\lambda}_v$ be the attitude vector and the position vector of the UAV related to the earth coordinate system and they are given as:

$$\boldsymbol{\eta}_v = \begin{bmatrix} \phi_v \\ \theta_v \\ \psi_v \end{bmatrix}, \quad (5.56)$$

$$\boldsymbol{\lambda}_v = \begin{bmatrix} x_v \\ y_v \\ z_v \end{bmatrix}. \quad (5.57)$$

To fully describe the dynamic equations of the UAV, we have the following relations from [101]:

$$\dot{\boldsymbol{\eta}}_v = \boldsymbol{\Psi} \boldsymbol{\omega}_v^b \quad (5.58)$$

$$\dot{\boldsymbol{\lambda}}_v^e = (\mathbf{R}_e^b)^{-1} \mathbf{v}_v^b \quad (5.59)$$

where $\boldsymbol{\Psi}$ is the rotational matrix between the angular velocity expressed in the body coordinate system $\boldsymbol{\omega}_v^b$ and the angular velocity in the earth coordinate system $\dot{\boldsymbol{\eta}}_v$. $\boldsymbol{\Psi}$ is given in [101] as:

$$\boldsymbol{\Psi} = \begin{bmatrix} 1 & \sin(\phi_v) \tan(\theta_v) & \cos(\phi_v) \tan(\theta_v) \\ 0 & \cos(\phi_v) & -\sin(\phi_v) \\ 0 & \sin(\phi_v) \sec(\theta_v) & \cos(\phi_v) \sec(\theta_v) \end{bmatrix}, \quad \frac{-\pi}{2} < \theta_v < \frac{\pi}{2}. \quad (5.60)$$

From the properties of the rotation matrix we have:

$$(\mathbf{R}_e^b)^{-1} = \mathbf{R}_b^e. \quad (5.61)$$

Finally, from Equations (5.54) - (5.61), the dynamic model of the UAV can be written as:

$$\dot{\mathbf{v}}_v^b = g\mathbf{H}_g - \mathbf{S}(\boldsymbol{\omega}_v^b)\mathbf{v}_v^b + \frac{k_f}{M_{tot}}\mathbf{H}_f\boldsymbol{\rho} \quad (5.62)$$

$$\dot{\boldsymbol{\omega}}_v^b = -(\mathbf{I}_v^b)^{-1}\mathbf{S}(\boldsymbol{\omega}_v^b)\mathbf{I}_v^b\boldsymbol{\omega}_v^b + (\mathbf{I}_v^b)^{-1}(k_f\mathbf{H}_t - k_t\mathbf{H}_f)\boldsymbol{\rho} \quad (5.63)$$

$$\dot{\boldsymbol{\eta}}_v = \boldsymbol{\Psi}\boldsymbol{\omega}_v^b \quad (5.64)$$

$$\dot{\boldsymbol{\lambda}}_v^e = \mathbf{R}_b^e\mathbf{v}_v^b \quad (5.65)$$

This model of the UAV is written in compact form in which every state variable is a vector of three components as:

$$\mathbf{v}_v^b = \begin{bmatrix} u \\ v \\ w \end{bmatrix}, \boldsymbol{\omega}_v^b = \begin{bmatrix} p \\ q \\ r \end{bmatrix}, \boldsymbol{\eta}_v = \begin{bmatrix} \phi_v \\ \theta_v \\ \psi_v \end{bmatrix}, \boldsymbol{\lambda}_v^e = \begin{bmatrix} x_v \\ y_v \\ z_v \end{bmatrix}. \quad (5.66)$$

Equations (5.62) - (5.65) show a nonlinear model with coupling between the translational and rotational dynamics of the UAV. Moreover, there is coupling between inputs and output channels in which all inputs act on all outputs. The channels coupling along with the nonlinearity of the system makes the control design of the Tri-rotor UAV a real challenge compared with other UAV configurations. On the other hand, if we consider the control problem of the UAV to be position tracking with attitude regulating, then the system is fully actuated in which there are six actuators (three BLDC motor speeds and three servo angles) and six outputs (3D position and three attitude angles). This highlights the positive aspect of the proposed configuration in terms of controller design compared with other UAV structures which are under-actuated systems like quadrotors. The control design of the Tri-rotor UAV will be discussed in next section.

5.4 Control System Design

In this section we consider the control design for the proposed Tri-rotor UAV using input-output feedback linearisation associated with \mathcal{H}_∞ Loop Shaping Design Procedure (LSDP). The control design of the system can be seen as a tracking problem for the position and attitude of the vehicle via the speed of the BLDC motors and the angles of the servo motors. In this case, the system is fully actuated having six outputs and six inputs. The proposed control algorithm is a centralized \mathcal{H}_∞ controller that stabilizes and tracks simultaneously all outputs, i.e., 3D position and three attitude angles. The motivation behind such a centralized control design is to synthesize a robust controller that can compensate for any unmodeled coupling between channels and attenuate cross-coupling noises and disturbances. Moreover, the implementation of such a design is simple via single feedback loop structure. The procedure for the control design in this section is:

- linearize the system using feedback linearisation,
- synthesize a centralized linear controller using \mathcal{H}_∞ LSDP,
- simulate the system to check time domain specifications.

We start by designing a controller for the system using feedback linearisation without considering actuator dynamics and then, the synthesized controller is applied to the full UAV model including actuator dynamics to demonstrate the effect of unmodeled actuator dynamics on the stability of system. After that, the two stage feedback linearisation developed in Chapter 2 is implemented to linearize the system and synthesize a linear \mathcal{H}_∞ controller with a comparison study between the the two stage feedback linearisation and the full system (including actuator dynamics) feedback linearisation. The performance of the controller in all cases is simulated using Matlab Simulink software.

5.4.1 Control Synthesis Without Actuator Dynamics

At this stage, actuator dynamics are neglected assuming that actuators are fast enough to apply the control action without a considerable delay. This assumption will be challenged and analysed later. The control design includes feedback linearisation of the UAV model and then a linear \mathcal{H}_∞ control synthesis for the linearized system.

5.4.1.1 Feedback Linearisation Without Actuator Dynamics

We linearize the model of the Tri-rotor UAV using input-output feedback linearisation. We recall the dynamic equations of the Tri-rotor UAV from (5.62) - (5.65):

$$\dot{v}_v^b = gH_g - \mathbf{S}(\omega_v^b)v_v^b + \frac{k_f}{M_{tot}}\mathbf{H}_f\rho \quad (5.67)$$

$$\dot{\omega}_v^b = -(\mathbf{I}_v^b)^{-1}\mathbf{S}(\omega_v^b)\mathbf{I}_v^b\omega_v^b + (\mathbf{I}_v^b)^{-1}(k_f\mathbf{H}_t - k_t\mathbf{H}_f)\rho \quad (5.68)$$

$$\dot{\eta}_v = \mathbf{\Psi}\omega_v^b \quad (5.69)$$

$$\dot{\lambda}_v^e = \mathbf{R}_b^e v_v^b \quad (5.70)$$

For simplicity of expression, the superscript b and e as well as the subscript v will not be written from now on unless it is necessary to avoid ambiguity. Therefore, Equations (5.67) - (5.70) can be written as:

$$\dot{v} = gH_g - \mathbf{S}(\omega)v + \frac{k_f}{M_{tot}}\mathbf{H}_f\rho \quad (5.71)$$

$$\dot{\omega} = -(\mathbf{I})^{-1}\mathbf{S}(\omega)\mathbf{I}\omega + (\mathbf{I})^{-1}(k_f\mathbf{H}_t - k_t\mathbf{H}_f)\rho \quad (5.72)$$

$$\dot{\eta} = \mathbf{\Psi}\omega \quad (5.73)$$

$$\dot{\lambda} = \mathbf{R}_b^e v \quad (5.74)$$

This model of the UAV is written in the compact form in which every state is a vector of three components, i.e., $x \in \mathbb{R}^{12}$.

The control problem of the UAV can be seen as tracking a position and attitude trajectory using the speed of the BLDC motors and the angles of the servos. Therefore, we consider the vector ρ as the input vector for the system, i.e., $u = \rho$, and the output is defined as:

$$y = \begin{bmatrix} \eta \\ \lambda \end{bmatrix} \quad (5.75)$$

Now, to implement input-output feedback linearisation, we have:

$$\dot{y} = y^{(1)} = \begin{bmatrix} \dot{\eta} \\ \dot{\lambda} \end{bmatrix} = \begin{bmatrix} \mathbf{\Psi}\omega \\ \mathbf{R}_b^e v_v \end{bmatrix} \quad (5.76)$$

and

$$\ddot{y} = y^{(2)} = \begin{bmatrix} \dot{\mathbf{\Psi}}\omega + \mathbf{\Psi}\dot{\omega} \\ (\mathbf{R}_b^e \dot{v} + \mathbf{R}_b^e \dot{v}) \end{bmatrix} \quad (5.77)$$

From the properties of the rotation matrix in (5.47) and the model equations (5.71) - (5.72), we can write:

$$\begin{aligned} y^{(2)} &= \begin{bmatrix} \dot{\mathbf{\Psi}}\omega + \mathbf{\Psi}(-\mathbf{I}^{-1}\mathbf{S}(\omega)\mathbf{I}\omega + \mathbf{I}^{-1}(k_f\mathbf{H}_t - k_t\mathbf{H}_f)u) \\ \mathbf{R}_b^e\mathbf{S}(\omega)v + \mathbf{R}_b^e(g\mathbf{H}_g - \mathbf{S}(\omega)v + \frac{k_f}{M_{tot}}\mathbf{H}_f u) \end{bmatrix} \\ &= \begin{bmatrix} (\dot{\mathbf{\Psi}} - \mathbf{\Psi}\mathbf{I}^{-1}\mathbf{S}(\omega)\mathbf{I})\omega \\ g\mathbf{R}_b^e\mathbf{H}_g \end{bmatrix} + \begin{bmatrix} \mathbf{\Psi}\mathbf{I}^{-1}(k_f\mathbf{H}_t - k_t\mathbf{H}_f) \\ \frac{k_f}{M_{tot}}\mathbf{R}_b^e\mathbf{H}_f \end{bmatrix} u \end{aligned} \quad (5.78)$$

where we have:

$$\dot{\mathbf{\Psi}} = \frac{\partial \mathbf{\Psi}}{\partial \phi_v} \dot{\phi}_v + \frac{\partial \mathbf{\Psi}}{\partial \theta_v} \dot{\theta}_v \quad (5.79)$$

and $\dot{\phi}_v$, $\dot{\theta}_v$ are obtained from Eq. (5.69) as

$$\dot{\eta} = \begin{bmatrix} \dot{\phi}_v \\ \dot{\theta}_v \\ \dot{\psi}_v \end{bmatrix} = \mathbf{\Psi}\omega \quad (5.80)$$

The relative degree of the system in the compact form is $r = r_1 + r_2 = 2 + 2 = 4$ which is

equal to the number of state vectors in the compact form of the dynamic equations, and there is no zero dynamics.

We define the matrix $\boldsymbol{\beta}(x)$ as:

$$\boldsymbol{\beta}(x) = \begin{bmatrix} \boldsymbol{\Psi}I^{-1} (k_f H_t - k_t \mathbf{H}_f) \\ \frac{k_f}{M_{tot}} \mathbf{R}_b^e \mathbf{H}_f \end{bmatrix}. \quad (5.81)$$

We have $\det[\boldsymbol{\beta}(x)] \neq 0$ and the inverse $\boldsymbol{\beta}^{-1}(x)$ exists always¹ for all $x \in \mathbb{R}^{12}$ where x represents the states of the system:

$$x = \begin{bmatrix} v \\ \omega \\ \eta \\ \lambda \end{bmatrix}$$

To linearize the system, we choose a new control input $\vartheta = \begin{bmatrix} \vartheta_1 \\ \vartheta_2 \end{bmatrix}$, and we define the system dynamics as:

$$y^{(2)} = \vartheta. \quad (5.82)$$

Now from Eq. (5.78) we can write the feedback linearisation law as:

$$u = \boldsymbol{\beta}^{-1} \left(\vartheta - \begin{bmatrix} (\dot{\boldsymbol{\Psi}} - \boldsymbol{\Psi}I^{-1} \mathbf{S}(\omega)I) \omega \\ g \mathbf{R}_b^e H_g \end{bmatrix} \right). \quad (5.83)$$

¹It is always assumed that $-\pi/2 < \theta_v < \pi/2$

The linearized model in the compact form is given as:

$$\dot{\zeta} = \begin{bmatrix} 0 & 1 & 0 & 0 \\ 0 & 0 & 0 & 0 \\ 0 & 0 & 0 & 1 \\ 0 & 0 & 0 & 0 \end{bmatrix} \zeta + \begin{bmatrix} 0 & 0 \\ 1 & 0 \\ 0 & 0 \\ 0 & 1 \end{bmatrix} \vartheta \quad (5.84)$$

$$y = \begin{bmatrix} 1 & 0 & 0 & 0 \\ 0 & 0 & 1 & 0 \end{bmatrix} \zeta \quad (5.85)$$

where

$$\zeta = \begin{bmatrix} \eta \\ \dot{\eta} \\ \lambda \\ \dot{\lambda} \end{bmatrix} \in \mathbb{R}^{12}, \quad y = \begin{bmatrix} \eta \\ \lambda \end{bmatrix} \in \mathbb{R}^6, \quad \vartheta = \begin{bmatrix} \vartheta_1 \\ \vartheta_2 \end{bmatrix} \in \mathbb{R}^6.$$

The linearized plant is a double integrator representing single degree of freedom for translational and rotational motion. In control applications, double integrator system is one of the fundamental systems that represents many applications [107].

The resulting double integrator linear system can be controlled using a linear control method. In this thesis, we invoke the \mathcal{H}_∞ Loop Shape Design procedure (LSDP) as one of robust control techniques that can be used to synthesize a controller for the linearized system. The concept of \mathcal{H}_∞ LSDP and its strengths are reviewed in next section.

5.4.1.2 Review of \mathcal{H}_∞ Loop Shaping Design

In literature of linear system control, \mathcal{H}_∞ Loop Shaping Design Procedure (LSDP) is proposed by [108] as an effective method for synthesizing robust controllers and has been implemented successfully in wide range of applications (see [109, 110, 111, 112] and the references therein). This section aims to briefly review the concept of \mathcal{H}_∞ LSDP and recall the standard implementation steps of this control synthesis method. Figure 5.6 represents a typical framework for the \mathcal{H}_∞ LSDP where this control method aims to design the performance of the closed loop system by shaping the singular values of the scaled plant P using compensators W_1 and W_2 . Once the desired shaped plant P_s

is obtained, the optimal robust stability margin $b_{opt}(P_s)$ is calculated and the set of all internally stabilizing controllers C_∞ to achieve a robust stability margin $b(P_s) < b_{opt}(P_s)$ is designed. The final controller for the scaled nominal plant P is $C = W_1 C_\infty W_2$.

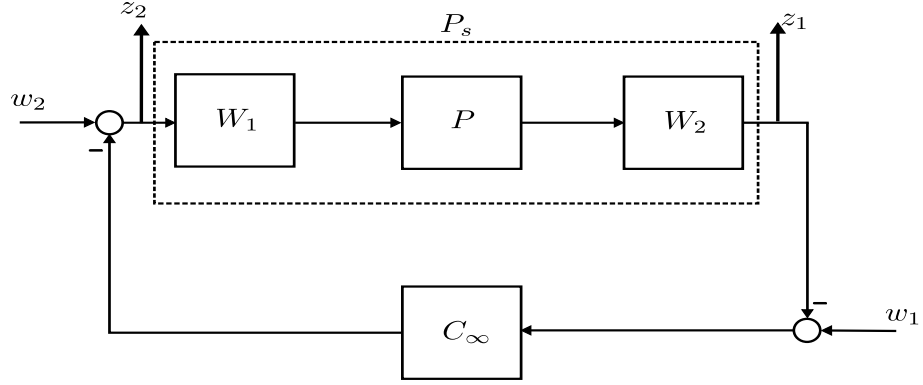


Figure 5.6: Typical framework for \mathcal{H}_∞ loop shaping design procedure.

Given a shaped plant P_s that has a normalized right Coprime factorization over \mathcal{RH}_∞ defined by $P_s = N_s M_s^{-1}$ and a controller C_∞ , then, the feedback interconnection $[\tilde{P}_s, C_\infty]$ is internally stable where \tilde{P}_s is a perturbed plant given by

$$\tilde{P}_s = (N_s + \Delta_{N_s})(M_s + \Delta_{M_s})^{-1}$$

such that:

$$\left\| \begin{bmatrix} \Delta_{N_s} \\ \Delta_{M_s} \end{bmatrix} \right\|_\infty \leq b(P_s, C_\infty).$$

and $(M_s + \Delta_{M_s})$ is invertible, where Δ_{N_s} and Δ_{M_s} are stable unknown transfer matrices that represent the uncertainty. $P_s = W_2 P W_1$ and $b(P_s, C_\infty)$ is the robust stability margin. The robust stability margin for a shaped plant P_s and a controller C_∞ is defined by [113]:

$$b(P_s, C_\infty) = \begin{cases} \left\| \begin{bmatrix} P_s \\ I \end{bmatrix} (I - C_\infty P_s)^{-1} \begin{bmatrix} -C_\infty & I \end{bmatrix} \right\|_\infty^{-1} & \text{if } [P_s, C_\infty] \text{ is internally stable,} \\ 0 & \text{otherwise.} \end{cases}$$

The largest value of robust stability margin is given by:

$$b_{opt} = \sup_{C_\infty} b(P_s, C_\infty)$$

and it has been proved that $b_{opt} \leq 1$ for any plant P_s , i.e., $0 \leq b(P_s) \leq 1$ for any plant P_s [114].

The interconnection $[P_s, C_\infty]$ is assumed to be internally stable, which means all transfer functions of the mapping from $\begin{bmatrix} w_1 \\ w_2 \end{bmatrix}$ to $\begin{bmatrix} z_1 \\ z_2 \end{bmatrix}$ exist (well-posedness) and they belong to \mathcal{RH}_∞ .

\mathcal{H}_∞ loop-shaping design is seen as a sensible control design tool due to the fact that the controller C_∞ guarantees the robust stability of the closed loop system while the weights W_1 and W_2 specify the performance of the loop at low and high frequency. The controller C_∞ shapes only the phase of the shaped plant P_s around the crossover frequency to improve robustness while it does not modify the loop-shape significantly at low and high frequency. Therefore, the performance objectives can be specified by designer via shaping the singular values of the open loop plant P using frequency dependent compensators W_1 and W_2 .

5.4.1.3 The Standard \mathcal{H}_∞ Loop Shaping Design Procedure

In the following, we recall the standard \mathcal{H}_∞ loop shaping design procedure proposed by [108] and summarized in [115].

1. Scale the nominal plant P_n using pre and post scaling matrices S_1 and S_2 to obtain the scaled nominal plant $P = S_2 P_n S_1$. This step is important to compensate for the difference between the input and output units of the system.
2. Use frequency dependent compensators W_1 and W_2 to shape the singular values of the scaled nominal plant P and obtain the desired performance requirement. For the chosen W_1 and W_2 , the interconnection $W_2 P W_1$ should contain no hidden modes.

3. Compute $b_{opt}(P_s)$. Following [116], it is suggested that a value of $b_{opt}(P_s) \geq 0.3$ is usually good enough and it is somehow equivalent to gain margin of 5.4 dB and phase margin of 35° for a SISO design. Therefore, if $b_{opt}(P_s) \ll 0.3$, this indicates an incompatibility of the designed loop-shape with robust stability or performance. In this case, the designer needs to go to Step 2 to design a better loop shape.
4. Synthesize a controller C_∞ that achieves a robust stability margin $b(P_s, C_\infty)$ less than or equal to the calculated optimal stability margin $b_{opt}(P_s)$. The justification for this design choice is that optimal controllers cannot be written in an observer form.
5. Obtain the real controller by pulling around the loop-shaping weights W_1, W_2 and the scaling matrices S_1, S_2 . Hence, the final synthesized controller for the real plant is $C = S_1 W_1 C_\infty W_2 S_2$.
6. Verify the robust performance of the closed-loop system by checking time-domain response characterizations (settling time, overshoot, saturation, etc.) and tune as necessary.

5.4.1.4 Control Synthesis and Simulation Results: W/o Actuator Dynamics

The \mathcal{H}_∞ loop-shaping design motivated in Section 5.4.1.2 is used here to synthesize a controller for the linearized system of the Tri-rotor UAV. For selection of weights to shape the linearized plant, we consider the following control design specifications:

- high loop-gain at low frequency for good reference tracking and disturbance rejection.
- low loop-gain at high frequency for robustness against unmodeled dynamics and output measurement noise.
- reasonable bandwidth for fast response.

An algorithm proposed in [117] is invoked to simultaneously optimize the synthesis of loop-shaping weights and a stabilizing controller. This algorithm captures the design

specifications listed above in a systematic manner while trying to maximize the robust stability margin of the closed-loop system. We fix the post-compensator weight to low pass filter on all channels and use the algorithm to optimize the pre-compensator weights for all channels.

The solution algorithm converged with a robust stability margin of 0.51. This level of robust stability margin indicates the tolerance of approximately 51% of coprime factor uncertainty. Figure 5.7 shows the singular value plots of the linearized plant, the shaped plant and the synthesized controller.

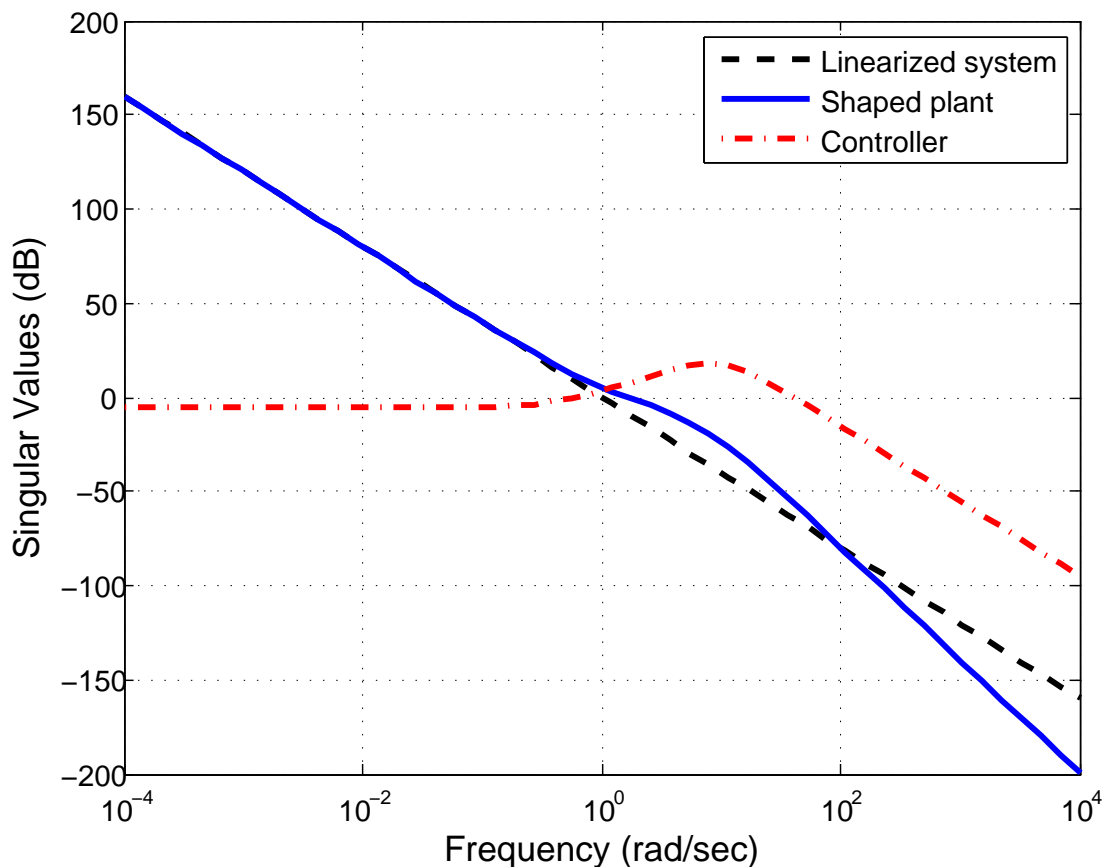


Figure 5.7: Singular values plots for the linearized system, the shaped system and the controller of the Tri-rotor UAV (no actuator dynamics).

To demonstrate the numerical results, we simulate the Tri-rotor UAV along with the design controller in Simulink. Figure 5.8 depicts the block diagram for the simulation where $\begin{bmatrix} \eta_r & \lambda_r \end{bmatrix}^T$ is the desired reference attitude and position respectively.

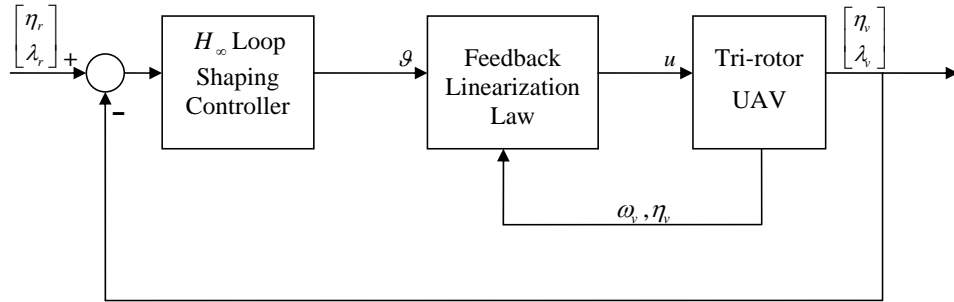


Figure 5.8: Simulation block diagram for the control design of the Tri-rotor UAV.

Figure 5.9 depicts the performance of the UAV for a scenario of horizontal hovering at height of 5 m where the vehicle was at a non-zero initial position and attitude as shown. The speed of the BLDC motors and the angles of the servo motors to stabilize the vehicle and track the references are shown in Figure 5.10. The controller shows good performance with tracking in all channels. The controller succeeds to maintain the stability of the vehicle and follow the reference trajectory for all initial conditions of the vehicle. The settling time of the system is about 3 s which is acceptable taking into considering the slow dynamics of the vehicle. The servos and BLDC motors are not saturated and operate within their physical limits of $\pm 90^\circ$ for the servos and 12000 rpm for the BLDC motors, where these limits come from the technical specifications of the real actuators used in the Tri-rotor UAV, see Section 5.5 for more details.

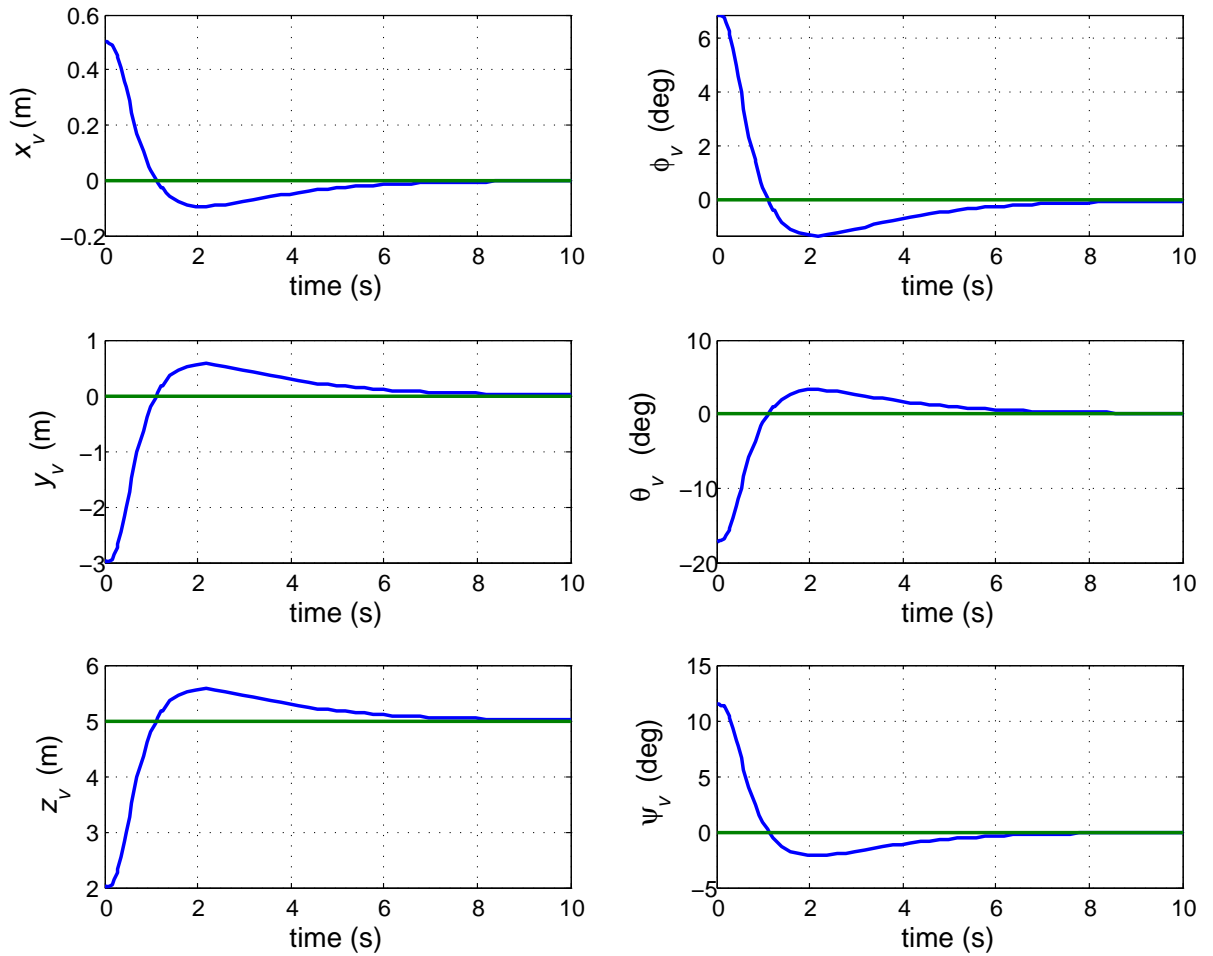


Figure 5.9: Simulation plots of the UAV position and attitude using the synthesized controller of \mathcal{H}_∞ loop shaping control associated with classical feedback linearisation. The specified reference input is $(0, 0, 0)$ deg for the attitude and $(0, 0, 5)$ m for the position in the earth frame. The UAV was in a non-zero initial position and attitude.

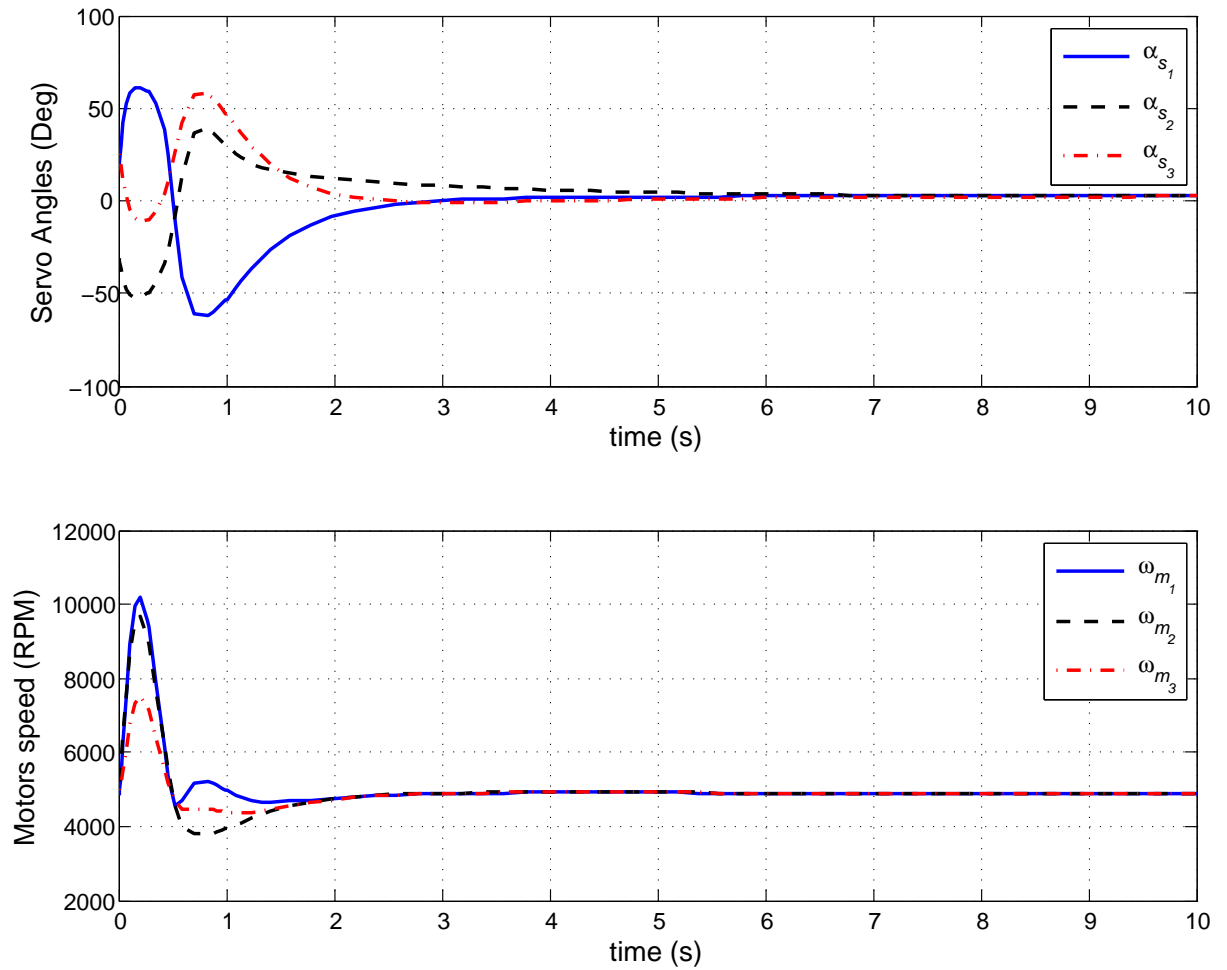


Figure 5.10: The performance of the actuators (servos and BLDC motors) to track the specified reference input of $(0,0,0)$ deg for the attitude, and $(0,0,5)$ m for the position. The servos and BLDC motors operate within their physical limits of $\pm 90^\circ$ for the servos and 12000 rpm for the BLDC motors.

5.4.2 Analysis of Unmodeled Actuator Dynamics Effect

In the previous section, the performance of the Tri-rotor UAV is simulated without actuator dynamics assuming that actuators are fast and their dynamics can be neglected. In this section we challenge this assumption by modeling the actuators of the UAV and investigate the effect of unmodeled actuator dynamics on the stability of the system.

The Tri-rotor UAV has two types of actuators, Brushless DC (BLDC) motors and digital Servos. Neglecting the inductance effect, the dynamic model of the BLDC motors can be represented as a first order system [37]. In addition, the servos combined with their drive circuits can be represented as first order systems using the supplied specifications of the servo response.

Assuming identical BLDC motors and identical servo motors, the dynamic equations of the i^{th} BLDC motor and the i^{th} servo are:

$$\dot{\omega}_{m_i} = c_m \omega_{m_i} + k_m V_{m_i}, \quad i = 1, 2, 3, \quad (5.86)$$

$$\dot{\alpha}_{s_i} = c_s \alpha_{s_i} + k_s V_{s_i}, \quad i = 1, 2, 3, \quad (5.87)$$

where c_m and c_s are the time constant for BLDC motor response and servo motor response respectively. k_m is the gain of the BLDC motor from the input voltage to the steady state speed of the shaft and k_s is the gain of the servo motor from the input voltage to the steady state tilting angle. V_{m_i} is the applied voltage to the i^{th} BLDC motor in form of Pulse Width Modulation (PWM) signal and V_{s_i} is the applied voltage to the i^{th} servo motor in form of Pulse Width Modulation (PWM) signal. c_s and k_s are given from the specifications of the servo drive while c_m and k_m are obtained from the BLDC motors specifications as [37]:

$$c_m = -\frac{k_v^2 + B_m R_a}{I_m R_a} \quad (5.88)$$

$$k_m = \frac{k_v}{I_m R_a} \quad (5.89)$$

where I_m is the inertia for the rotor, R_a is the armature resistance, B_m is the viscous friction coefficient, k_v is the speed-to-voltage constant. All values are of the BLDC motor.

In matrix form, the equations of the three BLDC motors and the three servos can be written as:

$$\dot{\omega}_m = \mathbf{C}_m \omega_m + \mathbf{K}_m V_m \quad (5.90)$$

$$\dot{\alpha}_s = \mathbf{C}_s \alpha_s + \mathbf{K}_s V_s \quad (5.91)$$

where

$$\omega_m = \begin{bmatrix} \omega_{m1} \\ \omega_{m2} \\ \omega_{m3} \end{bmatrix}, \quad \alpha_s = \begin{bmatrix} \alpha_{s1} \\ \alpha_{s2} \\ \alpha_{s3} \end{bmatrix}, \quad V_m = \begin{bmatrix} V_{m1} \\ V_{m2} \\ V_{m3} \end{bmatrix}, \quad V_s = \begin{bmatrix} V_{s1} \\ V_{s2} \\ V_{s3} \end{bmatrix} \quad (5.92)$$

and

$$\mathbf{C}_m = c_m \mathbf{I}_{3 \times 3}, \quad \mathbf{C}_s = c_s \mathbf{I}_{3 \times 3}, \quad \mathbf{K}_m = k_m \mathbf{I}_{3 \times 3}, \quad \mathbf{K}_s = k_s \mathbf{I}_{3 \times 3}. \quad (5.93)$$

with \mathbf{I} is the identity matrix of the specified size.

In compact form, the dynamics of the BLDC motors and the servo motors can be written by:

$$\dot{x}_a = \mathbf{A}_a x_a + \mathbf{B}_a u_a \quad (5.94)$$

where

$$x_a = \begin{bmatrix} \omega_m \\ \alpha_s \end{bmatrix}, \quad \mathbf{A}_a = \begin{bmatrix} \mathbf{C}_m & \mathbf{0} \\ \mathbf{0} & \mathbf{C}_s \end{bmatrix}, \quad \mathbf{B}_a = \begin{bmatrix} \mathbf{K}_m & \mathbf{0} \\ \mathbf{0} & \mathbf{K}_s \end{bmatrix}, \quad u_a = \begin{bmatrix} V_m \\ V_s \end{bmatrix}$$

To verify the models of the actuators of the Tri-rotor UAV, we consider physical hardware actuators. We choose the BLDC motor HC5030-390 manufactured by "Maxx Product" and the servo S9157 manufactured by "Futaba" as examples for the actuators of the Tri-rotor UAV. The dynamics of these actuators are excited using hardware in the loop experiment. The response of the actuators to pulse inputs are shown in Figure 5.11.

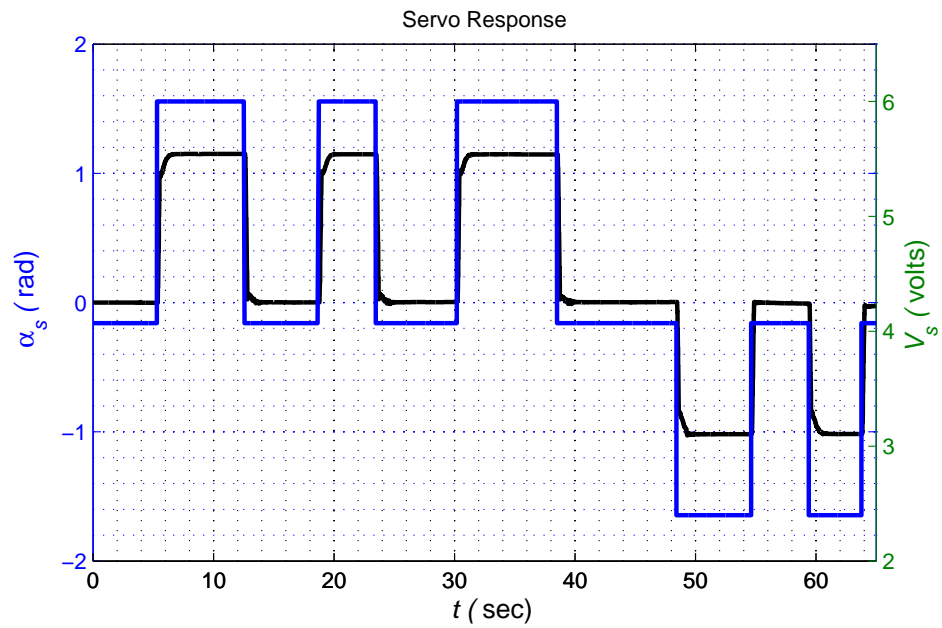
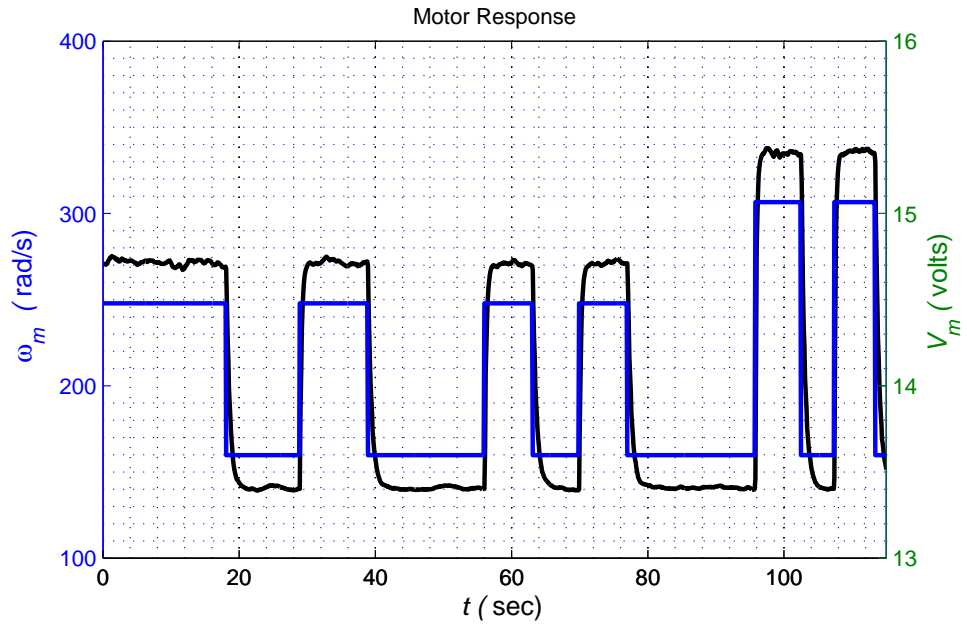


Figure 5.11: Response of the BLDC motor HC5030-390 and the digital servo S9157 used in the Tri-rotor UAV.

From this figure, we can see that the dynamic model of the BLDC motors and servos can be approximated by first order system as given in Equations (5.86) - (5.87).

In Section 5.4.1.4, a \mathcal{H}_∞ controller is synthesized and the performance of the Tri-rotor UAV is simulated while neglecting actuator dynamics. Aiming to verify the effect of

unmodeled actuator dynamics on input-output feedback linearisation, we impose here the actuator dynamics and use the same controller designed before to test the stability of the system and show the effect of unmodeled actuator dynamics. The effect of the unmodeled actuators dynamics on the performance of the UAV is reflected in Figure 5.12 with actuators behaviour shown in Figure 5.13.

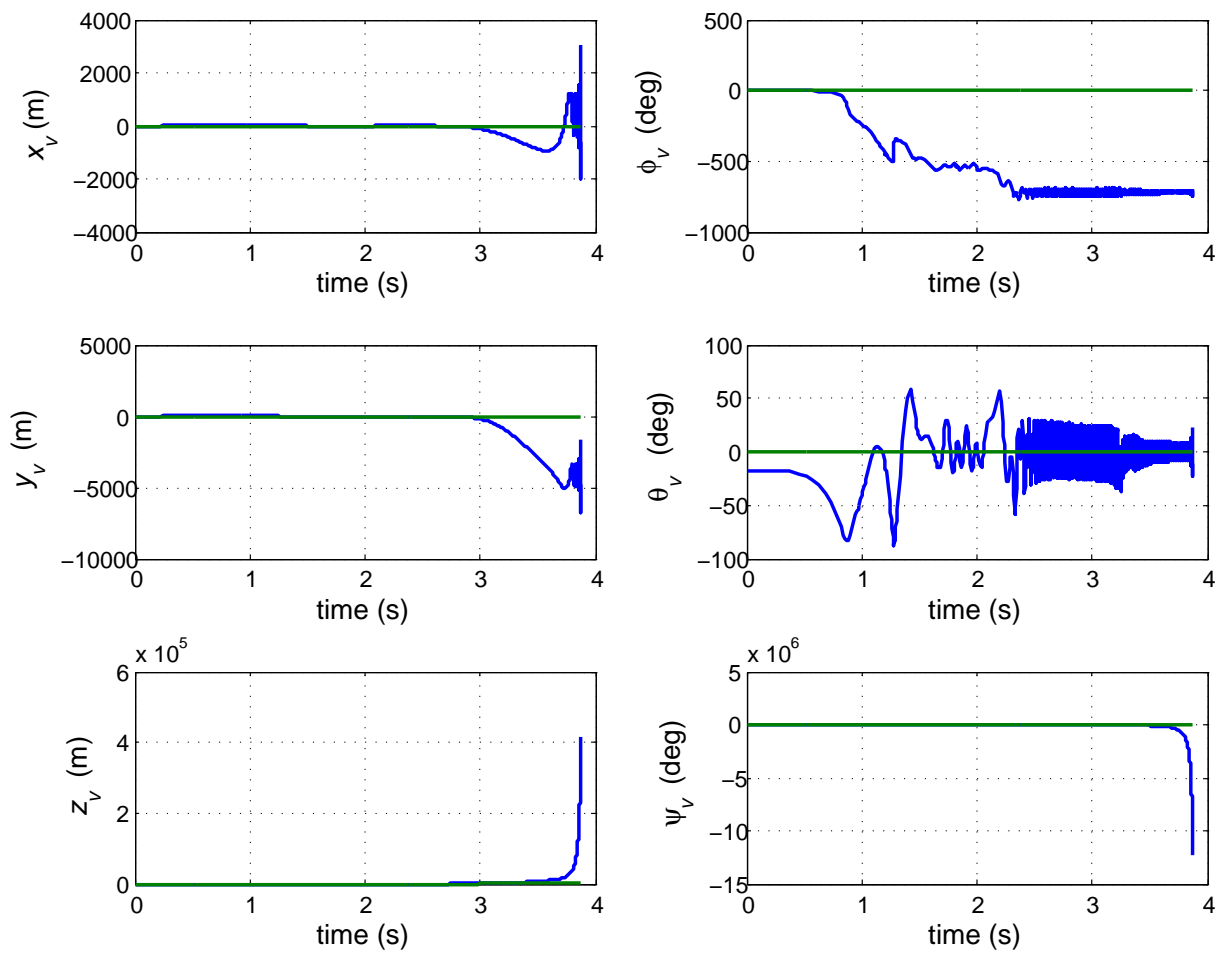


Figure 5.12: Simulation plots of the UAV position and attitude to demonstrate the effect of the unmodeled actuator dynamics.

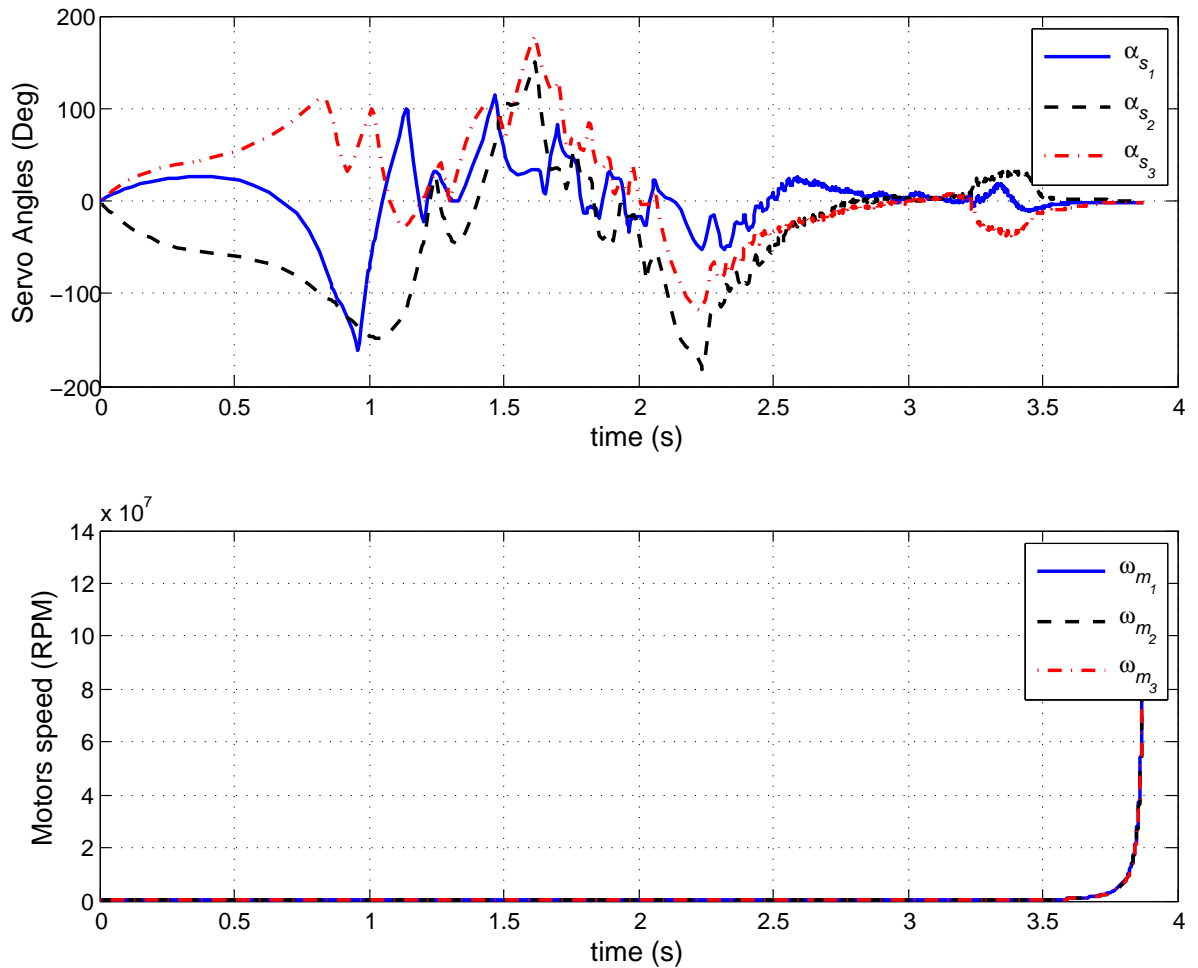


Figure 5.13: The performance of the actuators for the unstable UAV due to the impact of unmodeled actuator dynamics.

Figures 5.12 and 5.13 show clearly that unmodeled actuator dynamics destabilize the UAV system. This observation matches the result derived before in Chapter 2. The handling of actuator dynamics will be investigated in details in next section.

5.4.3 Control System Design Including Actuators Dynamics: Comparison Study

The previous section shows the destabilizing effect of unmodeled actuator dynamics on the Tri-rotor UAV system. In this section, we include actuator dynamics and implement the two stage feedback linearisation technique developed in Chapter 2 to linearize the UAV nonlinear model and compensate actuator dynamics. For comparison study we also implement classical feedback linearisation for the full system including actuator dynamics. The comparison aims to clarify the benefits of the proposed two stage feedback linearisation. We start first by implementing feedback linearisation on the total system and then we use the proposed two stage feedback linearisation.

5.4.3.1 Case 1: Complete Model Classical Feedback Linearisation

Full System Feedback Linearisation

The complete model of the Tri-rotor UAV including actuator dynamics is:

$$\dot{v} = gH_g - \mathcal{S}(\omega)v + \frac{k_f}{M_{tot}}\mathbf{H}_f\rho \quad (5.95)$$

$$\dot{\omega} = -\mathbf{I}^{-1}\mathcal{S}(\omega)\mathbf{I}\omega + \mathbf{I}^{-1}(k_f\mathbf{H}_t - k_t\mathbf{H}_f)\rho \quad (5.96)$$

$$\dot{\eta} = \Psi\omega \quad (5.97)$$

$$\dot{\lambda} = \mathbf{R}_b^e v \quad (5.98)$$

$$\dot{x}_a = \mathbf{A}_a x_a + \mathbf{B}_a u_a \quad (5.99)$$

$$y_a = x_a \quad (5.100)$$

The input to the system is u_a and we have the output as:

$$y = \begin{bmatrix} \eta \\ \lambda \end{bmatrix} \quad (5.101)$$

To implement input-output feedback linearisation, we have:

$$\dot{y} = y^{(1)} = \begin{bmatrix} \dot{\eta} \\ \dot{\lambda} \end{bmatrix} = \begin{bmatrix} \mathbf{\Psi}\omega \\ \mathbf{R}_b^e v \end{bmatrix} \quad (5.102)$$

and

$$\ddot{y} = y^{(2)} = \begin{bmatrix} \ddot{y}_1 \\ \ddot{y}_2 \end{bmatrix} = \begin{bmatrix} \mathbf{\Psi}\omega + \mathbf{\Psi}\dot{\omega} \\ (\mathbf{R}_b^e)\dot{v} + \mathbf{R}_b^e \ddot{v} \end{bmatrix} \quad (5.103)$$

We continue to get:

$$y^{(3)} = \begin{bmatrix} \mathbf{\Psi}\ddot{\omega} + 2\mathbf{\Psi}\dot{\omega} + \mathbf{\Psi}\ddot{\omega} \\ (\mathbf{R}_b^e)\ddot{v} + 2\mathbf{R}_b^e \dot{v} + \mathbf{R}_b^e \ddot{v} \end{bmatrix} \quad (5.104)$$

$$= \begin{bmatrix} \mathbf{\Psi}\omega + 2\mathbf{\Psi}I^{-1}(-\mathbf{S}(\omega)I\omega + (k_f\mathbf{H}_t - k_t\mathbf{H}_f)\rho) \\ + \mathbf{\Psi}I^{-1}[-(\mathbf{S}(\dot{\omega})I\omega + \mathbf{S}(\omega)I\dot{\omega}) + (k_f\mathbf{H}_t - k_t\mathbf{H}_f)\dot{\rho}] \\ (\mathbf{R}_b^e)\dot{v} + 2(\mathbf{R}_b^e)\dot{v} + \mathbf{R}_b^e \left(g\dot{H}_g - (\mathbf{S}(\dot{\omega})v + \mathbf{S}(\omega)\dot{v}) + \frac{k_f}{M_{tot}}\mathbf{H}_f\dot{\rho} \right) \end{bmatrix} \quad (5.105)$$

We have:

$$\dot{\rho} = \begin{bmatrix} 2\omega_{m_1}\dot{\omega}_{m_1}\sin(\alpha_{s_1}) + \omega_{m_1}^2\cos(\alpha_{s_1})\dot{\alpha}_{s_1} \\ 2\omega_{m_2}\dot{\omega}_{m_2}\sin(\alpha_{s_2}) + \omega_{m_2}^2\cos(\alpha_{s_2})\dot{\alpha}_{s_2} \\ 2\omega_{m_3}\dot{\omega}_{m_3}\sin(\alpha_{s_3}) + \omega_{m_3}^2\cos(\alpha_{s_3})\dot{\alpha}_{s_3} \\ 2\omega_{m_1}\dot{\omega}_{m_1}\cos(\alpha_{s_1}) - \omega_{m_1}^2\sin(\alpha_{s_1})\dot{\alpha}_{s_1} \\ 2\omega_{m_2}\dot{\omega}_{m_2}\cos(\alpha_{s_2}) - \omega_{m_2}^2\sin(\alpha_{s_2})\dot{\alpha}_{s_2} \\ 2\omega_{m_3}\dot{\omega}_{m_3}\cos(\alpha_{s_3}) - \omega_{m_3}^2\sin(\alpha_{s_3})\dot{\alpha}_{s_3} \end{bmatrix} \quad (5.106)$$

$$= \mathbf{N}\dot{x}_a \quad (5.107)$$

$$= \mathbf{N}(\mathbf{A}_a x_a + \mathbf{B}_a u_a) \quad (5.108)$$

where

$$\mathbf{N} = \begin{bmatrix} 2\omega_{m_1} \sin \alpha_{s_1} & 0 & 0 & \omega_{m_1}^2 \cos \alpha_{s_1} & 0 & 0 \\ 0 & 2\omega_{m_2} \sin \alpha_{s_2} & 0 & 0 & \omega_{m_2}^2 \cos \alpha_{s_2} & 0 \\ 0 & 0 & 2\omega_{m_3} \sin \alpha_{s_3} & 0 & 0 & \omega_{m_3}^2 \cos \alpha_{s_3} \\ 2\omega_{m_1} \cos \alpha_{s_1} & 0 & 0 & -\omega_{m_1}^2 \sin \alpha_{s_1} & 0 & 0 \\ 0 & 2\omega_{m_2} \cos \alpha_{s_2} & 0 & 0 & -\omega_{m_2}^2 \sin \alpha_{s_2} & 0 \\ 0 & 0 & 2\omega_{m_3} \cos \alpha_{s_3} & 0 & 0 & -\omega_{m_3}^2 \sin \alpha_{s_3} \end{bmatrix} \quad (5.109)$$

From the properties of the rotation matrix we have:

$$\ddot{\mathbf{R}}_b^e = \frac{d(\dot{\mathbf{R}}_b^e)}{dt} \quad (5.110)$$

$$= \frac{d(\mathbf{R}_b^e \mathbf{S}(\omega^b))}{dt} \quad (5.111)$$

$$= \mathbf{R}_b^e \left(\mathbf{S}(\omega^b) \mathbf{S}(\dot{\omega}^b) + \mathbf{S}(\dot{\omega}^b) \right) \quad (5.112)$$

and therefore, we can write:

$$\begin{aligned}
y^{(3)} &= \left[\begin{array}{l} \ddot{\Psi}\omega + 2\dot{\Psi}I^{-1}(-\mathbf{S}(\omega)\mathbf{I}\omega + (k_f\mathbf{H}_t - k_t\mathbf{H}_f)\rho) + \\ \Psi I^{-1}(-(\mathbf{S}(\dot{\omega})\mathbf{I}\omega + \mathbf{S}(\omega)\mathbf{I}\dot{\omega}) + (k_f\mathbf{H}_t - k_t\mathbf{H}_f)\mathbf{N}(\mathbf{A}_a x_a + \mathbf{B}_a u_a)) \\ \mathbf{R}_b^e(\mathbf{S}(\omega)\mathbf{S}(\omega) + \mathbf{S}(\dot{\omega}))v + 2\mathbf{R}_b^e\mathbf{S}(\omega)\dot{v} - \mathbf{R}_b^e\mathbf{S}(\dot{\omega})v - \mathbf{R}_b^e\mathbf{S}(\omega)\dot{v} + \\ \mathbf{R}_b^e g\dot{H}_g + \frac{k_f}{M_{tot}}\mathbf{R}_b^e\mathbf{H}_f\mathbf{N}(\mathbf{A}_a x_a + \mathbf{B}_a u_a) \end{array} \right] \\
&= \left[\begin{array}{l} (\ddot{\Psi} - 2\dot{\Psi}I^{-1}\mathbf{S}(\omega)\mathbf{I} - \Psi I^{-1}\mathbf{S}(\dot{\omega})\mathbf{I} + \Psi I^{-1}\mathbf{S}(\omega)\mathbf{S}(\omega)\mathbf{I})\omega + 2\dot{\Psi}I^{-1}(k_f\mathbf{H}_t - k_t\mathbf{H}_f)\rho + \\ -\Psi I^{-1}\mathbf{S}(\omega)(k_f\mathbf{H}_t - k_t\mathbf{H}_f)\rho + \Psi I^{-1}(k_f\mathbf{H}_t - k_t\mathbf{H}_f)\mathbf{N}(\mathbf{A}_a x_a + \mathbf{B}_a u_a) \\ \mathbf{R}_b^e\mathbf{S}(\omega)\mathbf{S}(\omega)v + \mathbf{R}_b^e\mathbf{S}(\omega)\left(gH_g - \mathbf{S}(\omega)v + \frac{k_f}{M_{tot}}\mathbf{H}_f\rho\right) + \\ \mathbf{R}_b^e\left(g\dot{H}_g + \frac{k_f}{M_{tot}}\mathbf{H}_f\mathbf{N}(\mathbf{A}_a x_a + \mathbf{B}_a u_a)\right) \end{array} \right] \\
&= \left[\begin{array}{l} 2\dot{\Psi}I^{-1}(k_f\mathbf{H}_t - k_t\mathbf{H}_f) - \Psi I^{-1}\mathbf{S}(\omega)(k_f\mathbf{H}_t - k_t\mathbf{H}_f) \\ \frac{k_f}{M_{tot}}\mathbf{R}_b^e\mathbf{S}(\omega)\mathbf{H}_f \end{array} \right] \rho + \\
&\left[\begin{array}{l} (\ddot{\Psi} - 2\dot{\Psi}I^{-1}\mathbf{S}(\omega)\mathbf{I} - \Psi I^{-1}\mathbf{S}(\dot{\omega})\mathbf{I} + \Psi I^{-1}\mathbf{S}(\omega)\mathbf{S}(\omega)\mathbf{I})\omega \\ g\mathbf{R}_b^e\mathbf{S}(\omega)H_g + g\mathbf{R}_b^e\dot{H}_g \end{array} \right] + \\
&\left[\begin{array}{l} \Psi I^{-1}(k_f\mathbf{H}_t - k_t\mathbf{H}_f) \\ \frac{k_f}{M_{tot}}\mathbf{R}_b^e\mathbf{H}_f \end{array} \right] \mathbf{N}\mathbf{A}_a x_a + \\
&\left[\begin{array}{l} \Psi I^{-1}(k_f\mathbf{H}_t - k_t\mathbf{H}_f) \\ \frac{k_f}{M_{tot}}\mathbf{R}_b^e\mathbf{H}_f \end{array} \right] \mathbf{N}\mathbf{B}_a u_a \tag{5.113}
\end{aligned}$$

We have:

$$\dot{\omega} \times (\mathbf{I}\omega) = -(\mathbf{I}\omega) \times \dot{\omega} \tag{5.114}$$

$$\Leftrightarrow \mathbf{S}(\dot{\omega})\mathbf{I}\omega = -\mathbf{S}(\mathbf{I}\omega)\dot{\omega} \tag{5.115}$$

For the gravitational force, we have:

$$H_g = \begin{bmatrix} \sin(\theta_v) \\ -\sin(\phi_v)\cos(\theta_v) \\ -\cos(\phi_v)\cos(\theta_v) \end{bmatrix} \tag{5.116}$$

and therefore:

$$\dot{H}_g = \mathbf{H}_{dg} \begin{bmatrix} \dot{\theta}_v \\ \dot{\phi}_v \\ \dot{\psi}_v \end{bmatrix} \quad (5.117)$$

$$= \mathbf{H}_{dg} \boldsymbol{\Psi} \omega_v \quad (5.118)$$

where

$$\mathbf{H}_{dg} = \begin{bmatrix} \cos(\theta_v) & 0 & 0 \\ \sin(\theta_v) \sin(\theta_v) & -\cos(\phi_v) \cos(\theta_v) & 0 \\ \cos(\theta_v) \sin(\theta_v) & \sin(\phi_v) \cos(\theta_v) & 0 \end{bmatrix} \quad (5.119)$$

From Equations (5.115) and (5.118), we can write:

$$y^{(3)} = \begin{bmatrix} (2\boldsymbol{\Psi}\mathbf{I}^{-1} - \boldsymbol{\Psi}\mathbf{I}^{-1}\mathbf{S}(\omega) + \boldsymbol{\Psi}\mathbf{I}^{-1}\mathbf{S}(\mathbf{I}\omega)\mathbf{I}^{-1}) (k_f\mathbf{H}_t - k_t\mathbf{H}_f) \\ \frac{k_f}{M_{tot}} \mathbf{R}_b^e \mathbf{S}(\omega) \mathbf{H}_f \end{bmatrix} \rho + \begin{bmatrix} (\ddot{\Psi} - 2\boldsymbol{\Psi}\mathbf{I}^{-1}\mathbf{S}(\omega)\mathbf{I} - \boldsymbol{\Psi}\mathbf{I}^{-1}\mathbf{S}(\mathbf{I}\omega)\mathbf{I}^{-1}\mathbf{S}(\omega)\mathbf{I} + \boldsymbol{\Psi}\mathbf{I}^{-1}\mathbf{S}(\omega)\mathbf{S}(\omega)\mathbf{I}) \omega \\ g\mathbf{R}_b^e \mathbf{S}(\omega) \mathbf{H}_g + g\mathbf{R}_b^e \mathbf{H}_{dg} \boldsymbol{\Psi} \omega \end{bmatrix} + \begin{bmatrix} \boldsymbol{\Psi}\mathbf{I}^{-1} (k_f\mathbf{H}_t - k_t\mathbf{H}_f) \\ \frac{k_f}{M_{tot}} \mathbf{R}_b^e \mathbf{H}_f \end{bmatrix} \mathbf{N} \mathbf{A}_a x_a + \begin{bmatrix} \boldsymbol{\Psi}\mathbf{I}^{-1} (k_f\mathbf{H}_t - k_t\mathbf{H}_f) \\ \frac{k_f}{M_{tot}} \mathbf{R}_b^e \mathbf{H}_f \end{bmatrix} \mathbf{N} \mathbf{B}_a u_a \quad (5.120)$$

Where:

$$\boldsymbol{\Psi} = \frac{\partial \Psi}{\partial \phi_v} \dot{\phi}_v + \frac{\partial \Psi}{\partial \theta_v} \dot{\theta}_v \quad (5.121)$$

and

$$\ddot{\boldsymbol{\Psi}} = \left(\frac{\partial \left(\frac{\partial \Psi}{\partial \phi_v} \right)}{\partial \phi_v} + \frac{\partial \Psi}{\partial \phi_v} \right) \ddot{\phi}_v + \left(\frac{\partial \left(\frac{\partial \Psi}{\partial \theta_v} \right)}{\partial \theta_v} + \frac{\partial \Psi}{\partial \theta_v} \right) \ddot{\theta}_v + \left(\frac{\partial \left(\frac{\partial \Psi}{\partial \phi_v} \right)}{\partial \theta_v} + \frac{\partial \left(\frac{\partial \Psi}{\partial \theta_v} \right)}{\partial \phi_v} \right) \dot{\phi}_v \dot{\theta}_v \quad (5.122)$$

$\dot{\theta}_v$, $\dot{\phi}_v$, $\ddot{\theta}_v$ and $\ddot{\phi}_v$ can be obtained respectively from Eq. (5.97) as:

$$\dot{\eta} = \begin{bmatrix} \dot{\phi}_v \\ \dot{\theta}_v \\ \dot{\psi}_v \end{bmatrix} = \mathbf{\Psi} \omega_v$$

and

$$\ddot{\eta} = \begin{bmatrix} \ddot{\phi}_v \\ \ddot{\theta}_v \\ \ddot{\psi}_v \end{bmatrix} = \dot{\mathbf{\Psi}} \omega_v + \mathbf{\Psi} \dot{\omega}_v$$

Now, we define the decoupling matrix as:

$$\boldsymbol{\beta}_f = \begin{bmatrix} \mathbf{\Psi} \mathbf{I}^{-1} (k_f \mathbf{H}_t - k_t \mathbf{H}_f) \\ \frac{k_f}{M_{tot}} \mathbf{R}_b^e \mathbf{H}_f \end{bmatrix} \mathbf{N} \mathbf{B}_a \quad (5.123)$$

We have:

$$\det[\boldsymbol{\beta}_f] = -k_d \omega_{m_1}^3 \omega_{m_2}^3 \omega_{m_3}^3 / \cos(\theta_v) \quad (5.124)$$

where $k_d = f(M_{tot}, k_f, k_t, I_{xx}, I_{yy}, I_{zz}) > 0$.

Therefore, $\det[\boldsymbol{\beta}_f] = 0$ only² when $\omega_{m_i} = 0$, $i = 1, 2, 3$. This means the inverse $\boldsymbol{\beta}_f^{-1}$ exists always in the region $\mathbb{D}_0 = \{x_f \in \mathbb{R}^{18} | \omega_m = 0\}$ where x_f represents the states of the full system including actuator dynamics as:

$$x = \begin{bmatrix} v_v \\ \omega_v \\ \eta \\ \lambda \\ \omega_m \\ \alpha_s \end{bmatrix}$$

This means that $\boldsymbol{\beta}_f$ is invertible and the feedback linearisation exist always as long as the BLDC motors are switched on. Therefore, the motors should be switched on and runs at

²It is always assumed that $-\pi/2 < \theta_v < \pi/2$.

low speed before the controller takes any action to avoid any mathematical error during the initial start of the vehicle.

We choose a new control input $\vartheta_f = \begin{bmatrix} \vartheta_{f1} \\ \vartheta_{f2} \end{bmatrix}$ such as each input is a vector of three components, and we write our desired linearized dynamics as:

$$y^{(3)} = \vartheta_f \quad (5.125)$$

Now from Eq. (5.113) we can write the feedback linearisation law as

$$u_a = \boldsymbol{\beta}_f^{-1} (\vartheta_f - \mathbf{C}_1 \rho - \mathbf{C}_2) \quad (5.126)$$

where

$$\mathbf{C}_1 = \begin{bmatrix} (2\Psi\mathbf{I}^{-1} - \Psi\mathbf{I}^{-1}\mathbf{S}(\omega) + \Psi\mathbf{I}^{-1}\mathbf{S}(\mathbf{I}\omega)\mathbf{I}^{-1}) (k_f\mathbf{H}_t - k_t\mathbf{H}_f) \\ \frac{k_f}{M_{tot}} \mathbf{R}_b^e \mathbf{S}(\omega) \mathbf{H}_f \end{bmatrix} \quad (5.127)$$

$$\mathbf{C}_2 = \begin{bmatrix} (\ddot{\Psi} - 2\dot{\Psi}\mathbf{I}^{-1}\mathbf{S}(\omega)\mathbf{I} - \Psi\mathbf{I}^{-1}\mathbf{S}(\mathbf{I}\omega)\mathbf{I}^{-1}\mathbf{S}(\omega)\mathbf{I} + \Psi\mathbf{I}^{-1}\mathbf{S}(\omega)\mathbf{S}(\omega)\mathbf{I}) \omega \\ g\mathbf{R}_b^e \mathbf{S}(\omega) \mathbf{H}_g + g\mathbf{R}_b^e \mathbf{H}_{dg} \Psi \omega \end{bmatrix} + \begin{bmatrix} \Psi\mathbf{I}^{-1} (k_f\mathbf{H}_t - k_t\mathbf{H}_f) \\ \frac{k_f}{M_{tot}} \mathbf{R}_b^e \mathbf{H}_f \end{bmatrix} \mathbf{N} \mathbf{A}_a x_a \quad (5.128)$$

The full linearized system is given as:

$$\dot{\zeta}_f = \begin{bmatrix} 0 & 1 & 0 & 0 & 0 & 0 \\ 0 & 0 & 1 & 0 & 0 & 0 \\ 0 & 0 & 0 & 0 & 0 & 0 \\ 0 & 0 & 0 & 0 & 1 & 0 \\ 0 & 0 & 0 & 0 & 0 & 1 \\ 0 & 0 & 0 & 0 & 0 & 0 \end{bmatrix} \zeta_f + \begin{bmatrix} 0 & 0 \\ 0 & 0 \\ 1 & 0 \\ 0 & 0 \\ 0 & 0 \\ 0 & 1 \end{bmatrix} \vartheta_f \quad (5.129)$$

$$y = \begin{bmatrix} 1 & 0 & 0 & 0 & 0 & 0 \\ 0 & 0 & 0 & 1 & 0 & 0 \end{bmatrix} \zeta_f \quad (5.130)$$

where

$$\zeta_f = \begin{bmatrix} \eta \\ \dot{\eta} \\ \ddot{\eta} \\ \lambda \\ \dot{\lambda} \\ \ddot{\lambda} \end{bmatrix}, y = \begin{bmatrix} \eta \\ \lambda \end{bmatrix}, \vartheta_f = \begin{bmatrix} \vartheta_{f_1} \\ \vartheta_{f_2} \end{bmatrix}$$

The linearized system is a chain of triple integrators for the rotational motion and the translational motion.

Control Synthesis and Simulation Results

We invoke now the \mathcal{H}_∞ LSDP to synthesize a controller for the full linearized system. We consider the same design specifications mentioned in Section 5.4.1.4 for the loop design and we use the algorithm in [117] utilized previously to optimize the shaping wight and simultaneously synthesize a controller for the system. The solution algorithm converged with a robust stability margin of 0.37. This level of robust stability margin indicates the tolerance of approximately 37 % of coprime factor uncertainty. Figure 5.14 shows the singular value plots of the full linearized plant, the shaped plant and the synthesized controller.

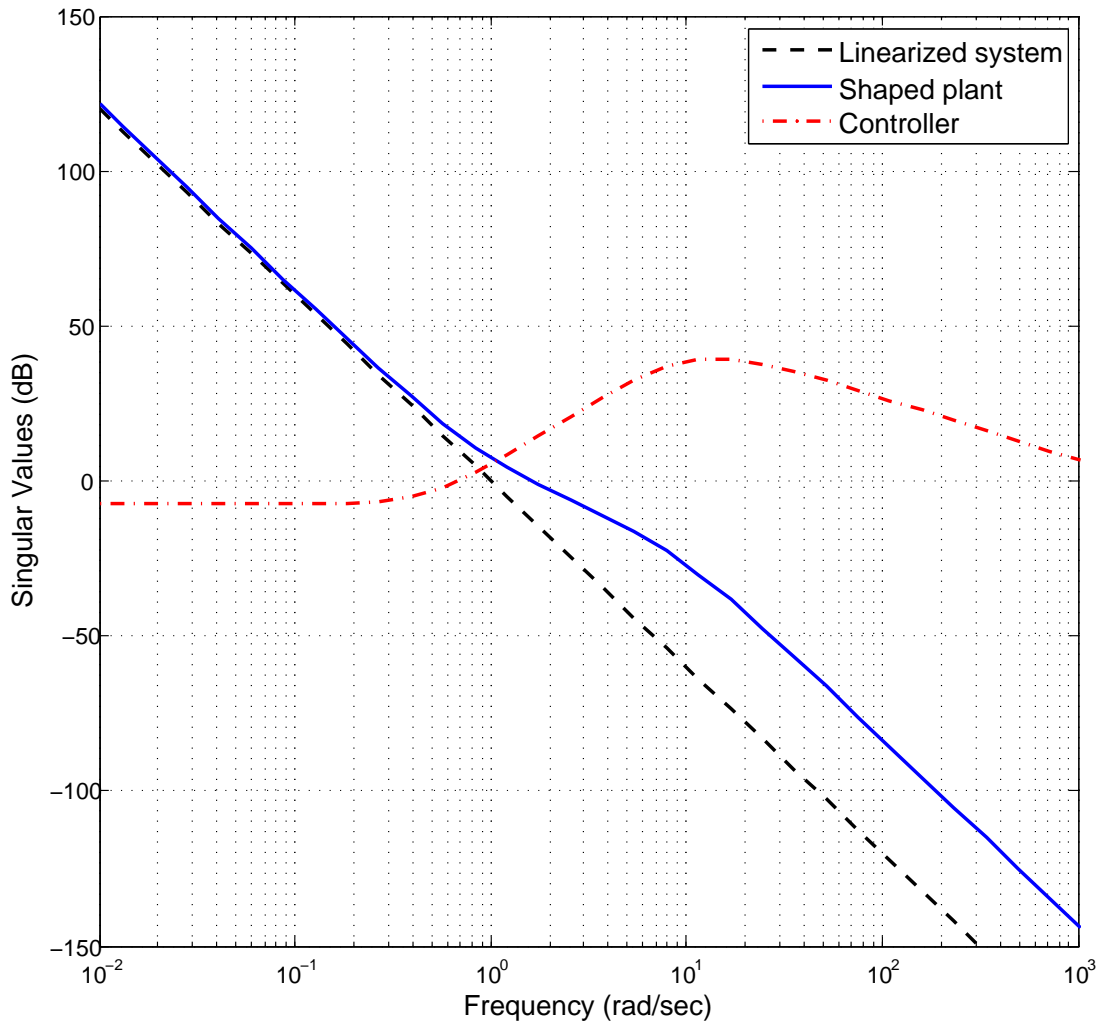


Figure 5.14: Singular values plots for the linearized system, the shaped system and the controller of the full modeled system including actuator dynamics.

The simulation results of the UAV performance and the actuators are shown in Figures 5.15 and 5.16. For comparison with the case of unmodeled actuator dynamics, we choose the same flight scenario in this simulation. Figure 5.15 depicts the performance of the UAV for a scenario of horizontal hovering at 5 m height where the vehicle was at initial non-zero position and attitude as shown. The speed of the BLDC motors and the angles of the servo motors to stabilize the vehicle and track the references are shown in Figure 5.16. The reader can observe that the inclusion of actuator dynamics causes some delay as expected and the system takes longer time to reach the steady state value.

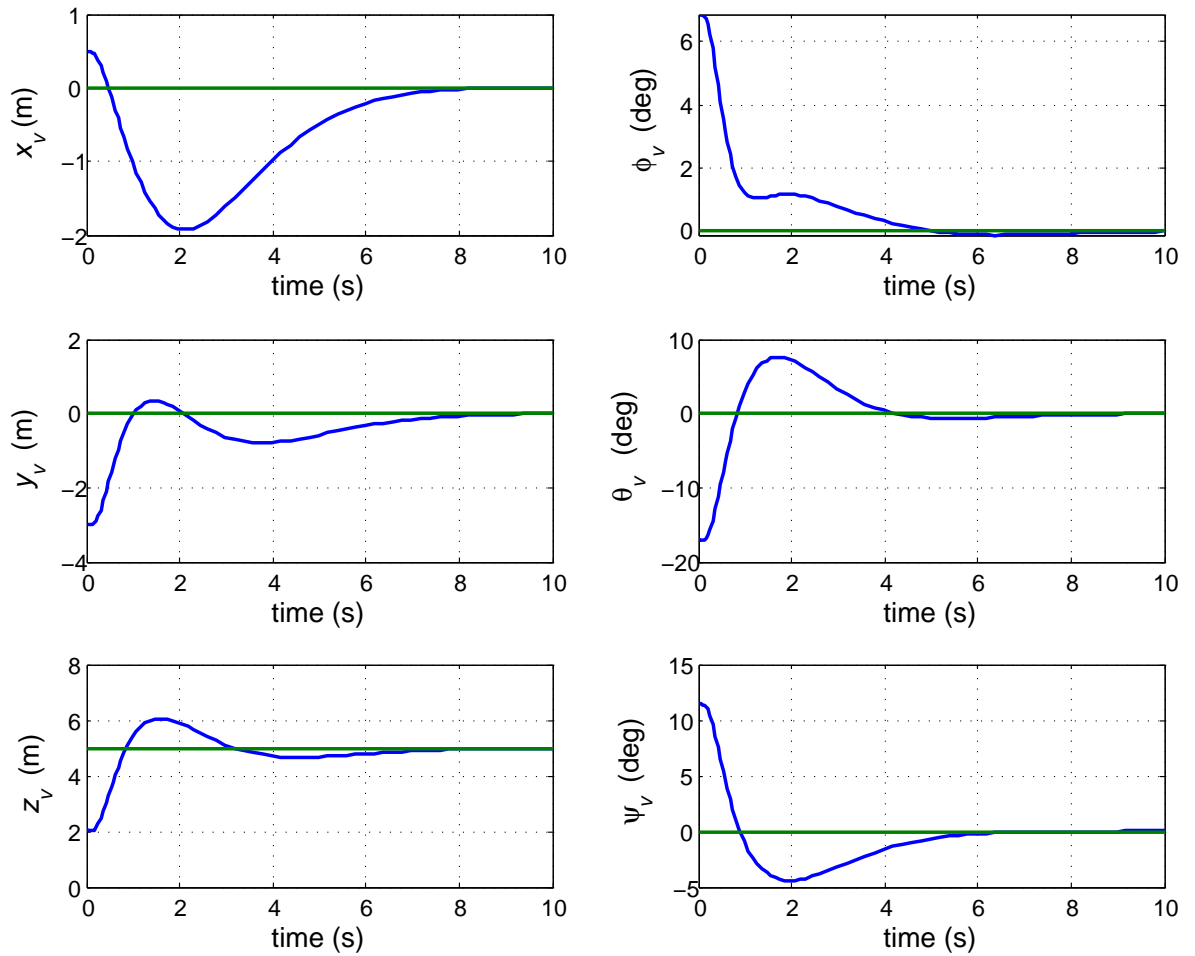


Figure 5.15: Simulation plots of the UAV position and attitude using the synthesized controller of \mathcal{H}_∞ loop shaping control associated with classical feedback linearisation of full modeling including actuator dynamics. The specified reference input is $(0, 0, 0)$ deg for the attitude and $(0, 0, 5)$ m for the position in the earth frame. The UAV was in a non-zero initial position and attitude.

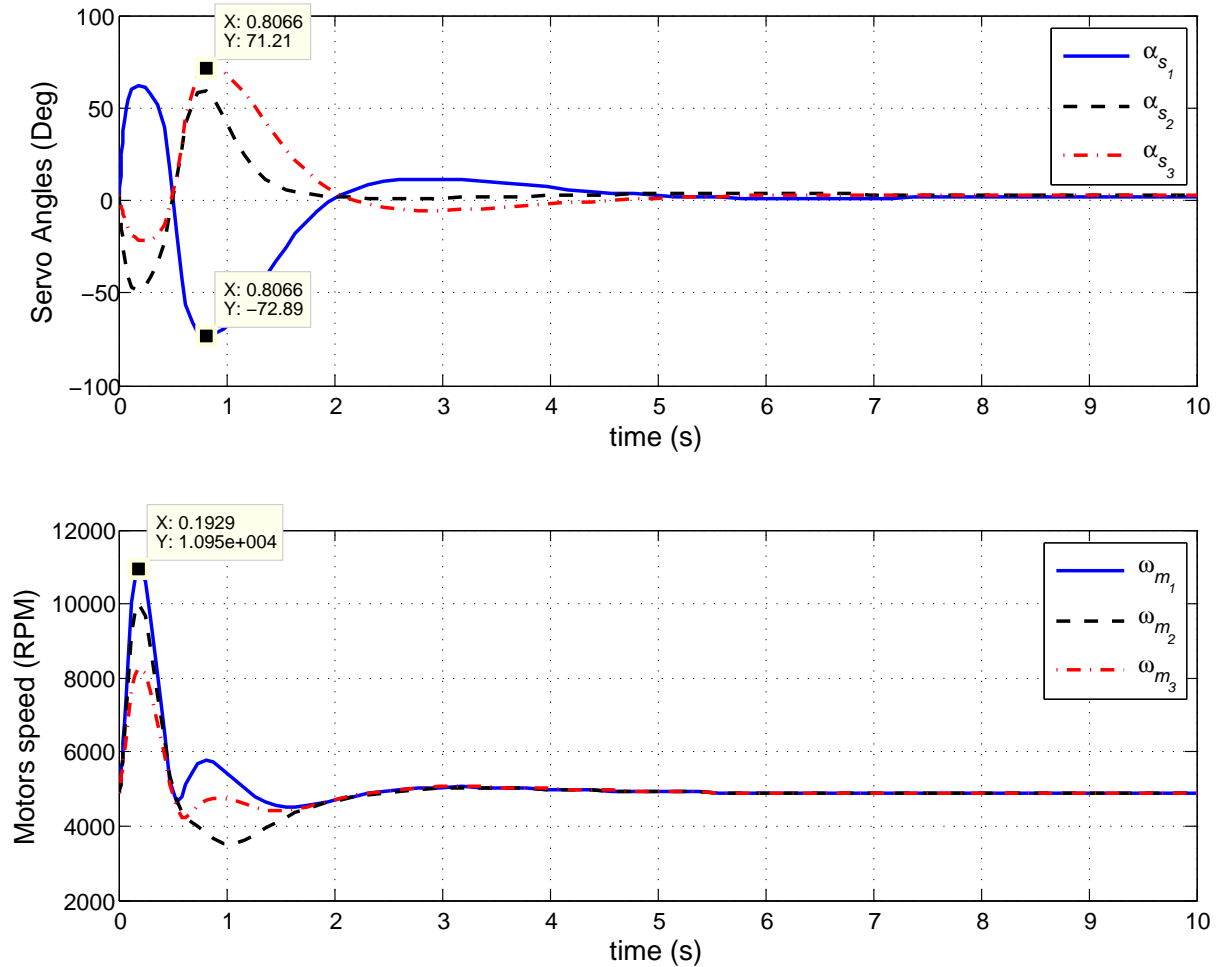


Figure 5.16: The performance of the actuators (servos and BLDC motors) to track the specified reference input of $(0, 0, 0)$ deg for the attitude, and $(0, 0, 5)$ m for the position in case of feedback linearisation of the full system including actuator dynamics. The servos and BLDC motors operate within their physical limits of $\pm 90^\circ$ for the servos and 12000 rpm for the BLDC motors.

5.4.3.2 Case 2: Two Stage Linearisation and Control

In this section we consider the two stage feedback linearisation technique developed in Chapter 2 to design a \mathcal{H}_∞ controller for the system including actuator dynamics.

Two Stage Feedback Linearisation

To implement the two stage input-output feedback linearisation, we firstly compensate for the dynamics of the actuators. The actuators system is a linear decoupled system so there is no need for a linearisation or a decoupling process. To compensate for the dynamics of the actuators, we define the error system as:

$$e = y_a - y_d \quad (5.131)$$

where $y_a = x_a$, $y_d = u$ and u is the feedback linearisation law of the outer loop to be designed later. This means:

$$\dot{e} = \dot{y}_a - \dot{y}_d \quad (5.132)$$

$$= \mathbf{A}_a x_a + \mathbf{B}_a u_a - \dot{y}_d \quad (5.133)$$

We choose the Lyapunov function:

$$V = \frac{1}{2} e^2 \quad (5.134)$$

whose derivative is:

$$\dot{V} = e \dot{e} \quad (5.135)$$

$$= e(\mathbf{A}_a x_a + \mathbf{B}_a u_a - \dot{y}_d) \quad (5.136)$$

To achieve global asymptotic stability of the origin, we design the control law:

$$u_a = \mathbf{B}_a^{-1} [\dot{y}_d - \mathbf{A}_a x_a - \mathbf{c}e] \quad (5.137)$$

$$= \mathbf{B}_a^{-1} [\dot{u} - \mathbf{A}_a x_a - \mathbf{c}(x_a - u)] \quad (5.138)$$

where \mathbf{c} is a diagonal design matrix.

To ensure wide bandwidth with quick convergence of y_a to y_d , we choose \mathbf{c} with high value elements. Typically $c_{ii} > 100, i = 1, 2, \dots, 6$ are sufficient for fast tracking and wide bandwidth.

We move now to the second stage where we linearize the UAV system without actuator dynamics. This stage includes the linearisation of the UAV system as described in Equations (5.67) - (5.70). The feedback linearisation process for this system is implemented before in Section 5.4.1.1. The reader can recall the feedback linearisation law from Eq. (5.83) as:

$$u = \boldsymbol{\beta}^{-1} \left(\vartheta - \begin{bmatrix} (\dot{\Psi} - \Psi \mathbf{I}^{-1} \mathbf{S}(\omega) \mathbf{I}) \omega \\ g \mathbf{R}_b^e \mathbf{H}_g \end{bmatrix} \right), \quad (5.139)$$

where $\boldsymbol{\beta}$ is defined in Eq. (5.81) as:

$$\boldsymbol{\beta}(x) = \begin{bmatrix} \Psi \mathbf{I}^{-1} (k_f \mathbf{H}_t - k_t \mathbf{H}_f) \\ \frac{k_f}{M_{tot}} \mathbf{R}_b^e \mathbf{H}_f \end{bmatrix}. \quad (5.140)$$

The resulting linearized system is a double integrator system described in (5.84) - (5.85) as:

$$\dot{\zeta} = \begin{bmatrix} 0 & 1 & 0 & 0 \\ 0 & 0 & 0 & 0 \\ 0 & 0 & 0 & 1 \\ 0 & 0 & 0 & 0 \end{bmatrix} \zeta + \begin{bmatrix} 0 & 0 \\ 1 & 0 \\ 0 & 0 \\ 0 & 1 \end{bmatrix} \vartheta \quad (5.141)$$

$$y = \begin{bmatrix} 1 & 0 & 0 & 0 \\ 0 & 0 & 1 & 0 \end{bmatrix} \zeta \quad (5.142)$$

where

$$\zeta = \begin{bmatrix} \eta \\ \dot{\eta} \\ \lambda \\ \dot{\lambda} \end{bmatrix} \in \mathbb{R}^{12}, \quad y = \begin{bmatrix} \eta \\ \lambda \end{bmatrix} \in \mathbb{R}^6, \quad \vartheta = \begin{bmatrix} \vartheta_1 \\ \vartheta_2 \end{bmatrix} \in \mathbb{R}^6.$$

Control Synthesis and Simulation Results

To demonstrate the system performance when using the two stage feedback linearisation, we implement the same control designed before when performing feedback linearisation without actuator dynamics, refer to the singular values plots in Figure 5.7. Figures 5.17 and 5.18 depict respectively the system performance and the actuator behaviour under the synthesized control.

Comparing the feedback linearisation law between the case of full system feedback linearisation as in Eq (5.126) and the case of two stage feedback linearisation law as in Eq. (5.139) sheds some light on the strength of the latter technique. The feedback linearisation law is simpler and requires less computational capacity and exists for all values of the system states. This means that the controller can work for all positions and attitudes³ of the vehicle and all speeds and angles of actuators. In contrary, the feedback linearisation law of the full system feedback linearisation law is complicated and requires high computational capacity and does not exist for all state values. When the BLDC motors are switched off, the decoupling matrix is singular and the controller cannot start from static state. Moreover, the linearized system in case of full system feedback linearisation is higher and it means higher order for the synthesized controller compared with linearized system of order 2 in case of two stage feedback linearisation. The difference of the linearized system order between the two cases is not of great importance in this case because the actuator system is a first order system, but in case of higher order actuator systems, the difference between the order of the linearized systems has more impact on the order of the synthesized controller. From the comparison between Figure 5.17 and Figure 5.15, the reader can notice also that the system reaches the steady value faster when using the two stage feedback linearisation. This is due to the compensation and control of actuator dynamics in the two stage feedback linearisation.

³It is always assumed that $\pi/2 < \theta_v < \pi/2$.

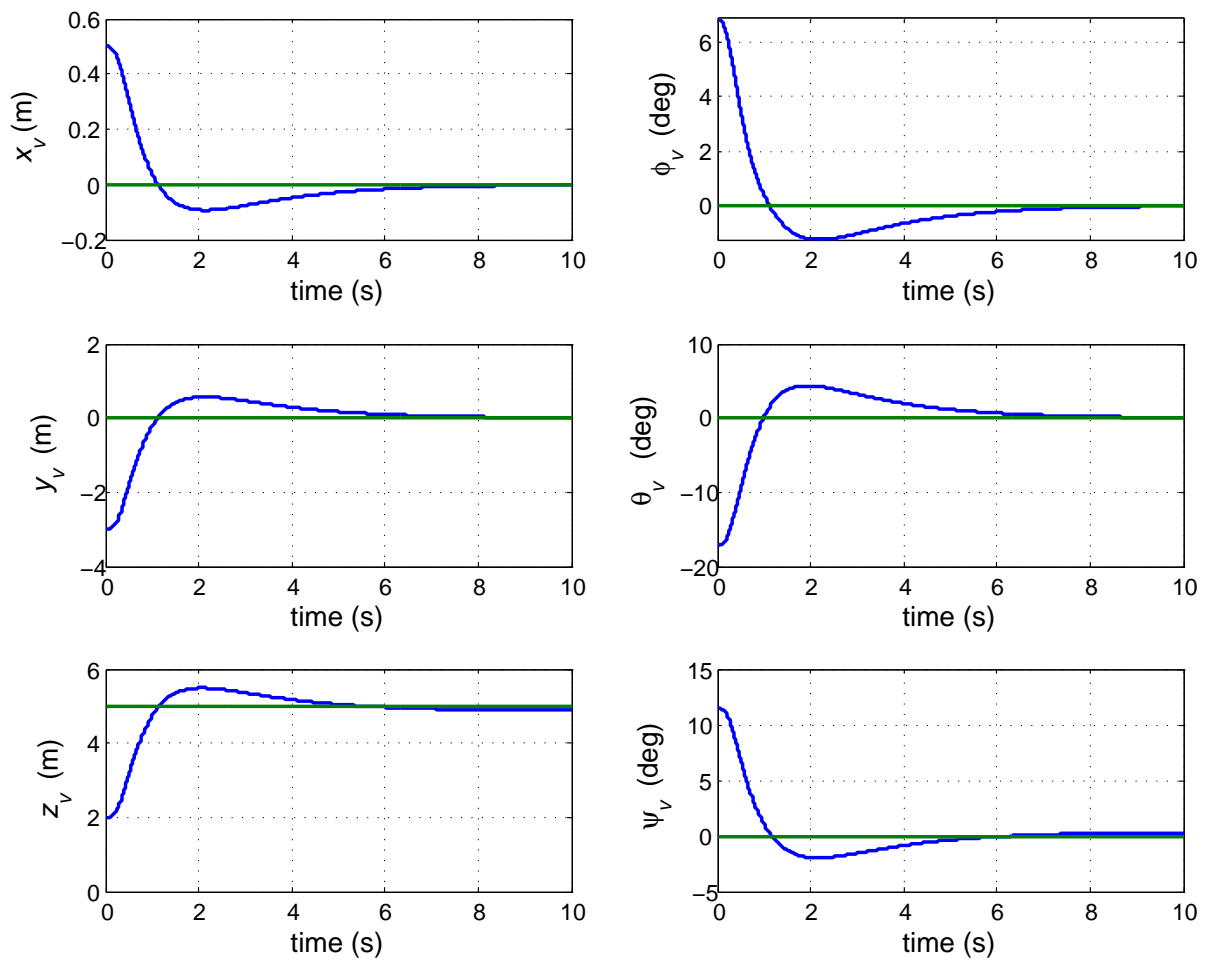


Figure 5.17: System performance under the two stage feedback linearisation associated with \mathcal{H}_∞ LSDP. The specified reference input is $(0, 0, 0)$ deg for the attitude and $(0, 0, 5)$ m for the position in the earth frame. The UAV was in a non-zero initial position and attitude.

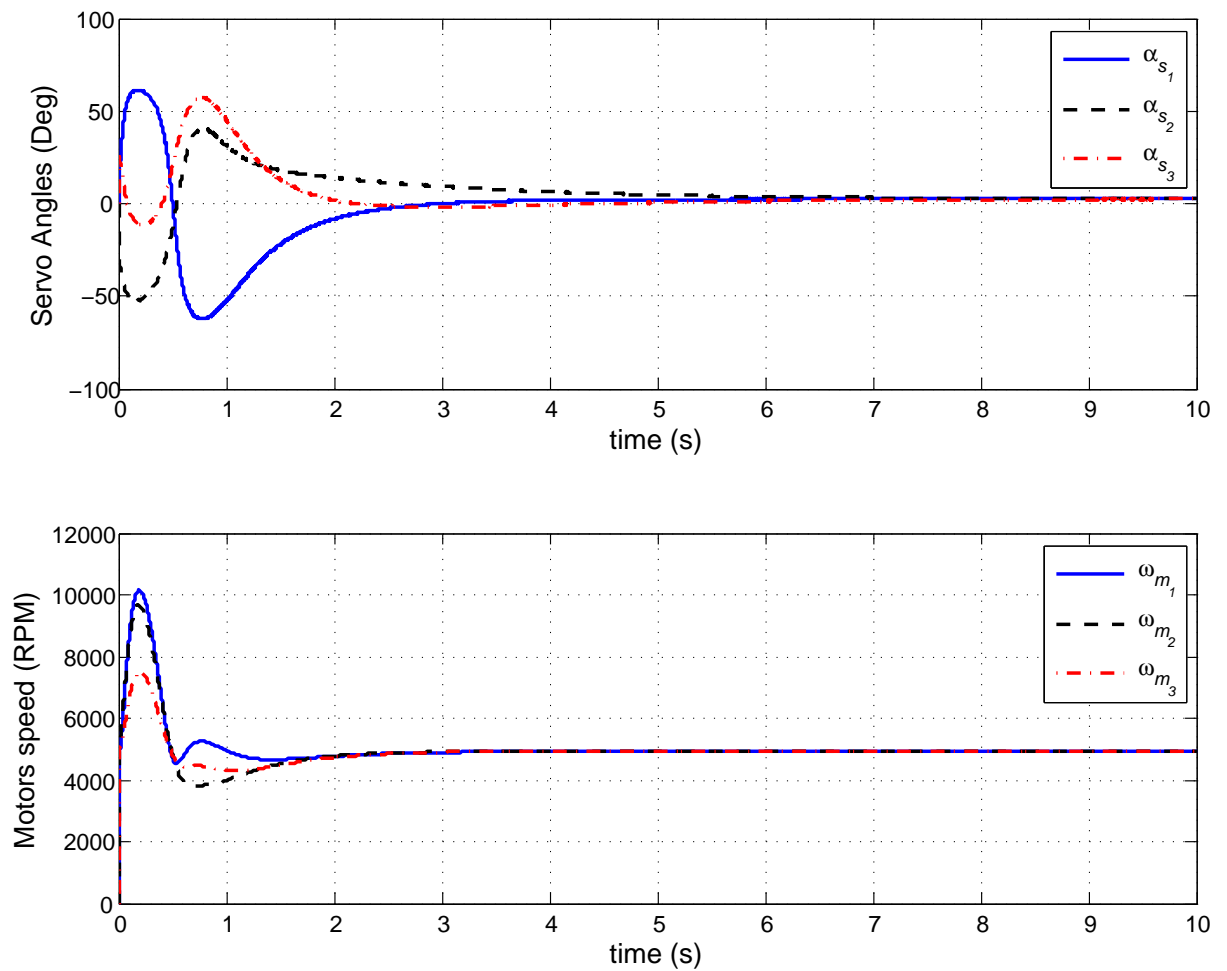


Figure 5.18: Actuator behaviour under the two stage feedback linearisation associated with \mathcal{H}_∞ LSDP. The specified reference input is $(0, 0, 0)$ deg for the attitude, and $(0, 0, 5)$ m for the position. The servos and BLDC motors operate within their physical limits of $\pm 90^\circ$ for the servos and 12000 rpm for the BLDC motors.

5.5 Propulsion System Design

In this Section, we consider designing the propulsion system for the Tri-rotor UAV using the propulsion system design procedure proposed in Chapter 3, see Section 3.3, where throughout this section, we will refer to the design steps described in Section 3.3 accordingly. The designed Tri-rotor UAV has a maximum area (including the dimension of the propellers) of $1 \text{ m}^2 \approx 1550 \text{ inch}^2$ and an estimated total mass⁴ of 10 Kg. The structure of the vehicle is represented again in Figure 5.19, where three identical electric propulsion subsystems (units) are positioned in a triangular arrangement. Each propulsion unit uses a BLDC motor to drive a propeller, and all three propellers are rotating in the same plane. Keeping a sufficient clearance of $10 \text{ cm} = 3.37''$ among the blades of propellers makes the maximum permitted radius of the propeller $R_{p_{max}} = 9''$. For a safety factor of $\alpha = 1.2$, each propulsion unit needs to generate at least an approximate thrust of $\frac{f_h}{3} = \frac{10 \times 9.81 \times 1.2}{3} \approx 40 \text{ N}$ for taking off and hovering (**Step 1**), where the estimated weight of the vehicle is $M_{total} = 10 \times 9.81 = 98.1 \text{ N}$. For simplicity, all weight values used later in this design will be expressed using the mass unit (kg). The weight of the mechanical structure of the vehicle and the payload give a maximum weight allowance of $M_{s_{max}} = 4.5 \text{ Kg}$ for the propulsion system; i.e. 1.5 Kg for each propulsion unit. Let the specified minimum flight time be $t_{f_{min}} = 200 \text{ s}$. The propulsion system design will consider two cases; in the first case each propulsion unit is powered individually by a separate battery pack while the second case considers a parallel powering of all propulsion units by the same battery pack.

⁴This includes the structure, the payload and the propulsion system.

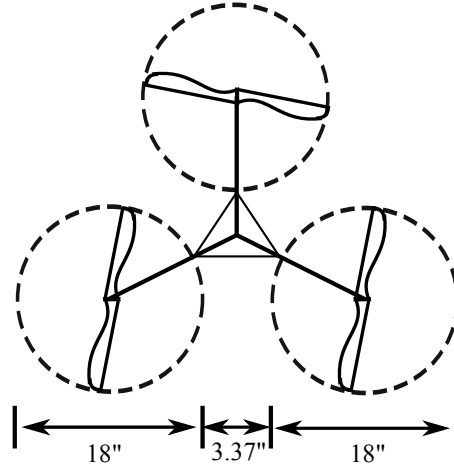


Figure 5.19: Tri-rotor UAV design (vertical view)

Nine APC Electrical Thin propellers manufactured by "Land Product" (set \mathbb{P}) are selected for the design (**Step 2a**) with an average chord-to-radius ratio of $d/R = 0.16$ for all nine propellers. The propeller's diameter and pitch length are denoted respectively by D and β . The maximum speed limit of propellers is specified by the manufacturer as $\omega_{p_{max}}(\text{RPM}) = 190,000/D_p(\text{"})$, where D_p is the diameter of the corresponding propeller. For all propellers $p \in \mathbb{P}$, the maximum rotational speed limit $\omega_{p_{max}}$, the rotational speed ω_p and the mechanical power P_{f_p} required to generate the required thrust are calculated (**Step 2b**) and shown in Table 5.1. All propellers are feasible to the design as the maximum rotational speed of each propeller is greater than the required rotational speed; i.e., $\omega_{p_{max}} > \omega_p \forall p \in \mathbb{P}$. Hence, $\bar{\mathbb{P}} = \mathbb{P}$ (**Step 2c**).

Table 5.1: Propellers data

No.	1	2	3	4	5	6	7	8	9
Propeller ($D \times \beta$)	16×8	16×10	16×12	17×8	17×10	17×12	18×8	18×10	18×12
$\omega_{p_{max}}$ (RPM)		11875			11176			10556	
P_{f_p} (W)		443.22			417.15			393.97	
ω_p (RPM)	7424.1	6439.1	5757.1	6842.2	5925.4	5290.7	6337.6	5480.8	4887.7

Three BLDC motors manufactured by "Maxx Product" (set \mathbb{M}) are chosen for the propulsion system design (**Step 3a**). The chosen motors with their technical specifications are

listed in Table 5.2. All motors can be grouped with all selected propellers as:

$$\min_{m \in \mathbb{M}} \omega_{m_{max}} > \max_{p \in \overline{\mathbb{P}}} \omega_p \quad \text{and} \quad \min_{m \in \mathbb{M}} P_{m_{max}} > \max_{p \in \overline{\mathbb{P}}} P_{fp}.$$

Hence, there are three groups G_j , $j = 1, 2, 3$ (**Step 3b**) and in each group, there is a motor and nine propellers, see Table 5.3.

Table 5.2: Motors data

No.	Motor	$P_{m_{max}}$ (W)	k_{v_m} (RPM/V)	M_m (Kg)	$\omega_{m_{max}}$ (RPM)	Efficient Operating Current Region (A)	$I_{m_{max}}$ (A)
1	HC5018-530	900	530	0.275	12000	30-50	50
2	HC5030-390	1500	390	0.395	12000	30-50	50
3	HC6320-250	1700	250	0.450	10000	30-60	60

The required voltage and current necessary to operate the motors with the load of the selected propellers (**Step 3c**) are obtained from the load graphs of the motor and the technical specification of k_v (see Section 3.2.3) and they are shown in Table 5.3. The current in brackets indicates the case of infeasibility or inefficiency. The infeasibility occurs when the required current is greater than the maximum allowed continuous current of the motor; i.e., $I_p^j > I_{m_{j_{max}}}$ and the inefficient condition appears when the calculated current is outside the efficient operating current region of the motor (see Table 5.2). Among all efficient as well as feasible cases from all groups, the minimum and maximum required voltages are respectively 10.86 V and 29.7 V. These voltages are important for deciding the set of batteries to be selected for the design (see Remark 4 in Section 3.3).

Table 5.3: Selection groups

Group	Motor	Propeller (D" × β")	V_p^j (V)	I_p^j (A)
G_1	HC5018-530	16 × 8	14	(55)
		16 × 10	12.15	48
		16 × 12	10.86	45
		17 × 8	12.91	(55)
		17 × 10	11.18	47
		17 × 12	9.98	(> 60)*
		18 × 8	11.96	(> 60)*
		18 × 10	10.34	(> 60)*
		18 × 12	9.22	(> 60)*
G_2	HC5030-390	16 × 8	19.03	45
		16 × 10	16.51	37
		16 × 12	14.76	39
		17 × 8	17.54	43
		17 × 10	15.19	(56)
		17 × 12	13.57	36
		18 × 8	16.25	41
		18 × 10	14.05	38
		18 × 12	12.53	37
G_3	HC6320-250	16 × 8	29.7	30
		16 × 10	25.76	(< 30)*
		16 × 12	23.03	(< 30)*
		17 × 8	27.37	(28)
		17 × 10	23.7	(< 30)*
		17 × 12	21.16	(< 30)*
		18 × 8	25.35	(< 30)*
		18 × 10	21.92	(< 30)*
		18 × 12	19.56	(< 30)*

*The current value is far outside the efficient range of the motor and this operating point lies outside the operational chart supplied by the manufacturer.

The battery packs will be used in this design are Li-Po batteries manufactured by "Thunder Power". They have different voltage capacities with a step increment of 3.7 V and for each voltage level, different current ratings are available. The technical specifications of these batteries indicate that the effective voltage is approximately 90% of the nominal voltage when the battery pack discharges the maximum current [118]; i.e., $V_b = 0.9V_{b_0}$. Therefore, supplying the minimum required voltage of $V_b = 10.86$ V needs at least a pack of nominal voltage $V_{b_0} = 10.86/0.9 = 12.067$ V, and for the maximum voltage of 29.7 V, we need a battery of nominal voltage $V_{b_0} = 29.7/0.9 = 33$ V. With an increment of 3.7 V, the required nominal voltage for minimum and maximum cases are respectively, 14.8 V and 33.3 V.

Case 1: Individual Powering of The Propulsion Subsystems

In this case, battery packs are chosen to consider a separate powering of the three propulsion units; i.e., the propulsion system involves three batteries to power the three motors. For each feasible pair from Table 5.3, a set of battery packs (\mathbb{B}_p^j) is chosen for the design (**Steps 4a**). For example, Table 5.4 shows the set of battery packs along with the calculated flight time and propulsion system weight (**Step 4b**) for the feasible pair $(m_1 = \text{HC5018-530}, p = 16" \times 10") \in G_1$.

Table 5.4: Battery pack selection for the feasible motor-propeller pair $(m_1 = \text{HC5018-530}, p = 16" \times 10")$.

Group	m_j	p	V_p^j (V)	I_p^j (A)	b	$t_{(m_j,p,b)}$ (s)	$M_{(m_j,p,b)}$ (Kg)
G_1	$m_1 = \text{HC5018-530}$	$16" \times 10"$	12.15	48	TP4000-4S2PL	300	0.613
					TP6000-4S3PL	450	0.763
					TP8000-4S4PL	600	0.908
					TP3300-4SPL2	247.5	0.59
					TP2700-4SSR	202.5	0.568
					TP5000-5SPL2	375	0.863
					TP3900-6SPL2	292.5	0.809
					TP4350-6SPL2	326.25	0.898

Table 5.5 shows all battery packs that are selected for all feasible pairs where each battery is matched with one or more motor-propeller pairs based on its specifications: V_{b_0} , I_{b_0} and $C_{b_{max}}$.

Table 5.5: Batteries for separate powering of the propulsion system units. The table includes batteries packs for all feasible pairs.

No.	Battery	V_{b_0} (V)	I_{b_0} (Ah)	$c_{b_{max}}$	M_b (kg)
1	TP4000-4S2PL	14.8	4	16	0.338
2	TP6000-4S3PL	14.8	6	16	0.488
3	TP8000-4S4PL	14.8	8	16	0.633
4	TP2600-4SPL2	14.8	2.6	20	0.238
5	TP3300-4SPL2	14.8	3.3	20	0.315
6	TP2700-4SSR	14.8	2.7	25	0.293
7	TP4000-5S2PL	18.5	4	16	0.416
8	TP6000-5S3PL	18.5	6	16	0.627
9	TP8000-5S4PL	18.5	8	16	0.79
10	TP2600-5SPL2	18.5	2.6	20	0.292
11	TP3300-5SPL2	18.5	3.3	20	0.392
12	TP5000-5SPL2	18.5	5	20	0.588
13	TP2600-6SPL2	22.2	2.6	20	0.352
14	TP3300-6SPL2	22.2	3.3	20	0.468
15	TP3900-6SPL2	22.2	3.9	20	0.534
16	TP4350-6SPL2	22.2	4.35	20	0.623
17	TP5000-6SPL2	22.2	5	20	0.716
18	TP3900-9SPL2	33.3	3.9	20	0.79
19	TP4350-9SPL2	33.3	4.35	20	0.935
20	TP5000-9SPL2	33.3	5	20	1.054

Finally, the flight time and propulsion system weight are calculated for all feasible pairs in all groups when using the corresponding battery pack (**Step 4c**). It is worthy here to remind the reader that the calculated flight time assumes a full load of 10 Kg regardless of the weight of the selected propulsion system. Figure 5.20 shows the calculated flight time t_f and propulsion system weight M_p for all efficient and feasible combinations. In this graph, each propulsion system design is represented by its components' number (the motor's number, the propeller's number, the battery's number), where these numbers are taken respectively from Tables 5.2, 5.1 and 5.5. The weight of the propulsion system shown in this graph equals to the total weight of the three propulsion subsystems. Over all efficient and feasible cases, the best design (**Step 5**) are:

(a) in terms of maximum flight time: ($m_t = \text{HC5030-390}$, $p_t = 17" \times 12"$, $b_t = \text{TP8000-5S4PL}$), or (2,6,9) in Figure 5.20. This propulsion system design weighs $M_p = 3.555 \text{ Kg}$ and gives a flight time of $t_f = 800 \text{ s}$.

(b) in terms of minimum propulsion system weight: ($m_w = \text{HC5018-530}$, $p_w = 16" \times 12"$, $b_w = \text{TP2600-4SPL2}$), which is (1,3,4) in Figure 5.20. This propulsion system weighs $M_p = 1.539 \text{ Kg}$ and gives a flight time of $t_f = 208 \text{ s}$.

For a trade-off between weight and flight time, other alternative designs can be selected. For instance, the combination ($m = \text{HC5030-390}$, $p = 16" \times 10"$, $b = \text{TP4000-5S2PL}$) = (2,2,7) produces a propulsion system with a total weight of $M_p = 2.433 \text{ Kg}$ and a flight time of $t_f = 389 \text{ s}$ while the combination ($m = \text{HC5030-390}$, $p = 16" \times 10"$, $b = \text{TP2600-5SPL2}$) = (2,2,10) is a propulsion system with a total weight of $M_p = 1.971 \text{ Kg}$ and a flight time of $t_f = 253 \text{ s}$.

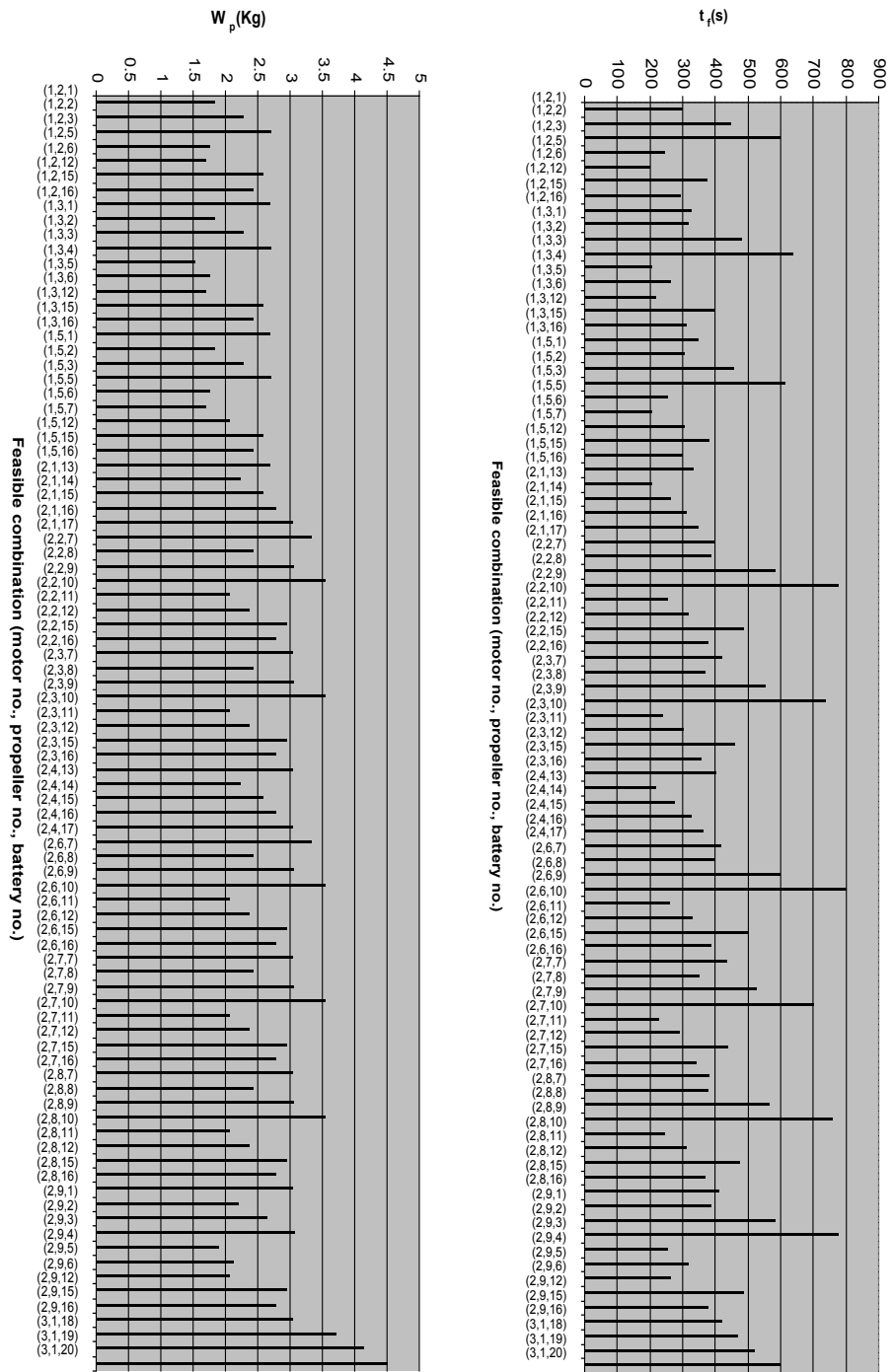


Figure 5.20: Weight and flight time and of all feasible designs of the propulsion system (motors are powered individually by separate battery packs.).

Case 2: Parallel Powering of The Three Subsystems

This case considers the design of parallel powering for the three propulsion subsystems. The required batteries in this case should have the same voltage capacity as the batteries chosen in Table 5.5 because they need to power the three subsystems in parallel. However, the maximum continuous discharging current of the new battery sets must be higher and sufficient to power all three motors in parallel; i.e., $I_{b_{max}} = I_{b_0} c_{b_{max}} \geq 3I_p^j \forall b \in \mathbb{B}_p^j$. Table 5.6 shows all battery packs that used in battery sets for all feasible pairs while considering the parallel powering of the propulsion units.

Table 5.6: Batteries for parallel powering of the propulsion subsystems.

No.	battery	V_{b_0} (V)	I_{b_0} (Ah)	$c_{b_{max}}$	M_b (kg)
1	TP2650-4SP45	14.8	2.65	45	0.296
2	TP3250-4SP45	14.8	3.25	45	0.357
3	TP3850-4SP30	14.8	3.85	30	0.409
4	TP4400-4SP30	14.8	4.4	30	0.479
5	TP5000-4SP30	14.8	5	30	0.516
6	TP5400-4SSR	14.8	5.4	25	0.558
7	TP2650-5SP45	18.5	2.65	45	0.367
8	TP3250-5SP45	18.5	3.25	45	0.443
9	TP3850-5SP30	18.5	3.85	30	0.508
10	TP4400-5SP30	18.5	4.4	30	0.592
11	TP5000-5SP30	18.5	5	30	0.647
12	TP6000-5S3PL	18.5	6	25	0.627
13	TP6600-5SPL2	18.5	6.6	20	0.766
14	TP8000-5S4PL	18.5	8	25	0.79
15	TP3250-6SP45L	22.2	3.25	45	0.548
16	TP3800-6SP45	22.2	3.8	45	0.620
17	TP4400-6SP30L	22.2	4.4	30	0.712
18	TP5000-6SP30L	22.2	5	30	0.805
19	TP3250-9SP45	33.3	3.25	45	0.786
20	TP3850-9SP30	33.3	3.85	30	0.899
21	TP5000-9SPL2	33.3	5	20	1.054

Figure 5.21 presents the flight time and weight of all possible designs for parallel powering of the three motors, where the designs are represented in the same way as in Figure 5.20 (each propulsion system design is represented by its components' number (the

motor's number, the propeller's number, the battery's number), where the numbers are taken respectively from Tables 5.2, 5.1 and 5.5). Comparing with the previous case of individual powering of the subsystems (see Figure 5.20), there are less feasible combinations in the case of parallel powering of the motors. This is due to the fact that the current requirement is much higher in case of parallel powering and only few batteries can fulfill this current condition. The design ($m_t = \text{HC5030-390}$, $p_t = 17" \times 12"$, $b_t = \text{TP8000-5S4PL}$), which is (2,6,14) in Figure 5.21, gives the maximum flight time of $t_f = 267$ s and weighs $M_p = 1.975$ Kg. On the other hand, the design ($m_w = \text{HC5018-530}$, $p_w = 16" \times 12"$, $b_w = \text{TP8000-5S3PL}$) = (1,3,14) results in the minimum propulsion system weight of $M_p = 1.615$ Kg and a flight time of about $t_f = 213$ s.

Comparing with the previous case of separate powering of the propulsion subsystems, the parallel powering of the motors produces approximately similar results when considering the minimum weight design while the first case gives considerably better flight time when considering the best flight time design.

In experiment, the Tri-rotor UAV is built by implementing the minimum weight design of the parallel powering of the three propulsion subsystems in order to simplify the electrical structure of the vehicle.

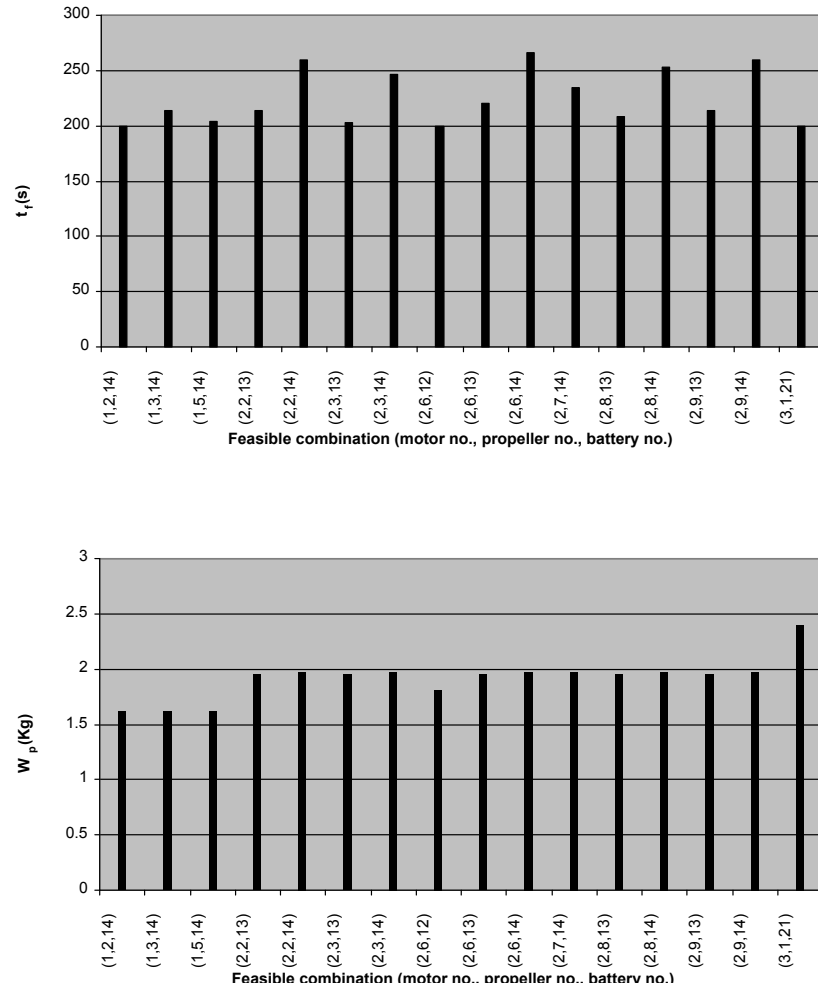


Figure 5.21: Flight time and weight of all feasible designs of the propulsion system (motors are powered in parallel by the same battery pack.).

5.6 Hardware Assembly

The target was to build the Tri-rotor UAV, run hardware experiment and record the stability and performance of the system under the synthesized controllers. Unfortunately, due to the time limit of the PhD program, the target was not fulfilled completely. The vehicle was built with all equipment, yet, a communication problem between the navigation system and main processor of the vehicle hinders the completion of the experiment. Figure

5.22 below presents a picture of the complete Tri-rotor UAV.

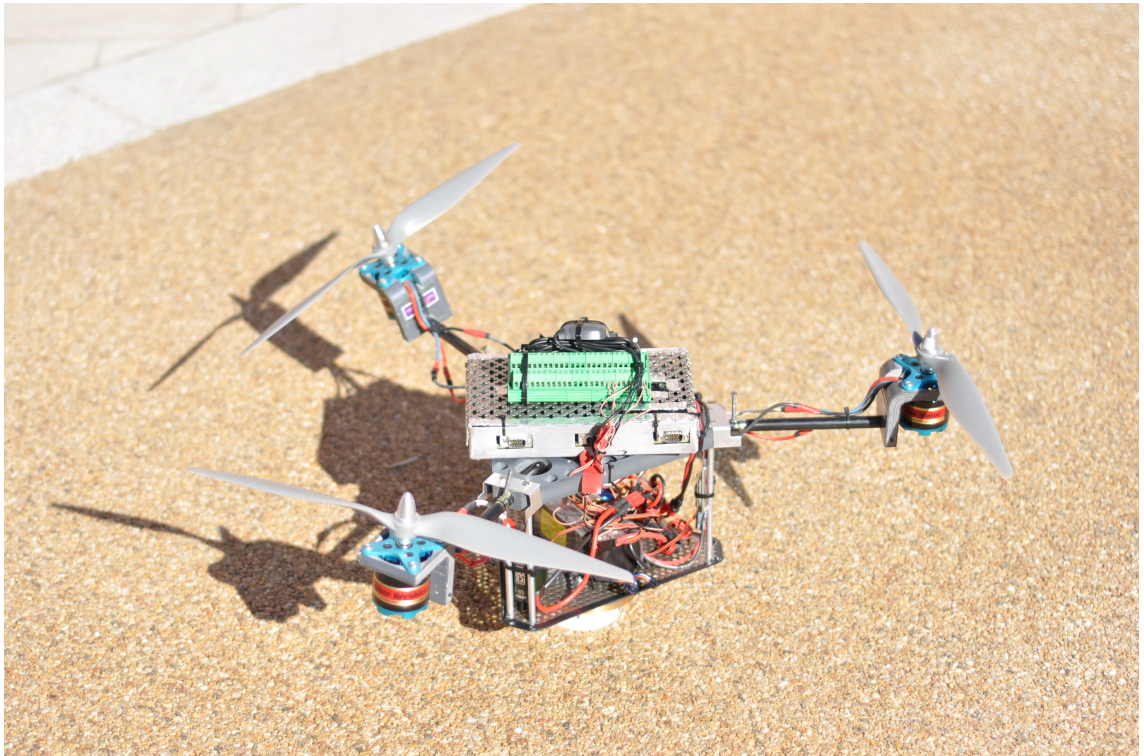


Figure 5.22: The final structure of the designed Tri-rotor UAV.

5.7 Summary

Tri-rotor UAVs are more efficient compared to quadrotors in regard to their size and power requirement, yet, they are more challenging in terms of control and stability due to their asymmetric structure. In this chapter, we propose the design and control of a novel tri-rotor UAV. The proposed tri-rotor has a triangular shape of three arms where at the end of each arm, a fixed pitch propeller is driven by a DC motor. A tilting mechanism is employed to tilt the motor-propeller assembly and produce thrust in the desired direction. The three propellers can be tilted independently and the resulting vehicle is a fully actuated system of six actuators with full authority of thrust and torque vectoring. A feedback linearisation associated with \mathcal{H}_∞ loop shaping design is used to synthesize a centralized controller for the system. The centralized controller stabilize the vehicle, regulate the attitude of the vehicle and track the position trajectory simultaneously for all channels. Throughout the control system design for the proposed platform, the advantages of the two stage feedback linearisation are highlighted via a comparison study between the proposed linearisation method and the classical feedback linearisation of the full system including actuator dynamics. The chapter presents also a simulation based analysis of the destabilization effect of unmodeled actuator dynamics on the stability of the Tri-rotor UAV.

The chapter also presents a systematic design for the propulsion system of the Tri-rotor UAV using the design procedure proposed in Chapter 3. Two cases are considered here, i.e. individual powering and parallel powering of the three propulsion systems units.

Chapter 6

Concluding Remarks

By a way of conclusion, this chapter summarizes the main contributions of the thesis and outlines some possible directions for future research.

6.1 Contributions

Investigating different perspectives of UAV systems from design to operation and control, the main contributions of this thesis are summarized as follows:

- Given the fact that UAV systems are nonlinear in general, this thesis produces an analysis of the effect of unmodeled actuator dynamics on the stability of nonlinear systems when using feedback linearisation technique. The analysis shows the potential destabilization effect of unmodeled actuator dynamics regardless of how fast actuators are. The thesis suggests two stage feedback linearisation to compensate for actuator dynamics in the first stage and then linearize the main nonlinear system in the second stage. The proposed two stage feedback linearisation is less complex and needs less computation capacity when compared with feedback linearisation for full system including actuator dynamics.

- Deriving a new thrust and power models for air propellers based on the momentum theory. The aim of the derived model is to provide a simple tool that can be used by engineers to implement the propulsion system design procedure proposed in this thesis as well. The proposed thrust and power models might be less accurate when compared with complicated models available in literature but it is more handy when considering the design of electric propulsion system for small UAVs. The derived thrust model has been verified for some propellers available in hand.
- Proposing a new explicit and easy to implement design procedure for choosing and matching the components of electric propulsion system for VTOL UAVs. Based on the available products in the market, the proposed design method aims to optimize the selection of electric propulsion system components. The goal of the design procedure is to generate sufficient thrust for the vehicle while in the same time maximize the thrust to weight ratio of the propulsion system, prolong the flight time of the vehicle and increase the payload capability of the UAV.
- Presenting a novel indoor navigation system for UAVs. The proposed system uses a computer vision technique and three laser beams to determine the 3D-position and orientation of the vehicle. The system provides full information about the position and orientation of the UAV based on the length of the three laser beams along with the positions of their projections on the ground. Compared with other existing computer vision navigation methodologies, the proposed system is less complicated and requires less computational capabilities.
- Proposing the design and control of a novel tri-rotor UAV system that can achieve six degree of freedom using thrust vectoring technique. Compared to quadrotors and other tri-rotor configurations, the proposed platform is more flexible and maneuverable. The proposed system is advantageous when considering the attitude and position control as the system is square, i.e., fully actuated. The designed control system is a centralized \mathcal{H}_∞ controller for translational and rotational motion simultaneously. The centralized \mathcal{H}_∞ control can be implemented using a single feedback loop system and it is robust to cross-coupling unmodeled dynamics and disturbances.

6.2 Directions for Future Research

Each research problem discussed in this thesis has its own potential for further research. Some possible directions for points tackled in the thesis are hereby outlined.

Two stage feedback linearisation The advantages of the proposed two stage feedback linearisation are outline via examples and simulation in this thesis. It is desirable to derive an analytical study of the proposed method and measure mathematically the robustness of this feedback linearisation against measurement noise and other types of disturbances.

Thrust model of air propeller Further verification experimental study for the presented model of thrust and power of air propellers can be performed to cover wide range of propellers. A comparison study between this model and more advanced models in the literature is believed to be useful to identify the accuracy of this model and spot the required modifications needed to improve it.

Propulsion System Design The propulsion system design procedure developed in this thesis is for VTOL vehicles. It is desirable to extend the procedure to include fixed-wings vehicles and other non-conventional UAVs.

Indoor navigation system Due to time limitation, the proposed indoor navigation system has not been implemented and tested. An implementation experiment is useful to highlight the advantages and disadvantages of this navigation strategy and compare it with other computer-vision navigation systems. The effect of the sensor noise and image quality on the accuracy of the proposed system can be analysed to study the robustness of the system.

Tri-rotor UAV Hardware experiments could be completed to test the proposed UAV and compare the behaviour of the system against other common configuration of quadrotors systems. It is believed that this comparison study is essential to indicate the negative and positive sides of the proposed system and highlight any potential for future development of the vehicle.

Centralized control synthesis for the Tri-rotor UAV It is perhaps useful to investigate advanced feedback linearisation such as the proposed robust feedback linearisation in [119] and compare it with classical feedback linearisation when considering a centralized controller synthesis for the proposed Tri-rotor UAV.

References

- [1] S. G. Tzafestas, Ed., *Robotic Systems: Advanced Techniques and Applications*, 1st ed. Springer, 1992.
- [2] D. Liu, L. Wang, and K. C. Tan, Eds., *Design and Control of Intelligent Robotic Systems*. Springer, 2009.
- [3] K. P. Valavanis, Ed., *Advances in Unmanned Aerial Vehicles: State of the Art and the Road to Autonomy*, ser. International Series on Intelligent Systems, Control, and Automation: Science and Engineering. Springer, 2007, vol. 33.
- [4] D. Glade, “Unmanned aerial vehicles: Implications for military operations,” Center for Strategy and Technology, Air War College, Air University, Maxwell Air Force Base, Alabama 36112, Technical Report 16, July 2000.
- [5] S. Davies, “UAVs in the firing line,” *Engineering & Technology*, vol. 6, no. 8, pp. 34–36, 2011.
- [6] Z. Sarris, “Survey of UAV applications in civil markets,” in *Proceedings of The 9th IEEE Mediterranean Conference on Control and Automation (MED’01)*, Dubrovnik, Croatia, June 2001, pp. 1–11.
- [7] M. Okrent, “Civil UAV activity within the framework of European commission research,” in *Proceedings of The AIAA 3rd Unmanned Unlimited Technical Conference, Workshop and Exhibit*, Chicago, IL, USA, September 2004, pp. 1–11.
- [8] T. H. Cox, C. J. Nagy, M. A. Skoog, I. A. Somers, and R. Warner, “Civil UAV capability assessment,” NASA, Technical Report, Draft Version, December 2004.

- [9] P. Vanblyenburgh, "UAVs: An overview," *Air & Space Europe*, vol. 1, no. 5-6, pp. 43–47, 1999.
- [10] P. Doherty, "Advanced research with autonomous unmanned aerial vehicles," in *Proceedings of The 9th International Conference on The Principles of Knowledge Representation and Reasoning*, Whistler, British Columbia, Canada, June 2004, pp. 731–732.
- [11] S. S. Wegener, S. M. Schoenung, T. Totah, D. Sullivan, J. Frank, F. Enomoto, C. Frost, and C. Theodore, "UAV autonomous operations for airborne science missions," in *Proceedings of The AIAA 3rd "Unmanned Unlimited" Technical Conference, Workshop and Exhibit*, Chicago, Illinois, USA, September 2004, pp. 1–10.
- [12] *Unmanned Aircraft Systems Roadmap 2005-2030*, Office of the Secretary of Defence, Department of Defense, United States of America, August 2005.
- [13] P. Spanoudakis, L. Doitsidis, N. C. Tsourveloudis, and K. P. Valvanis, "Vertical take-off and landing vehicle market overview," *Unmanned Systems Magazine*, vol. 21, no. 5, pp. 14–18, 2003.
- [14] D. H. Lyon, "A military perspective on small unmanned aerial vehicle," *IEEE Instrumentation & Measurement Magazine*, vol. 7, no. 3, pp. 27–31, 2004.
- [15] S. Bouabdallah, P. Murrieri, and R. Siegwart, "Design and control of an indoor micro quadrotor," in *Proceedings of The 2004 IEEE International Conference on Robotics and Automation*, vol. 5, New Orleans, LA, April 2004, pp. 4393 – 4398.
- [16] A. Ficola, M. L. Fravolini, V. Brunori, and M. LaCava, "A simple control scheme for mini unmanned aerial vehicles," in *Proceedings of The 14th Mediterranean Conference on Control and Automation, MED'06*, Ancona, Italy, June 2006, pp. 1–6.
- [17] M. A. Goodrich, J. L. Cooper, J. A. Adams, C. Humphrey, R. Zeeman, and B. G. Buss, "Using a mini-UAV to support wilderness search and rescue: Practices for human-robot teaming," in *IEEE International Workshop on Safety, Security and Rescue Robotics, SSRR 2007*, Rome, Italy, September 2007, pp. 1–6.

- [18] D. J. Pines and F. Bohorquez, "Challenges facing future micro-air-vehicle development," *AIAA Journal of Aircraft*, vol. 43, no. 2, pp. 290–305, 2006.
- [19] B. Siciliano, O. Khatib, and F. Groen, Eds., *Multiple Heterogeneous Unmanned Aerial Vehicles*, ser. Springer Tracts in Advanced Robotics. Springer, 2007, vol. 37.
- [20] Y. Qu, "Cooperative localization against GPS signal loss in multiple UAVs flight," *Journal of Systems Engineering and Electronics*, vol. 22, no. 1, pp. 103 – 112, 2011.
- [21] E. Pastor, J. Lopez, and P. Royo, "UAV payload and mission control hardware/software architecture," *IEEE Aerospace and Electronic Systems Magazine*, vol. 22, no. 6, pp. 3 – 8, 2007.
- [22] D. M. O'Brien, "Analysis of computational modeling techniques for complete rotorcraft configurations," Ph.D. dissertation, School of Aerospace Engineering, Georgia Institute of Technology, May 2006.
- [23] R. Austin, *Unmanned Aircraft Systems: UAVs Design, Development and Deployment*. Wiley, 2010.
- [24] G. Cai, B. M. Chen, and T. H. Lee, *Unmanned Rotorcraft Systems*, ser. Advances in Industrial Control. Springer, 2011.
- [25] C. Sconyers, I. A. Raptis, and G. J. Vachtsevanos, "Rotorcraft control and trajectory generation for target tracking," in *Proceedings of The 2011 19th Mediterranean Conference on Control & Automation (MED)*, Corfu, Greece, June 2011, pp. 1235 – 1240.
- [26] T. Dierks and S. Jagannathan, "Output feedback control of a quadrotor UAV using neural networks," *IEEE Transactions on Neural Networks*, vol. 21, no. 1, pp. 50 – 66, 2010.
- [27] D. Lee, H. J. Kim, and S. Sastry, "Feedback linearization vs. adaptive sliding mode control for a quadrotor helicopter," *International Journal of Control, Automation and Systems*, vol. 7, no. 3, pp. 419–428, 2009.

- [28] A. Mokhtari, N. K. M. Sirdi, K. Meghriche, and A. Belaidi, “Feedback linearization and linear observer for a quadrotor unmanned aerial vehicle,” *Advanced Robotics*, vol. 20, no. 1, pp. 71–91, 2006.
- [29] J. Chen and Y. Wang, “The guidance and control of small net-recovery UAV,” in *Proceedings of The 2011 Seventh International Conference on Computational Intelligence and Security (CIS)*, Hainan, China, December 2010, pp. 1566 – 1570.
- [30] G. Cai, B. M. Chen, K. Peng, M. Dong, and T. H. Lee, “Modeling and control of the yaw channel of a UAV helicopter,” *IEEE Transactions on Industrial Electronics*, vol. 55, no. 9, pp. 3426–3434, 2008.
- [31] Y. Kang and J. K. Hedrick, “Linear tracking for a fixed-wing UAV using nonlinear model predictive control,” *IEEE Transactions on Control Systems Technology*, vol. 17, no. 5, pp. 1202–1210, 2009.
- [32] M. S. Mahmoud and M. Zribi, “Robust output feedback control for nonlinear systems including actuators,” *Systems Analysis Modelling Simulation*, vol. 43, no. 6, pp. 771–792, 2003.
- [33] R. W. Aldhaheri and H. K. Khalil, “Effect of unmodeled actuator dynamics on output feedback stabilization of nonlinear systems,” *Automatica*, vol. 32, no. 9, p. 1323–1327, 1996.
- [34] D. Chwa, J. Y. Choi, and J. H. Seo, “Compensation of actuator dynamics in nonlinear missile control,” *IEEE Transactions on Control Systems Technology*, vol. 12, no. 4, pp. 620–626, 2004.
- [35] H. A. Khalil, *Nonlinear Systems*, 2nd ed. Prentice Hall, Inc., 2001.
- [36] J. E. Slotine and W. Li, *Applied Nonlinear Control*. Prentice-Hall, Inc., 1991.
- [37] B. C. Kuo, *Automatic Control Systems*, 7th ed. Wiley & Sons Inc., 1995.
- [38] K. Zhou, J. C. Doyle, and K. Glover, *Robust Optimal Control*. Prentice-Hall, Inc., 1996.

- [39] M. Krstić, I. Kanellakopoulos, and P. Kokotović, *Nonlinear and Adaptive Control Design*, ser. Adaptive and Learning Systems for Signal Processing, Communications, and Control. Wiley-Blackwell, 1995.
- [40] C. L. Griffis, T. A. Wilson, J. A. Schneider, and P. S. Pierpont, “UAS propulsion systems technology survey,” Daytona Beach College of Aviation, Embry-Riddle Aeronautical University, Technical Report, May 2007.
- [41] ———, “Framework for the conceptual decomposition of unmanned aircraft propulsion systems,” in *Proceedings of The 2008 IEEE Aerospace Conference*, Big Sky, MT, USA, March 2008, pp. 1–10.
- [42] I. Moir and A. Seabridge, *Aircraft Systems: Mechanical, Electrical and Avionics Subsystems Integration*, 3rd ed. Wiley, 2008.
- [43] W. Crowther, P. Geoghegan, A. Lanzon, and M. Pilmoor, “Rotory wing vehicle,” Patent GB2 462 452-A; WO2 010 015 866-A2, August 8, 2008.
- [44] P. Lindahl, E. Moog, and S. R. Shaw, “Simulation, design and validation of a UAV SOFC propulsion system,” in *Proceedings of The 2009 IEEE Aerospace conference*, Big Sky, MT, USA, March 2009, pp. 1–8.
- [45] T. T. H. Ng and G. S. B. Leng, “Design of small-scale quadrotor unmanned air vehicles using genetic algorithms,” *Proceedings of The Institution of Mechanical Engineers, Part G: Journal of Aerospace Engineering*, vol. 221, no. 5, pp. 893–905, 2007.
- [46] M. P. Merchant, “Propeller performance measurement for low reynolds number unmanned aerial vehicle applications,” Master’s thesis, The college of Engineering and the faculty of the Graduate school of Wichita State University, Wichita, Kansas, USA, December 2005.
- [47] X. Qi, J. and Zhao, Z. Jiang, and J. Jianda, Han, “Design and implement of a rotorcraft UAV testbed,” in *Proceedings of The 2006 IEEE International Conference on Robotics and Biomimetics*, Kunming, China, December 2006, pp. 109 – 114.
- [48] G. Cai, A. K. Cai, B. M. Chen, and T. H. Lee, “Construction, modeling and control of a mini autonomous UAV helicopter,” in *Proceedings of The IEEE International*

- Conference on Automation and Logistics*, Qingdao, China, September 2008, pp. 449 – 454.
- [49] G. Cai, B. M. Chen, T. H. Lee, and M. Dong, “Design and implementation of a hardware-in-the-loop simulation system for small-scale UAV helicopters,” *Mechanics*, vol. 19, no. 7, pp. 1057–1066, 2009.
- [50] S. Salazar-Cruz, R. Lozano, and J. Escareño, “Stabilization and nonlinear control for a novel trirotor mini-aircraft,” *Control Engineering Practice*, vol. 17, no. 8, pp. 886–894, 2009.
- [51] M. Abdulrahim, R. Albertani, P. Barnswell, F. Boria, D. Claxton, J. Clifton, J. Cocquyt, K. Lee, S. Mitryk, and P. Ifju, “Design of the University of Florida surveillance and endurance micro air vehicles,” University of Florida, Gainesville, FL, USA, 7th Annual Micro Air Vehicle Competition Entry, April 2003.
- [52] R. Albertani, P. Barnswell, F. Boria, D. Claxton, J. Clifton, J. Cocquyt, A. Crespo, C. Francis, P. Ifju, B. Johnson, S. Jung, K. lee, and M. Morton, “University of Florida biologically inspired micro air vehicel,” University of Florida, Gainesville, FL, USA, 8th Annual Micro Air Vehicle Competition Entry, April 2004.
- [53] G. R. Spedding and P. B. S. Lissaman, “Technical aspects of microscale flight systems,” *Journal of Avian Biology*, vol. 29, no. 4, pp. 458–468, 1998.
- [54] W. F. Phillips, *Mechanics of Flight*. John Wiley & Sons, 2004.
- [55] W. Z. Stepniewski and C. N. Keys, *Rotory-Wing Aerodynamics*. Dover Publications, 1984.
- [56] J. Seddon and S. Newman, *Basic Helicopter Aerodynamics*, 2nd ed. Blackwell Science, 2001.
- [57] K. Kotwani, S. K. Sane, H. Arya, and K. Sudhakar, “Experimental characterization of propulsion system for mini aerial vehicle,” in *Proceedings of The 31st National Conference on Fluid Mechanics and Fluid Power FMFP*, vol. 2, Jadavpur University, Kolkata, India, December 2004, pp. 671–678.

- [58] O. Solomon, “Model reference adaptive control of a permanent magnet brushless DC motor for UAV electric propulsion system,” in *Proceedings of The 33rd Annual Conference of The IEEE Industrial Electronics Society (IECON)*, Taipei, Taiwan, November 2007, pp. 1186 – 1191.
- [59] G. Sincero, J. Cros, and P. Viarouge, “Efficient simulation method for comparison of brush and brushless DC motors for light traction application,” in *Proceedings of The 13th European Conference on Power Electronics and Applications, EPE’09*, Barcelona, Spain, September 2009, pp. 1–10.
- [60] H. Auinger, “Efficiency of electric motors under practical conditions,” *Power Engineering Journal*, vol. 15, no. 3, pp. 163–167, 2001.
- [61] (2010, May) Himax brushless outrunner motor HC6332-230. Technical Manual. [Online]. Available: <http://www.maxxprod.com/pdf/HC6332-230.pdf>
- [62] G. Cai, F. Lin, B. M. Chen, and T. H. Lee, “Systematic design methodology and construction of UAV helicopters,” *Mechatronics*, vol. 18, no. 10, pp. 545–558, 2008.
- [63] R. Huang, Y. Liu, and J. J. Zhu, “Guidance, navigation, and control system design for tripropeller vertical-takeoff-and-landing unmanned air vehicle,” *AIAA Journal of Aircraft*, vol. 46, no. 6, pp. 1837–1856, 2009.
- [64] J. Zhang, Y. Wu, and W. Liu, “Novel approach to position and orientation estimation in vision-based UAV navigation,” *IEEE Transactions on Aerospace and Electronic Systems*, vol. 46, no. 2, pp. 687–700, 2010.
- [65] F. Kendoul, I. Fantoni, and K. Nonami, “Optic flow-based vision system for autonomous 3D localization and control of small aerial vehicles,” *Robotics and Autonomous Systems*, no. 6-7, pp. 591–602, 2009.
- [66] S. de La Parra and J. Angel, “Low cost navigation system for UAV’s,” *Aerospace Science and Technology*, vol. 9, no. 6, pp. 504–516, 2005.
- [67] S. Ehsan and K. D. McDonald-Maier, “On-board vision processing for small UAVs: Time to rethink strategy,” in *Proceedings of The NASA/ESA Conference*

on Adaptive Hardware and Systems, AHS, San Francisco, CA, USA, July-August 2009, pp. 75–81.

- [68] M. R. Parks, “Vision based self motion estimation in a fixed wing aerial vehicle,” Master’s thesis, Faculty of Virginia Polytechnic Institute and State University, Blacksburg, VA, USA, January 2006.
- [69] A. L. Majdik, L. Tamas, M. Popa, I. Szoke, and G. Lazea, “Visual odometer system to build feature based maps for mobile robot navigation,” in *Proceedings of The 18th Mediterranean Conference on Control & Automation*, Marrakech, Morocco, June 2010, pp. 1200–1205.
- [70] J. Courbon, Y. Mezouar, L. Eck, and P. Martinet, “Efficient hierarchical localization method in an omnidirectional images memory,” in *Proceedings of The IEEE International Conference on Robotics and Automation, ICRA*, Pasadena, CA, USA, May 2008, pp. 13–18.
- [71] H. Bay, A. Ess, T. Tuytelaars, and L. V. Gool, “SURF: Speeded up robust features,” *Computer Vision and Image Understanding (CVIU)*, vol. 110, no. 3, pp. 346–359, 2008.
- [72] D. G. Lowe, “Object recognition from local scale-invariant features,” in *Proceedings of The 7th IEEE International Conference on Computer Vision*, vol. 2, Kerkyra, Greece, September 1999, pp. 1150–1157.
- [73] ———, “Distinctive image features from scale-invariant keypoints,” *International Journal of Computer Vision*, vol. 60, no. 2, pp. 91–110, 2004.
- [74] M. I. McCartney, S. Zein-Sabatto, and M. Malkani, “Image registration for sequence of visual image captured by UAV,” in *Proceedings of The IEEE Symposium on Computational Intelligence for Multimedia Signal and Vision Processing, CIMSVP '09*, Nashville, TN, USA, March- April 2009, pp. 91–97.
- [75] C. Xing and J. Huang, “An improved mosaic method based on SIFT algorithm for UAV sequence images,” in *Proceedings of The 2010 International Conference On Computer Design And Applications (ICCD)*, vol. 1, Qinhuangdao, China, June 2010, pp. 414–417.

- [76] K. Han and G. N. DeSouza, “Multiple targets geolocation using SIFT and stereo vision on airborne video sequences,” in *Proceedings of The IEEE/RSJ International Conference on Intelligent Robots and Systems, IROS*, St. Louis, MO, USA, October 2009, pp. 6327–5332.
- [77] K. P. Valavanis, P. Oh, and L. A. Piegl, Eds., *Unmanned Aircraft Systems: International Symposium On Unmanned Aerial Vehicles, UAV’08*. Springer Netherlands, 2009.
- [78] J. Courbon, Y. Mezouar, N. Nicolas Guénard, and P. Martinet, “Vision-based navigation of unmanned aerial vehicle,” *Control Engineering Practice*, vol. 18, no. 7, pp. 789–799, 2010.
- [79] S. K. Phang, J. J. Ong, R. T. C. Yeo, B. M. Chen, and T. H. Lee, “Autonomous mini-UAV for indoor flight with embedded on-board vision processing as navigation system,” in *Proceedings of The 2010 IEEE Region 8 International Conference on Computational Technologies in Electrical and Electronics Engineering (SIBIRCON)*, Listvyanka, Russia, July 2010, pp. 722 – 727.
- [80] Z. He, R. V. Iyer, and P. R. Chandler, “Vision-based UAV flight control and obstacle avoidance,” in *Proceedings of The American Control Conference*, Minneapolis, MN, USA, June 2006, pp. 2166–2170.
- [81] B. Sinopoli, M. Micheli, G. Donatoy, and T. J. Koo, “Vision based navigation for an unmanned aerial vehicle,” in *Proceedings of The IEEE International Conference on Robotics and Automation (ICRA 2001)*, vol. 2, Seoul, Korea, May 2001, pp. 1757 – 1764.
- [82] R. Lerner, E. Rivlin, and P. H. Rostein, “Error analysis for a navigation algorithm based on optical-flow and a digital terrain map,” in *Proceedings of The 2004 IEEE Computer Society on Computer Vision and Pattern Recognition, CVPR*, vol. 1, Washington, DC, USA, June-July 2004, pp. 604–610.
- [83] D. G. Sim, “Integrated position estimation using aerial image sequence,” *IEEE Transactions on Pattern Analysis and Machine Intelligence*, vol. 24, no. 1, pp. 1–18, 2002.

- [84] A. E. Barabanov and D. V. Romaev, "Design of helicopter autopilot," in *Proceedings of The European Control Conference, (ECC09)*, Budapest, Hungary, August 2009, pp. 3839–3844.
- [85] R. Gibb, R. Gray, and L. Scharff, *Aviation Visual Perception: Research, Misperception and Mishaps*. Ashgate, 2010.
- [86] H. Schaub and J. L. Junkins, *Analytical Mechanics of Space Systems*, ser. AIAA Education Series. AIAA, 2003, vol. 1.
- [87] D. Pedoe, *Geometry: A Comprehensive Course*. Dover Publications, 1970.
- [88] A. Das, K. Subbarao, and F. Lewis, "Dynamic inversion with zero-dynamics stabilisation for quadrotor control," *IET Control Theory and Applications*, vol. 3, no. 3, pp. 303–314, 2009.
- [89] H. J. Kim and D. H. Shim, "A flight control system for aerial robots: Algorithm and experiments," *Control Engineering Practice*, vol. 11, no. 12, pp. 1389–144, 2003.
- [90] C. W. Lum and B. Waggoner, "A risk based paradigm and model for unmanned aerial systems in the national airspace," in *Proceedings of the AIAA Infotech@Aerospace Conference*, St. Louis, Missouri, USA, March 2011, pp. 1–31.
- [91] J. Escareno, A. Sanchez, O. Garcia, and R. Lozano, "Triple tilting rotor mini-UAV: Modeling and embedded control of the attitude," in *Proceedings of The American Control Conference*, Seattle, Washington, USA, June 2008, pp. 3476–3481.
- [92] D.-W. Yoo, H.-D. Oh, D.-Y. Won, and M.-J. Tahk, "Dynamic modeling and stabilization technique for tri-rotor unmanned aerial vehicles." *International Journal of Aeronautical and Space Science.*, vol. 11, no. 3, pp. 167–174, 2010.
- [93] S. D. Prior, S.-T. Shen, A. S. White, S. Odedra, M. Karamanoglu, M. A. Erbil, and T. Foran, "Development of a novel platform for greater situational awareness in the urban military terrain," in *Proceedings of The 8th International Conference on Engineering Psychology and Cognitive Ergonomics: Held as Part of HCI International 2009*, San Diego, CA, USA, July 2009, pp. 120–125.

- [94] P. Rongier, E. Lavarec, and F. Pierrot, “Kinematic and dynamic modeling and control of a 3-rotor aircraft,” in *Proceedings of The 2005 IEEE International Conference on Robotics and Automation, ICRA 2005*, Barcelona, Spain, April 2005, pp. 2606–2611.
- [95] B. Crowther, A. Lanzon, M. Maya-Gonzalez, and D. Langkamp, “Kinematic analysis and control design for a non planar multirotor vehicle,” *Journal of Guidance, Control, and Dynamics*, vol. 34, no. 4, pp. 1157–1171, 2011.
- [96] F. Lin, W. Zhang, and R. D. Brandt, “Robust hovering control of a PVTOL aircraft,” *IEEE Transactions on Control Systems Technology*, vol. 7, no. 3, pp. 343–351, 2002.
- [97] J. Watkinson, *The Art of The Helicopter*. Butterworth-Heinemann, 2003.
- [98] F. Kendoul, I. Fantoni, and R. Lozano, “Modeling and control of a small autonomous aircraft having two tilting rotors,” *IEEE Transactions on Robotics*, vol. 22, no. 6, pp. 1297–1302, 2006.
- [99] P. Fan, X. Wang, and K.-Y. Cai, “Design and control of a tri-rotor aircraft,” in *Proceedings of The 8th IEEE International Conference on Control and Automation (ICCA)*, Xiamen, China, June 2010, pp. 1972–1977.
- [100] Z. Prime, J. Sherwood, M. Smith, and A. Stabile, “Remote control (RC) vertical take-off and landing (VTOL) model aircraft,” School of Mechanical Engineering, University of Adelaide, Adelaide, Australia, LevelIV Honours Project Final Report, October 2005.
- [101] G. D. Padfield, *Helicopter Flight Dynamics: The Theory and Application of Flying Qualities and Simulation Modeling*, 2nd ed. Wiley-Blackwell Publishing, 2007.
- [102] P. S. Sreetharan and R. J. Wood, “Passive aerodynamic drag balancing in a flapping wing microrobotic insect,” *Journal of Mechanical Design*, vol. 132, no. 5, pp. 051 006–1 – 051 006–11, 2010.
- [103] J. Escareno, S. Salazar, and R. Lozano, “Modelling and control of a convertible VTOL aircraft,” in *Proceedings of The 45th IEEE Conference on Decision and Control*, San Diego, CA, USA, December 2006, pp. 69–74.

- [104] J. F. Roberts, “Design of an autonomous hovering miniature air vehicle as a flying research platform,” Master’s thesis, The University of Sydney, New South Wales, Australia, March 2007.
- [105] J. L. Meriam and L. G. Kraige, *Engineering Mechanics Dynamics*, 6th ed. Wiley, 2010, vol. 2.
- [106] A. Isidori, L. Marconi, and A. Serrani, *Robust Autonomous Guidance: An Internal Model Approach*, 1st ed., ser. Advanced in Industrial Control. Springer, 2003.
- [107] V. G. Rao and D. S. Bernstein, “Naive control of the double integrator,” *IEEE Control Systems Magazine*, vol. 21, no. 5, pp. 86 – 97, 2001.
- [108] D. McFarlane and K. Glover, “A loop shaping design procedure using H_∞ synthesis,” *IEEE Transactions on Automatic Control*, vol. 37, no. 6, pp. 759–769, 1992.
- [109] G. Papageorgiou and K. Glover, “Design, development and control of the HIRM wind tunnel model,” in *Proceedings of The 38th IEEE Conference on Decision and Control*, vol. 2, Phoenix, Arizona, USA, December 1999, pp. 1529 – 1537.
- [110] ———, “ H_∞ loop-shaping: Why is it a sensible procedure for designing robust flight controllers?” in *Proceedings of the AIAA Conference on Guidance, Navigation and Control*, August 1999.
- [111] L. Sheng, F. Liang, and L. Jia-lai, “Application of H_∞ control in rudder/flap vector robust control for ship course,” in *Proceedings of The International Conference on Mechatronics and Automation, ICMA*, Harbin, China, August 2007, pp. 774–778.
- [112] Y. Jiao, J. Du, X. Wang, and R. Xie, “ H_∞ state feedback control for UAV maneuver trajectory tracking,” in *Proceedings of The International Conference on Intelligent Control and Information Processing (ICICIP)*, Dalian, China, August 2010, pp. 253 – 257.
- [113] A. Lanzon and G. Papageorgiou, “Distance measures for uncertain linear systems: A general theory,” *IEEE Transactions on Automatic Control*, vol. 54, no. 7, pp. 1532–1547, 2009.

- [114] K. Glover and D. McFarlane, “Robust stabilization of normalized coprime factor plant descriptions with H_∞ -bounded uncertainty,” *IEEE Transactions on Automatic Control*, vol. 34, no. 8, pp. 821–830, 1989.
- [115] A. Lanzon, “Weight selection in robust control: An optimization approach,” Ph.D. dissertation, Wolfson College, Department of Engineering, University of Cambridge, October 2000.
- [116] K. Glover, G. Vinnicombe, and G. Papageorgiou, “Guaranteed multi-loop stability margins and the gap metric,” in *Proceeding of The 39th IEEE Conference on Decision and Control*, Sydney, Australia, December 2000, pp. 4084 – 4085.
- [117] A. Lanzon, “Weight optimisation in H_∞ loop-shaping,” *Automatica*, vol. 41, no. 7, pp. 1201–1208, 2005.
- [118] (2009, December) LiPo batteries. Technical Specifications. [Online]. Available: <http://thunderpowerrc.com/G6SportRace35CSeriesLiPoBatteries.htm>
- [119] A. L. D. Franco, H. Bourlès, E. R. De-Pieri, and H. Guillard, “Robust nonlinear control associating robust feedback linearization and H_∞ control,” *IEEE Transactions on Automatic Control*, vol. 51, no. 7, pp. 1200–1206, 2006.